ABSTRACT

Title of thesis: An Experimental and Analytical Investigation of Hydrogen Fuel Cells for Electric Vertical Take-Off and Landing (eVTOL) Aircraft

Wanyi Ng
Master of Science, 2019

Thesis directed by: Professor Anubhav Datta
Department of Aerospace Engineering

The objective of this thesis is a comprehensive investigation of hydrogen fuel cells for electric vertical take-off and landing (eVTOL) aircraft. The primary drawback of battery powered eVTOL aircraft is their poor range and endurance with practical payloads. This work uses simulation and hardware testing to examine the potential of hydrogen fuel cells to overcome this drawback. The thesis develops steady state and transient models of fuel cells and batteries, and validates the models experimentally. An equivalent circuit network model was able to capture the waveforms and magnitudes of voltage as a function of current. Temperature and humidity corrections were also included. Examination of the results revealed that the transient behavior of batteries and fuel stacks are significant primarily shortly after startup of the fuel stack and at the limiting ranges of high and low power; for a nominal operating power and barring faults, steady state models were adequate. This work then demonstrates fuel cell and battery power sharing in regulated and unregulated parallel configurations. It details the development of a regulated archi-

tecture, which controls power sharing, to achieve a reduction in power plant weight. Finally, the thesis outlines weight models of motors, batteries, and fuel cells needed for eVTOL sizing, and carries out sizing analysis for on-demand urban air taxi missions of three different distances – 50, 75, and 150 mi of cruise and 5 min total hover time. This revealed that for ranges within 75 mi, a light weight (5000-6000 lb gross weight) all-electric tilting proprotor configuration achieves a practical payload (500 lb or more) with current levels of battery specific energy (150 Wh/kg) if high burst C-rate batteries are available (4-10 C for 2.5 min). Either a battery-only or battery-fuel cell (B-FC) hybrid power plant is ideal depending on the range of the mission: For inter-city ranges (beyond approximately 50 mi), the mission is impossible with batteries alone, and fuel cells are a key enabling technology; a VTOL aircraft with a B-FC hybrid powerplant, an aircraft with 6200 lb gross take-off weight, 10 lb/ft^2 disk loading, and 10 C batteries, could be sized to carry a payload of 500 lb for a range of 75 mi. For this inter-city range, the research priority centers of fuel cells, as they appear to far surpass future projections of Li-ion battery energy levels based on performance numbers (at a component level), high weight fraction of hydrogen storage due to the short duration of eVTOL missions, and lack of a compressor due to low-altitude missions, with the added benefit of ease of re-fueling. However, for an intra-city mission (within approximately 50 mi), the B-FC combination provides no advantage over a battery-only powerplant; a VTOL aircraft with a battery-only powerplant with the same weight and disk loading as before, and 4 C batteries, can carry a payload of 800 lb for a range of 50 mi. For this mission range, improving battery energy density is the priority.

AN EXPERIMENTAL AND ANALYTICAL INVESTIGATION OF HYDROGEN FUEL CELLS FOR ELECTRIC VTOL (eVTOL) AIRCRAFT

by

Wanyi Ng

Thesis submitted to the Faculty of the Graduate School of the
University of Maryland, College Park in partial fulfillment
of the requirements for the degree of
Master of Science
2019

Advisory Committee:
Professor Anubhav Datta, Chair/Advisor
Professor Inderjit Chopra
Professor James Baeder

Acknowledgments

Thank you to my advisor, Dr. Anubhav Datta, for his mentorship and guidance. Thank you to my family and friends who have supported me through everything. Even the little things mean more than you know.

This work was carried out at the Alfred Gessow Rotorcraft Center, University of Maryland at College Park under the Army/Navy/NASA Vertical Lift Research Center of Excellence (VLRCOE) (grant number W911W61120012), with technical monitoring from Dr. Mahendra Bhagwat and Dr. William Lewis. Technical points of contact were Dr. Wayne Johnson and Chris Silva of NASA and Dr. Mark Valco from the U.S. Army. Additional funding is provided by Army Research Lab (grant number W911NF1620155), with technical monitoring from Dr. Rajneesh Singh. Thank you to Dr. Josef Kallo for his comments and insights on fuel cells, and to the German Aerospace Center (DLR) for hosting me as a summer research assistant.

Table of Contents

List of Tables

List of Figures

List of Abbreviations

a_A	fuel stack activation loss constant for anode
a_C	fuel stack activation loss constant for cathode
A_c	fuel cell active area, m^2
ASR_Ω	fuel stack area specific resistance, Ohm-cm^2(Ω cm^2)
b_A	fuel stack activation loss constant for anode
b_C	fuel stack activation loss constant for cathode
C	concentration loss constant, V
$C_1, ...C_N$	capacitors representing Warburg impedance, Farad (F)
C_{dl}	dielectric layer or double layer capacitance, F (subscripts a and c refer to anode and cathode, respectively)
DL	disk loading, lb/ft^2
E_r	ideal reversible voltage, V
F	Faraday's constant, 96485 Coulombs/mole
FM	rotor figure of merit
H	rotor hub drag (rotor shaft coordinate frame)
i	current density, A/cm^2
i_{0A}	fuel stack activation loss constant for anode
i_{0C}	fuel stack activation loss constant for cathode
I	current supplied by fuel stack or battery, A
L	rotor lift (wind coordinate frame), N
L/D, aircraft	aircraft lift to drag ratio
L/D_e, rotor	effective rotor lift to drag ratio
M_{tip}	rotor tip Mach number
N_b,	number of rotor blades
n_{cell}	battery or fuel cell number of cells
N_{units}	battery number of units in series
P	power supplied by the fuel stack, W
P_B	power supplied by the battery, W
P_C	power to cruise, W
P_H	power to hover, W
P_{kW}	power, kW
P_{load}	power supplied to load, W
Q_{Nm}	torque, Nm
R	ideal gas constant, 8.314 J/mol.K
$R_1, ...R_N$	resistors representing Warburg impedance, Ω
R_{ct}	charge transfer resistance, Ω (subscripts a and c refer to anode and cathode, respectively)
R_s	series resistance, Ω
SFC	specific fuel consumption, lb/hp.hr

SOC	state of charge
T	rotor thrust (rotor shaft coordinate frame)
t_c	fuel cell thickness, m
V_c	cruise speed, ft/s
V_f	true airspeed or forward flight speed, ft/s
V	voltage supplied by fuel stack or battery, V
υ_c	cell voltage, V
υ_{ss}	steady state fuel cell voltage, V
w_f	hydrogen storage weight fraction
$\dot{W}_F$	hydrogen flow rate, kg/s
W_{GTO}	gross take-off weight, lb
W_{PAY}	payload weight, lb
W_{kg}	weight, kg
X	rotor propulsive force (wind coordinate frame), N
Z_w	Warburg impedance, $Ohm(\Omega)$
α_A	fuel cell activation loss constant for anode
α_C	fuel cell activation loss constant for cathode
α_s	rotor shaft tilt, rad
ζ	battery maximum current rating (C-rate), 1/hr
η_{act}	fuel cell activation loss
η_{ohmic}	fuel cell ohmic loss
η_{conc}	fuel cell concentration loss
η	battery charging efficiency
θ_{75}	rotor twist at 75% span
θ_{ac}	aircraft pitch, rad
θ_{py}	pylon pitch, rad
λ	non-dimensional climb inflow
μ	advance ratio
ρ_c	fuel cell area density, kg/m^2

Chapter 1: Introduction

The objective of this thesis is a comprehensive investigation of hydrogen fuel cells for electric vertical take-off and landing (eVTOL) aircraft. The primary drawback of battery powered eVTOL aircraft is their poor range and endurance with practical payloads. This work uses simulation and hardware testing to examine the potential of hydrogen fuel cells to overcome this drawback.

1.1 Motivation

Recent advances in electrochemical power and permanent magnet motors have caused a significant resurgence of interest in manned electric vertical take-off and landing (eVTOL) aircraft [1, 2]. We define eVTOL as vertical lift aircraft propelled by electric power and capable of carrying people. Since the world's first electric manned helicopter flight in 2011 [3] and the first multirotor helicopter flight in 2012 [4], developers ranging from start-ups to major aerospace corporations have introduced many eVTOL concepts in various stages of development. Electric power promises the potential for cleaner, quieter, safer, and more agile aircraft, which are essential characteristics for a new urban air mobility system. Cleanliness results from the lack of particulate pollution from the aircraft, often in densely populated

areas, as well as the potential to use renewable energy for charging batteries and powering water electrolysis to produce hydrogen for fuel stacks. Quietness results from a combination of reduced engine noise and slowed tipspeeds enabled by electric motors and optimized for primarily forward flight missions. Safety results from redundancy in distributed proprotors and multiple power sources. Agility results from the ability to quickly vary rotor RPM and the increased thrust moment in distributed propulsion. Distributed propulsion, or the inclusion of many proprotors distributed throughout the aircraft, is made possible by electric power; the drivetrain is changed from mechanical connections to electrical wires, which makes adding many drivetrains much more feasible from a weight perspective. In 2017, Uber released a vision for an urban air mobility system with these features in a white paper [5]. The principal drawback of these electric aircraft is the poor range and endurance with practical payload (at least 2 passengers). This drawback stems from the weight of lithium-ion (Li-ion) batteries. With current state of the art, a practical aircraft cannot be flown using battery power. The objective of this paper is to examine the use of hydrogen fuel cells to overcome this drawback.

A major limitation for battery powered eVTOL is the specific energy of Li-ion batteries – a maximum of 250 Wh/kg for cells (Panasonic) and 150-170 Wh/kg for packs (Tesla, Saft). Proton exchange membrane (PEM) fuel cells using hydrogen fuel can offer significantly higher specific energy than batteries in a unit that is still clean and hydrocarbon free, mechanically simple, operates at low temperatures (80-100 °C), and produces no harmful emissions during flight. In contrast to batteries, the specific energy of hydrogen fuel is 39.4 kWh/kg with an efficiency of 0.45 when

used in fuel cells. This is much higher even than the specific energy of gasoline, 13 kWh/kg with an efficiency of 0.3 (Carnot efficiency). However, the low weight efficiency of hydrogen storage somewhat diminishes the advantage. The state-of-the-art hydrogen storage weight fraction is 5.5%, so the specific energy of hydrogen including storage is reduced to $39.4 \times 0.45 \times 0.055 = 1$ kW/kg. This is still four times higher than the battery specific energy. The limitation for fuel cells is lower specific power, around 0.5 kW/kg (see for example, Protonex Ion Tiger, HES A-1000). A combination of the high specific power of batteries with the high specific energy of fuel cells can reduce the overall powerplant weight, allow fast charging and refueling, and introduce redundancy in the power source for added safety.

Fuel cell and battery hybrid systems have been demonstrated in all-electric manned fixed-wing aircraft. The Boeing Fuel Cell Demonstrator achieved manned flight in 2008 with a gross weight of 870 kg for approximately 45 min [6]. The German Aerospace Center's electric motor glider Antares DLR-H2 has been successfully used as a flying test-bed with a gross take-off weight of 825 kg [7–9]. This aircraft has been used to investigate different hybridization architectures to allow charging and minimize the powerplant weight, as well as investigating methods to increase reliability. The ENFICA-FC project at Politecnico di Torino developed a two-seater hybrid aircraft that achieved an endurance of 40 minutes [10]. These aircraft serve as a proof of concept for fuel cell powered flight, provide flight data, and identify key obstacles compared to conventional aircraft.

However, all of the above are fixed-wing, not rotary-wing, aircraft. eVTOL requires a rotary-wing aircraft, which have unique challenges associated with high

hover power, low lift to drag ratios (due to the edgewise rotor and hub drag), and highly transient power profiles, including high power during both take-off and landing. Recently, unmanned rotary-wing drones have been flown using fuel cells, but these are small scale aircraft and scarce data is available in the public domain. These aircraft include the United Technologies Research Center's 1.75 kW, 10kg, single main rotor helicopter in 2009 [11] and EnergyOr's 1.5 kW, 9.5 kg quadcopter in 2015 [12].

This paper deals with larger scale manned aircraft, with the objective of comparing two main electrochemical power sources – Li-ion batteries and hydrogen fuel cells, separately and in combination in a power-sharing mode – for an on-demand air taxi mission. The possible benefits of battery-fuel cell (B-FC) hybridization for manned electric rotorcraft were reported for a R-22 beta II helicopter [13, 14] in a conceptual conversion study. In this study, the feasibility of power-sharing and architecture required to enable it was left as future work. Moreover, it was a conversion study carried out on an existing aircraft, with the recommendation that an integrated aircraft and powerplant system be sized together in the future. Both these tasks are carried out as part of this thesis. This thesis provides actual demonstration of power-sharing through hardware testing, develops steady-state and transient powerplant models, calibrates them with test data, and carries out integrated eVTOL sizing based on measured experimental overheads and performance analysis validated with XV-15 flight test data.

1.2 Objective

The first step is to develop new propulsion system models for the design of this new class of aircraft. There have been several efforts in recent years to build such models [13, 17–20] and apply them to conceptual design of rotorcraft [14, 21]. However, these models are all limited to steady-state operation. Models that can predict both steady-state and transients would allow for refined sizing as well as an analysis of load transients and unsteady maneuvers of an aircraft. In this paper, batteries and fuel cells are modeled as equivalent circuit networks (ECN) using resistor-capacitor (RC) models to more refined Warburg impedance based models [22–25]. The transient models predict voltage variation due to rapid changes in current. For batteries, they also capture the variation due to state of charge. The models are calibrated (for time constants) and validated (for phenomenological trends) using an experimental set up. The set up consisted of a commercial fan-cooled proton exchange membrane (PEM) fuel stack, pressurized hydrogen equipment, and a lithium polymer (LiPo) battery connected in parallel to either an electronic load or a flying quad-rotor. A fuel cell requires many pieces of accessory equipment, called balance of plant, that incur power losses and add weight overhead. The setup was also used to determine these balance-of-plant losses and overheads. A more detailed description of the hardware is provided in the Experimental Setup chapter.

The second step is to establish regulated power sharing between a fuel stack and battery. This involves controlling the ratio in power contribution from the two sources at any point during the mission, as well as charging the battery during flight.

The schematic used by the Anteres DLR-H2 [9] was adopted as a starting point. Improvements were made to customize the power sharing algorithm, increase the level of control over the power sharing ratio, and automate the process. These are described in more detail in the section on Demonstration of Power Sharing.

The third step, sizing of eVTOL, begins with state-of-the-art data for motor and battery weights as a basis for weight models. However, fuel cell weights cannot be readily inferred from data due to the wide variation in type of application and type of hydrogen storage. Top-level technology assessments can be found in the U.S. Department of Energy's continuing Hydrogen and Fuel Cell Program, automotive literature, and limited UAV applications reported in trade journals. These are not adequate for a proper weight estimation. Instead, a geometry- and material-based weight break-down is used, guided by (in-house) measurements from a commercial fan cooled low power stack, and reported literature on the custom built, liquid cooled, high power automobile stacks of Honda [26] and Toyota [27, 28].

Sizing of the aircraft calculates the minimum gross (total) take-off weight and payload weights that are achievable for a prescribed mission. The structural weights are based on simple expressions, correction factors, and available data on existing aircraft, so that the primary focus remains on the impact of the new powerplant. The results are compared for different powerplant configurations: turboshaft, battery alone, fuel cell alone, and battery and fuel cell (B-FC) hybrid. They are also compared for edgewise and tilting prop rotor configurations.

Specific targets are based on Uber's white paper [5] for a demonstration of sizing. The maximum installed power was taken to be 500 kW (hover) with cruise

at the best range velocity. Details of the mission are provided in the Aircraft Sizing chapter.

The effects of technology advances are investigated at the end. The baseline results use parameters that are currently feasible at the component level. These parameters include battery specific energy, fuel stack specific power, and hydrogen tank weight fractions. Only the battery maximum current, or C-rate, is allowed to vary unconstrained beyond what is reported at this capacity level. Results are also calculated based on improved technology forecast for each individual component; for example, a battery specific energy of 250 Wh/kg envisioned by the automobile industry, fuel stack specific power of 2 kW/kg reported by Toyota, and a hydrogen weight fraction of 7.5% – a target met by the Department of Defense hydrogen fuel cell program for pressured storage and well within the 10% reported by the UTC fuel cell helicopter. These technology assessments provide insights for prioritizing future investments.

1.3 Fundamentals of Fuel Cells and Batteries

Fuel Cells

The Proton Exchange Membrane or Polymer Electrolyte Membrane (PEM) fuel cell is the state-of-the-art fuel cell for maximum specific power. Figure 1.1 shows a functional description of the physical components of a PEM hydrogen fuel cell. The anode and cathode are electrodes which undergo oxidation and reduction reactions, respectively. The chemical reactions are given by Eq. 1.1 on the anode

side and Eq. 1.2 on the cathode side. The gas diffusion layer is composed of carbon paper or cloth, carbon powder, and polytetrafluoroethylene (PTFE). The catalyst is composed of platinum/carbon powder and Nafion ionomer. The proton exchange membrane is a polymer, typically Nafion, which conducts protons. Electrons, which cannot pass through the membrane, provide useful current to a load. On the systems level, fuel cells are connected in series and packaged into fuel stacks.

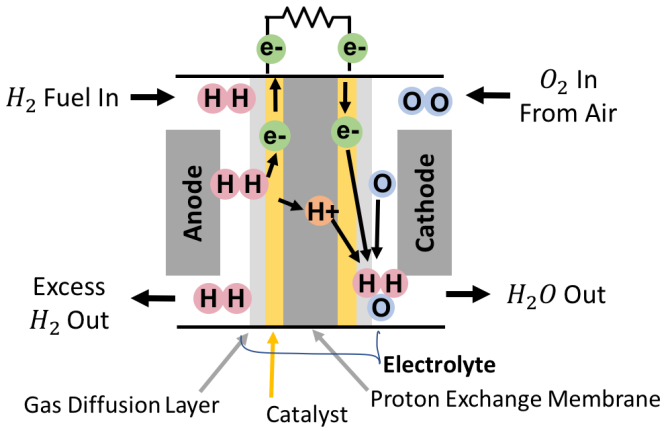

Figure 1.1: Schematic of fuel cell.

$$\text{Anode, oxidation :} \qquad H_2 \rightarrow 2H^+ + 2e^- \tag{1.1}$$

$$\text{Cathode, reduction :} \qquad \frac{1}{2}O_2 + 2H^+ + 2e^- \rightarrow H_2O \tag{1.2}$$

There are five major types of fuel cells, which all follow the same electrochem-

ical principle as the PEM fuel cell, but are differentiated by their electrolytes and vary in operating temperature, materials, fuel tolerance, and performance characteristics. They are: phosphoric acid fuel cell (PAFC), polymer electrolyte membrane fuel cell (PEMFC), alkaline fuel cell (AFC), molten carbonate fuel cell (MCFC), and solid oxide fuel cells (SOFC). Of these, PEM fuel cells are the most suited for aviation due to their high power density, high specific power, low temperature operation (around 80°C), and fast startup time [29, 30].

Batteries

Lithium-ion (Li-ion) batteries are the state of the art for aviation. Figure 1.2 shows the components of a notional Li-ion battery with C_6Li_x as the anode material and $LiCoO_2$ as the cathode material. The discharge chemical reactions are given by Eq. 1.3 on the anode side and Eq. 1.4 on the cathode side, and charging follows the same reactions in reverse. As in the fuel cell, protons are conducted through the electrolyte, and electrons provide useful current to the load. $LiCo_2$ was the first successful cathode material. Today, there are many different cathode materials, but almost all require Cobalt, a rare material, in some percentage. The anode is typically graphite.

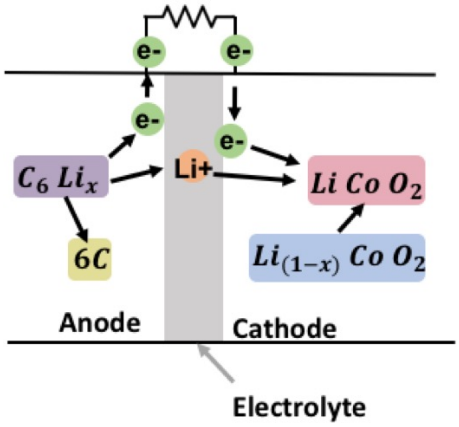

Figure 1.2: Schematic of discharging Li-ion battery.

$$\text{Anode, oxidation :} \qquad C_6Li_x \rightarrow xLi^+ + xe^- + 6C \tag{1.3}$$

$$\text{Cathode, reduction :} \qquad xLi^+ + xe^- + Li_{1-x}CoO_2 \rightarrow LiCoO_2 \tag{1.4}$$

The experimental portion of this work used lithium-polymer (LiPo) batteries. LiPo batteries use a gel electrolyte instead of the liquid electrolyte used in Li-ion batteries. However, the electrochemistry is identical, so the performance is also the same.

1.4 History of Fuel Cells in Transportation

The discovery of the principle of fuel cells is attributed to either Christian Friedrich Schönbein or Sir William Robert Grove in 1838. Fuel cells were brought from a laboratory concept to a practical power source in the 1930's by Francis Thomas Bacon, who developed the first hydrogen-oxygen, alkaline fuel cells. During WWII, his fuel cells were used in the submarines of the Royal Navy [31].

Early Space Industry

Fuel cells were brought to a mature, reliable power source for space applications by the Gemini and Apollo programs in the 1960's. They were more promising than other power sources for meeting the new requirements of extended manned missions. The Gemini program (1962–1965) used solid polymer electrolyte (SPE), also called ion-electrolyte membrane (IEM), fuel cells with hydrogen and oxygen reactants. The electrolyte was a sulfonated polystyrene resin, the electrodes were titainum screens, and the catalysts were platinum with PTFE deposited on the screens. This technology was then used on the Biosatellite spacecraft in 1967, during which the Nafion membrane was introduced, and is still used today. The Gemini powerplant was 1 kW, made up of 126 cells total.

The Apollo program (1968–1972) fuel cells were modified from Bacon's original alkaline fuel cell rather than the Gemini cell. The modifications included operating at a reduced pressure of 50 psi and increased temperature of 260°C. The electrolyte was an aqueous alkaline solution of KOH-H_2O. The anode was porous nickel, the

cathode was lithiated, oxidized porous nickel, and no platinum catalyst was needed due to the higher temperatures. This powerplant was nominally 1.5 kW with a peak power capability of 2295 W and weighed 220 lb. It was rated to 400 hr and ran for 690 hr without failure.

The Shuttle Orbiter built on Apollo alkaline cells. The previous free electrolyte was replaced by an alkaline solution in an asbestos matrix. The temperature was reduced to 93°C, which meant a catalyst layer was required. The electrodes were gold plated Ni with a catalyst layer and PTFE. Its three fuel cell powerlpants combined supplied 7 kW average and 12 kW peak power and weighed 750 lb [32]. Specific energy for these alkaline fuel cells increased drastically from 0.0247 kW/kg in 1962 (Apollo) to 0.275 kW/kg in 1973 (Shuttle Orbiter) [33].

The two major fuel cell technologies at this point were SPE and alkaline fuel cells. SPE cells had better performance but lacked long term catalyst stability, which caused a decrease in performance over time. Alkaline cells had lower performance (in terms of voltage efficiency) but a longer lifespan. In the 1980's, the performance of the Gemini era SPE fuel cells was greatly improved by making the membrane thinner to reduce the internal ohmic resistance of the cell. These became known as proton exchange membrane (PEM) fuel cells. This improvement made the performance of PEM fuel cells competitive with that of alkaline fuel cells without the lifespan limitation of alkaline fuel cells [32].

Automobile Industry

Toyota Motor Corporation began developing fuel cell hybrid vehicles in 1992.

They marketed their first vehicle in 2002 and were the first in Japan to acquire vehicle type certification in 2005. The Toyota FCHV 2005 model weighed 1880 kg with a maximum driving range of 330 km and maximum speed of 155 km/h. The proton exchange membrane (PEM) fuel cell generated 90 kW and used hydrogen stored at a maximum of 35 MPa (1 MPa = 10 bar = 145 psi). The fuel cell was connected in parallel to a nickel-metal hydride battery by a converter, and supplied power to a permanent magnet motor through an inverter [34].

Honda also first introduced their fuel cell vehicle in 2002. In the following years, they made improvements to the vehicle's driving and environmental performance. In 2009, the Honda FCX Clarity was capable of a maximum power of 100 kW, speed of 160 km/h, and range of 280 miles. It used a PEM fuel cell with Li-ion battery for power assist, and hydrogen volume of 171 L stored at 35 MPa. It uses a combination of regenerative and hydraulic breaking to recover energy. [26]. Today, the U.S. DoE has an ongoing Hydrogen and Fuel Cells Program focused on research and development for automobile needs. Recently, in Jan 2019, it announced the intent to pursue affordable and reliable large-scale hydrogen generation, transport, storage, and utilization in the U.S.

Fixed Wing Aircraft

The first fuel cell powered flight is credited to the Global Observer in 2005, developed by AeroVironment. It used PEM fuel cells with liquid hydrogen fuel. The test flights lasted over an hour, and the company reported that a full tank would allow for a 24 hour flight. This aircraft was unmanned [35].

A larger unmanned fixed-wing aircraft was published in 2007 by Georgia Tech with more data made available in the public domain. The total mass of the aircraft was 16.4 kg. It utilized a polymer electrolyte membrane (PEM), self-humidified, hydrogen-air fuel cell with a peak output power of 465 W and weight of 4.96 kg. Liquid cooling was used to maintain the fuel stack's operational temperature. The hydrogen was stored at 31 MPa with a maximum capacity of 192 Standard L. This equated to a specific energy of 7.1 Wh/kg and specific power of 52 W/kg. Based on the hydrogen tank capacity, the aircraft was capable of a 43 min cruise [36]. Several other fixed-wing fuel cell UAVs have been developed since [37], and are not mentioned here.

The first manned, fixed-wing, fuel cell aircraft was successfully flight tested in 2008 by The Boeing Company. It utilizes a hybrid powerplant with a PEM fuel cell as the main power source, and a Li-ion battery for supplemental power during takeoff and climb. The aircraft was the Austrian HK36 Superdimona motor glider. The maximum takeoff weight was 860 kg with a payload of 71 kg. The maximum power output of the fuel cell was 24 kW and of the battery was 50-75 kW. In case of fuel cell failure, this battery was sized to supply maximum power for 5 min. The fuel capacity was 1 kg of hydrogen stored at 350 bar. The aircraft used a permanent magnet DC brushless motor with an inverter [6]. The 2008 Boeing test was the first piloted fuel cell airplane to have systematic documentation of its development and flight testing.

In 2009, the German Aerospace Center (DLR) successfully integrated an air cooled, hydrogen PEM fuel cell into their manned fixed-wing aircraft, Antares DLR-

H2. The aircraft was built on a motor glider Antares 20E with a 42kW motor and inverter. The maximum gross weight was 825 kg and payload weight was 100 kg. The maximum velocity was 175 km/h. The nominal power available was 15.6 kW, and the aircraft was capable of taking off on fuel cell power alone. At high altitudes of 2500 m, the fuel cells provided 14 kW, which was enough to maintain level flight. The company then investigated a lower temperature, liquid-cooled PEM hydrogen fuel cell, as well as a methanol fueled cell with a reformer for processing hydrogen from the methanol [38]. In 2015, DLR published a new concept that extended the DLR-H2 to include a battery hybrid to increase the range and improve reliability. For this design, the fuel stack was capable of providing 30 kW, and an additional 40 kW could be added by the battery [9]. A similar system is now being developed for DLR's four-seat HY4 aircraft (unpublished).

Another manned, fixed-wing, fuel cell aircraft was test flown at Politecnico di Torino through the ENFICA-FC project, published in 2012. This was also a hybrid system with a fuel cell and supplemental battery. Two fuel stacks provided up to 20 kW (50% maximum required power) for the entirety of the mission, while two batteries could deliver an additional 20 kW for 18 min, including contingency. It was converted from a RAPID200 sport aircraft. The maximum takeoff weight was 554 kg and payload weight was 75 kg. A total of 1.2 kg of hydrogen fuel was stored at 350 bar, with a total hydrogen system weight of 52 kg. An endurance of 40 minutes was achieved, which was stated to be limited by water consumption (for cooling) rather than hydrogen. The power sources were connected to an air-cooled brushless electric motor via a DC/DC boost converter and AC/DC inverter. [10]

Rotary Wing Aircraft

Fuel cells were not introduced to rotary wing aircraft until very recently, due to a larger range of required power over the course of a typical rotary wing mission. There are only a few published records, and all are small-scale unmanned aircraft. The first documented fuel cell powered, unmanned, rotary wing aircraft was a remote controlled helicopter flown in 2008 by United Technologies Research Center (UTRC). It had a gross take-off weight of 10 kg, rotor diameter of 1.83 m, and was powered entirely by a 1.75 kW PEM fuel cell. It used an off-the-shelf hydrogen storage tank with a storage fraction of only 2.3%. The test flight lasted for 20 min, but UTRC predicted that with a custom tank (10% storage fraction), the maximum endurance would be 1 hr 45 min. They concluded that for payloads less than 1.5 kg, the fuel cells offered greater endurance than an advanced battery [11].

Following the first single main rotor helicopter, EnergyOr flew the first multirotor VTOL aircraft. A commercial quadrotor airframe was used, with a gross weight of 9.5 kg and payload up to 1 kg. The flight lasted for 2 hr 13 min. The company reported that the high specific energy of their fuel cells allow flight times two to three times longer than with state-of-the-art batteries [12].

Since then, several companies including Horizon Unmanned Systems and MMC have marketed unmanned, fuel cell powered, VTOL drones, but with limited to no scientific data available. To date there have been no demonstrations of piloted-scale VTOL aircraft utilizing fuel cell power.

1.5 Organization and Scope of Paper

This paper is organized into six technical chapters. Following this introduction, Chapter 2 describes the experimental setup used to calibrate and validate the fuel stack and battery models. Chapter 3 covers model development. Chapter 4 is on experimental validation of the models. Chapter 5 documents the development of a regulated power sharing architecture to control the fuel stack and battery working in a hybrid configuration. Chapter 6 discusses weight models for the power plant to be used for aircraft sizing. Finally, Chapter 7 describes the sizing procedure and principal results of an eVTOL for an on-demand urban air-taxi mission.

The first part of the paper, Chapters 2 through 5, deals with hardware and modeling. The second part, Chapters 6 through 7, deals with weights and aircraft sizing. The motivation of the first part is provided by the principal result of the second part – that a hybrid solution can be superior to individual battery-only or fuel cell-only solutions; the principal result of the second part is in turn based on the weights and efficiencies measured in the first part. Thermal effects are not modeled in the first part, but built-in thermal management is implicit in weights and efficiency numbers. Cost and noise are ignored in the second part.

Chapter 2: Experimental Setup

A commercial 300 W PEM fuel stack and a 2800 mAh 3 cell lithium polymer (LiPo) battery were used to construct a simple test-bed to understand the system overheads and acquire test data for calibrating and validating the fuel cell and battery models. Overheads include balance of plant losses and accessory weights, which are later utilized for aircraft sizing. Due to the surrogate nature of the setup (non-flight worthy) these overheads are expected to be conservative. Figure 2.1 provides a basic flow diagram of how power is delivered in a parallel hybrid system from the battery and fuel stack to a load. This applies to the setup used in power sharing demonstrations described in Section 5. The unregulated version of power sharing architecture is a direct connection of the two power sources in parallel with diodes to ensure the current always flows away from each power source. The regulated version adds controlled charging and discharging of the battery in a strategic manner to minimize the powerplant weight. The data loggers record current and voltage over time.

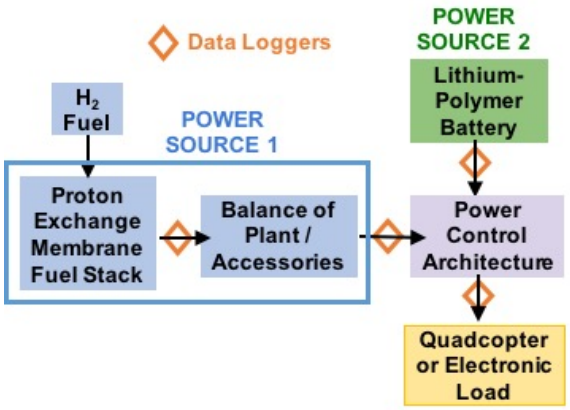

Figure 2.1: Flow diagram of a parallel hybrid power system.

A photograph of the hardware is shown in Fig. 2.2. The fuel stack controller controls the supply and purge valves to allow hydrogen flow in and out the fuel stack. This controller requires external power which can be provided by a power supply or an additional battery. The fuel stack operates around 50 V, so a DC-DC converter is used to reduce this voltage to that of the battery, to around 12 V. The power output from the fuel stack is connected in parallel with a battery. The combined power is then connected to a bench-top programmable electronic load during controlled tests. It is also connected to a quadcopter for tethered flight tests.

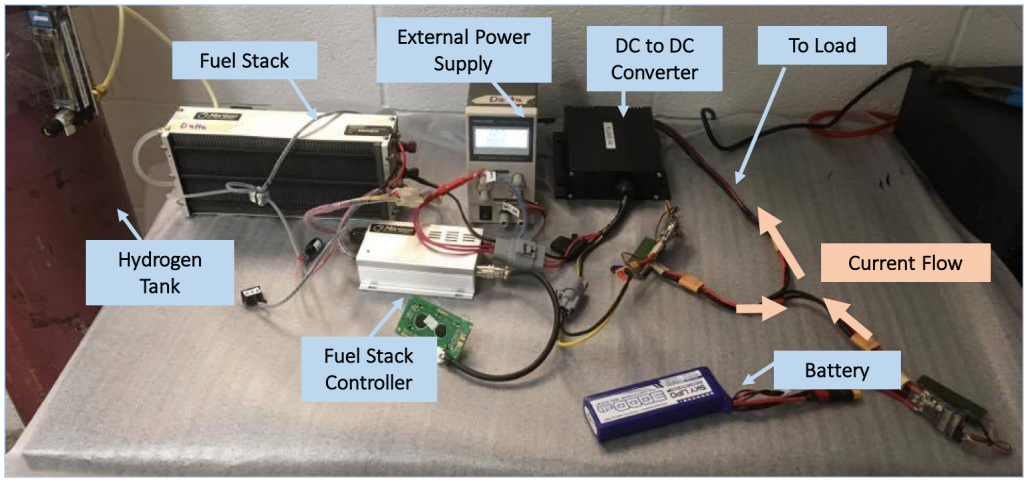

Figure 2.2: Battery and fuel cell hybrid test bed hardware.

Table 2.1 gives details of each component used in the experimental setup.

Table 2.1: Details of components in experimental setup

Component	Manufacturer	Part Number	Description
Hydrogen	Airgas	HYZ200	99.998% purity (Grade O), size 200 cylinder
Pressure Regulator	Roberts Oxygen	3151321-27-M1H	Custom 315 Series Dual Stage Regulator, H2 gas; inlet: 2200 psi, CGA 350; outlet: 7.5 psi, 1/4" compression tube fitting
Tubing	McMaster-Carr	5156K87	Flame-Retardant Polyethylene Tubing, 0.17" ID, 1/4" OD, 0.04" Wall Thickness
Tubing Fittings	McMaster-Carr	50915K123; 50915K193; 5526K72	Nut and sleeve for 1/4" OD brass compression tube fitting; Push-to-fit connectors, 1/4" NPT to 1/4" tube
Flow Meter	Vögtlin	GSM-B9SA-BN00	Red-y smart H2 meter, 0.26-13 L/min, 0.5 bar
Fuel Stack	Horizon	FCS-C300	H-300 PEM fuel cell, 300 W
DC-DC Step Down	Astron	4812-40	30-56 Vdc input, 13.8 Vdc output, max 32 A output
Battery	Zippy	Z28003S-30	2800 mAh, 3 series 1 parallel, 30C discharge, 2C charge
Electrical Wire	McMaster	7715T16	8 gauge stranded bare copper building wire
Electrical Connectors	various		XT-60 connectors
Data Loggers	Eagle Tree	MPRV4	eLogger V4, measures 5-80V and 100A peak at frequencies up to 50 Hz

A detailed plumbing and wiring diagram of the test bed with the quadrotor connected is shown in Fig. 2.3. The thicker black lines represent tubing for hydrogen flow with the arrows pointing in the direction of flow. The thinner lines represent electrical wires with the arrows pointing in the direction of positive current or control signals.

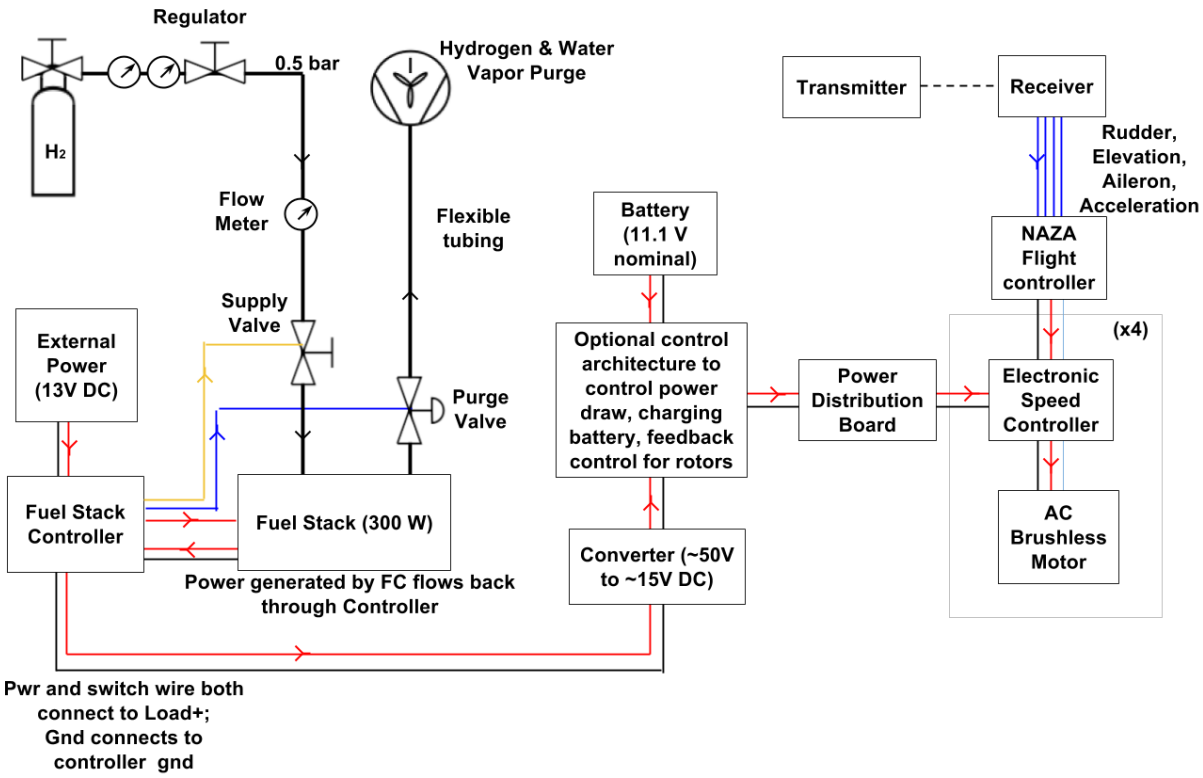

Figure 2.3: Plumbing and wiring diagram of experimental setup for tethered quadcopter flights.

The setup and start up of the fuel cell and battery system is described as follows. The hydrogen gas cylinder valve was opened momentarily to expel any debris in the outlet tube, and then closed securely. The pressure regulator was screwed on to the cylinder outlet. A 1/4" brass compression fitting was used to

connect flexible tubing to the pressure regulator outlet to deliver hydrogen gas to the fuel stack. Push-to-connect fittings were used to connect the flow meter to the hydrogen line. Power must be supplied to the flow meter (in this setup via a conventional wall outlet) before the fuel stack is turned on. The fuel stack was assembled as described in the Horizon user's manual. The electrical output of the fuel stack was connected to the DC/DC converter to reduce the fuel stack voltage. The DC/DC converter contains a fuse in series, which could be blown if the current exceeded 15 Amps. A diode was placed in series with the output of the DC/DC converter to prevent current flowing backwards into the fuel cell. Electrical wiring was soldered to form two branches to connect the power output of the DC/DC converter in parallel with the LiPo battery. In the absence of the diode, the fuel cell must be turned on before connecting the battery, or the fuse will be blown and require replacement. A long piece of cable was attached to this parallel connection to deliver power to the load. The load was either the programmable electronic load (shown in Fig. 2.4) or quadcopter (shown in Fig. 2.5). Data loggers were installed in series at the fuel stack output, battery output, and load.

The fuel stack was prepared for start up as described in the Horizon user's manual. The pressure regulator was turned all the way down (counter clockwise). The hydrogen bottle was opened completely (counter clockwise). Then, the pressure regulator was slowly increased (clockwise) until the operating pressure of the fuel stack (as described in the user's manual) was reached. A hydrogen probe or soapy water was used to test for leaks at all the fittings. Additionally, the bottle was closed to verify that the system does not lose pressure over the course of a few minutes.

The bottle was then reopened before turning on the fuel stack for testing. The battery was connected after the fuel stack was turned on.

For system shutdown, the following steps are taken in this order. The load was disconnected, the battery was disconnected, the fuel stack was turned off, the hydrogen bottle was closed completely (clockwise), the pressure regulator was turned to the minimum set pressure (counter clockwise), and fuel stack connections were disconnected according to the user's manual.

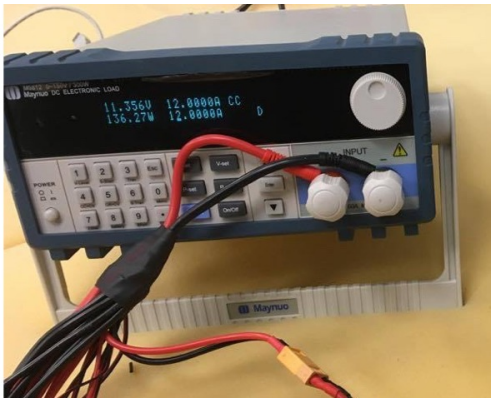

Figure 2.4: Electronic programmable load; M9812 by Maynuo; max 150 V, 30 A, 300 W.

Figure 2.5: In-house built quadcopter.

The fuel stack operation includes intermittent short circuits every 10 seconds that last for 100 ms each time. This behavior is inherent to the Horizon fuel stack design. It manifests as segments of time when the fuel stack stops delivering power to the load. In the parallel fuel stack and battery configuration described above, the battery power contribution jumps up to 100% of the required power. In this thesis, these drops are filtered out, because they are considered artifacts of a test-grade fuel stack and would not be present in a flight-grade fuel stack.

2.1 Mass Overhead

The component weights are presented in Table 2.2. From these weights, the overhead mass associated with the DC-DC converter (including cables) was calculated to be 15% of the total mass. This represents the portion of the mass that would not be included in the specific energy of a fuel cell, and is later used in the Sizing section as a factor to obtain a more accurate system mass. The mass overhead for the hydrogen regulator is 13%, but this can likely be reduced for a digital pressure gauge and aerospace grade regulator. Data collection devices accounted for 4% mass overhead. Only the DC-DC step down mass overhead is used in the sizing calculations later. This low-end commercial fuel stack has a specific power of 0.1 kW/kg based on the fuel stack plus controller weight.

Note that in this experimental setup, for data collection purposes, one battery is connected in parallel to the fuel stack as a power source and a variable voltage power supply is used to power the fuel stack controller. However, in a more realistic setup, the same battery would be used to power both the vehicle and fuel stack controller. So the variable voltage power supply is left out of Table 2.2.

Table 2.2: Mass breakdown of experimental setup

	Component	Mass (g)	% of Total Mass
Fuel Stack	Fuel Stack (300 W)		
	Supply Valve		
	Purge Valve		
	Cooling Fan		
	Total	2901	44.6
	Controller	433	6.7
	Display	66	1
Balance of Plant/	Battery for Controller	216	3.3
Accessories	DC-DC Converter	943	14.5
	Data Loggers (4)	158	2.4
	Displays (4)	54	0.8
	Cable Stub, DC Converter In	30	0.5
	Cable Stub, DC Converter Out	28	0.4
Hydrogen System	Hydrogen Regulator	840	12.9
	Hydrogen (35 L at 515 psig)	602	9.3
	Tube, Hydrogen Inlet	14	0.2
	Tube, Purge	3	0.05
Total		6503	

2.2 Balance of Plant Power

This setup was used to find the balance of plant (BOP) losses of the fuel stack. The primary losses occurred at the DC-DC converter and the tether that delivered power to the load. The former is relevant to sizing later, while the latter is not. The fuel stack was connected to the DC-DC converter, which was then connected to the tether, which was in turn connected to a programmable electronic load. The load was used to draw a constant current from the fuel stack, and data were collected at three locations: before the DC-DC step down, after the DC-DC step down, and at

the load.

The percent loss was calculated at different power levels (i.e. different currents) and shown in Fig. 2.6. In the middle plot of Fig. 2.6, the power loss over the DC-DC converter decreases as steady-state fuel stack power load increases. This may be because at higher power load, the fuel stack operates at a lower voltage (seen later in Fig. 3.1), bringing the operating voltage (˜45-55 V) closer to the target output voltage of the DC-DC converter (˜12 V); at higher power, the converter is generating a smaller voltage difference, which leads to a smaller power loss. The mean is loss is ˜24.5%. In the right-hand plot of Fig. 2.6, the power loss over the tether cable increases as steady-state fuel stack power increases. This can be explained by the relation $P_{loss} = I^2R$ where R is the constant resistance of the cable; when the steady-state power load increases, the current drawn increases, so the power loss also increases.

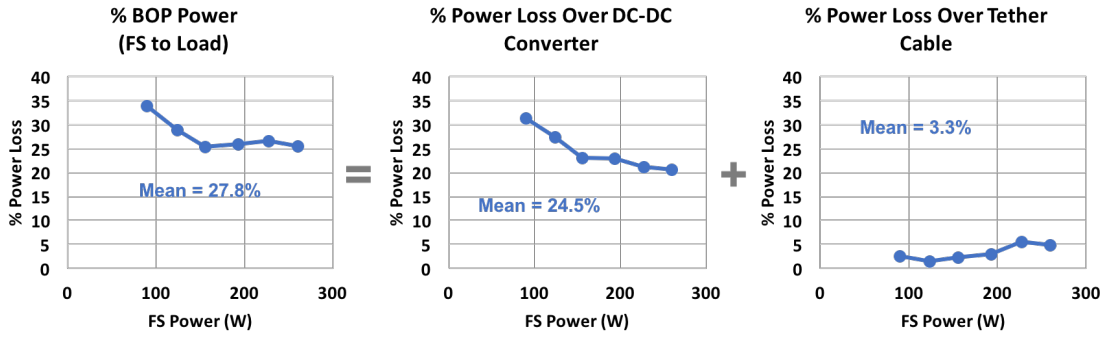

Figure 2.6: Breakdown of balance of plant power losses for fuel stack at steady-state using a programmable load.

The losses in steady-state were compared to those occurring under transient conditions using a quadcopter. Data were collected during a hover test at each of the four points labeled data logger in Fig. 2.1. Then, assuming the mean steady

state losses in Fig. 2.6 still apply, the power after the step down and at the load were predicted and compared to the experimental results. Figure 2.7 shows the fuel stack power before and after the DC-DC step down. The mean steady-state loss was 24.5%, so the expected power after the DC-DC was calculated as $P_{FS} \times (1 - 24.5)\%$, where P_{FS} is the power produced by the fuel stack. However, Fig. 2.6 shows that the power loss across the DC-DC step down was smaller during the actual flight (around 13%) than during the steady state characterization. A value of 20% was used as the balance of plant power loss in the sizing calculations presented later, which is still conservative compared to a custom designed step down that would be used in flight. Additionally, if the powerplant is designed such that the battery and fuel stack operate at a similar voltage, this DC-DC step down can be eliminated from the system entirely.

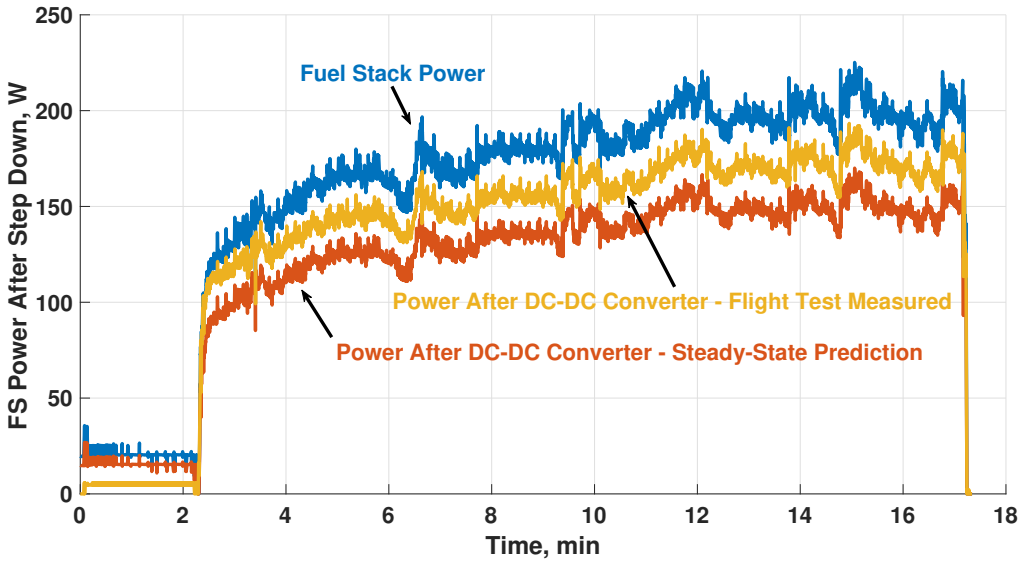

Figure 2.7: Fuel stack power before and after DC-DC step down during quad-rotor flight test shows 13% loss; shown for comparison, measured loss of 23% in bench top steady-state condition.

The loss along the tether was noticed to be slightly higher during the flight test than during steady state characterization. However, the tether is specific to the flight test and is therefore not required for aircraft sizing.

Chapter 3: Model Development

3.1 Fuel Stack Steady-State Model

Power plant sizing calculations require steady state voltage versus current (i-υ or polarization) curves. A steady-state model was developed based on a well-accepted description of the underlying electrochemical behavior of a fuel stack [29], extended to include empirical corrections for fuel stack temperature and humidity based on data from Ref. [39] and [40]. Then, transient operating characteristics were modeled using an equivalent circuit network (ECN). The ECN model captures the principal characteristics of transient dynamics [41–44] through a capacitative (first order) linear behavior. The circuit elements that determine the underlying time constants are calibrated using in-house experiments using the setup described earlier.

The steady state behavior of the fuel stack is modeled using Eq. 3.1. The voltage $\upsilon(i)$ is a function the current density i and is equal to the ideal or open circuit voltage E_r minus activation, ohmic, and concentration losses. These consist of eight empirically derived thermodynamic constants: $\alpha_A, \alpha_C, i_{0A}, i_{0C}$ (unitless constants), C (constant in volts), ASR_Ω (area specific resistance in Ohm-cm^2), i_L (limiting current in A/cm^2), and i_{leak} (leakage current in A/cm^2). The constant E_r can be

predicted empirically, or taken from test data.

$$\upsilon(i) = E_r - \eta_{act} - \eta_{ohmic} - \eta_{conc} \tag{3.1}$$

where

$$E_r = 1.229 - (T - 298.15) \times 8.46 \times 10^{-4} + 4.309 \times 10^{-5}(\ln p_{H_2} + 1/2 \ln p_{O_2})$$

for operation in air, at a pressure of 1 atm and temperature T (Kelvin).

$$\eta_{act} = (a_A + b_A \ln(i + i_{leak})) + (a_C + b_C \ln(i + i_{leak}))$$

$$\eta_{ohmic} = i \; ASR_{\Omega}$$

$$\eta_{conc} = C \ln \frac{i_L}{i_L - (i + i_{leak})}$$

and

$$a_A = -\frac{RT}{\alpha_A n_A F} \ln i_{0A} \qquad b_A = \frac{RT}{\alpha_A n_A F}$$

$$a_C = -\frac{RT}{\alpha_C n_C F} \ln i_{0C} \qquad b_C = \frac{RT}{\alpha_C n_C F}$$

Here, T is the temperature in Kelvin, R = 8.314 J/mol K is the ideal gas constant, F = 96485 C/mol is Faraday's constant, $n_A = 2$ moles of electrons per mole of hydrogen at the anode (see Eq. 1.1), $n_C = 4$ moles of electrons per mole of oxygen at the cathode, $p_{H_2} = 1$ is the partial pressure of hydrogen, and $p_{O_2} = 0.21$ is the partial pressure of oxygen in the air at 1 atm. E_r for the fuel stack operating

at 60°C is 1.19 V.

To calibrate the constants, the programmable electronic load was directly connected to the fuel stack (no DC-DC step down) and the current and voltage supplied by the fuel stack were recorded. The data was collected simultaneously using an Eagle Tree data logger, an AttoPilot breakout board, and the built-in fuel stack display. The current was increased in steps from zero until the fuel stack reached its automatic shutoff voltage; the voltage was allowed to reach a steady state at each current. It should be noted that the last data points at the high current end were not steady-state values; they were recorded during a transient period just before the fuel stack shut off automatically due to low voltage.

Figure 3.1 summarizes the state of the art in fuel cell performance. The data measured from this setup are represented as FC-1 Data-1. The voltage is normalized by the number of cells in the stack and current is normalized by the total active area of the stack. FC-1 Data-2 is data from the same stack but from the manufacturer's specifications. They are close, as expected. Two other data sets are shown for comparison. FC-2 is from a state-of-the-art (2015), aerospace grade, complete stack similar to that used by DLR. FC-3 is from a state-of-the-art (2006) single cell tested by Yan [39] at 1 atm and 60°C. The power density in the lower plot is simply the product of cell voltage and current density shown in the upper plot. The calibrated constants are given in Table 3.1; the fitted models are shown as lines in Fig. 3.1. The main difference is the high current and power from higher quality cells. Later in the sizing section, the polarization curve of FC-3 will be used, which is well within what is achievable for an aerospace fuel stack.

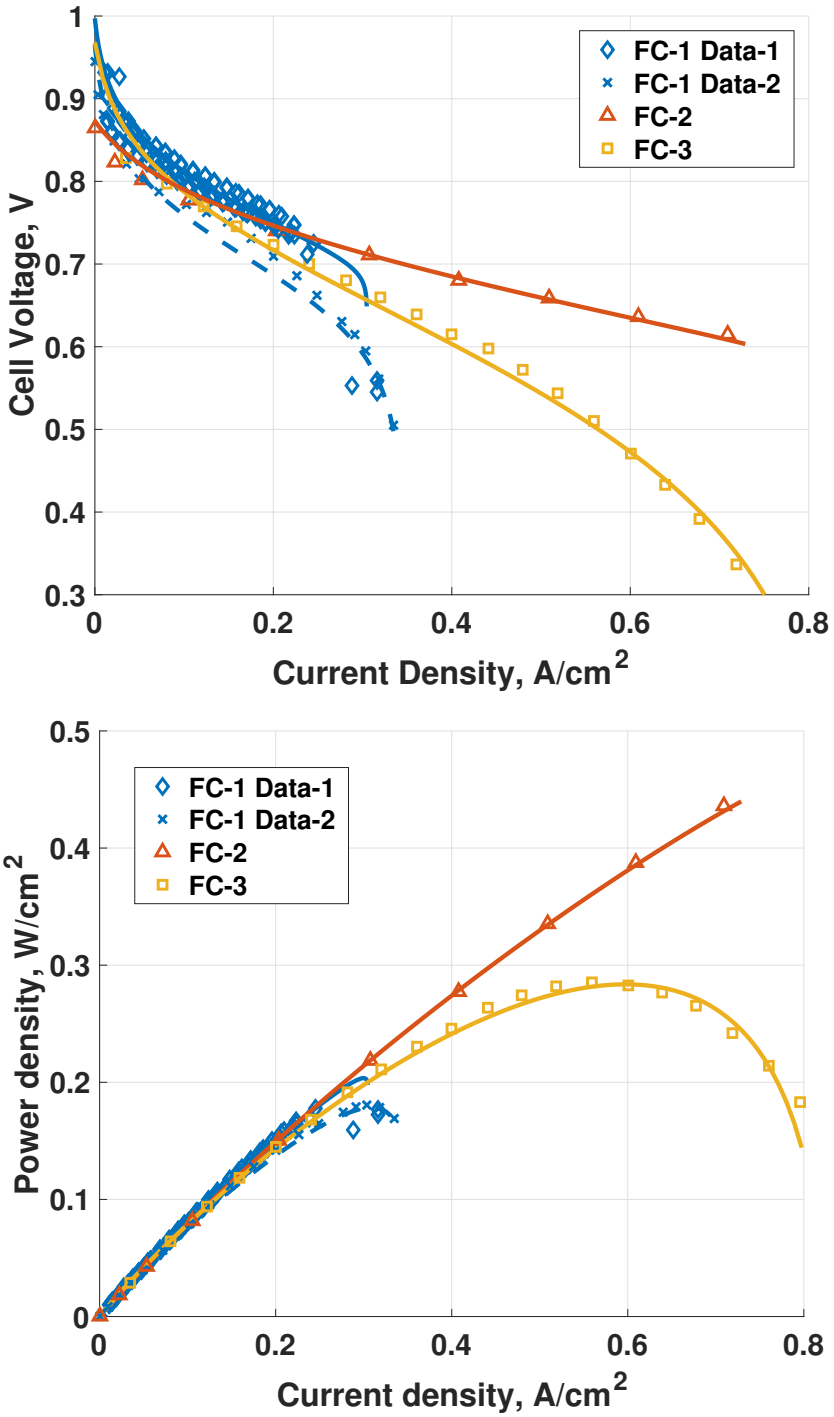

Figure 3.1: Steady state characteristics of three different fuel cells (FC-1 through 3 defined in text); cell voltage (top) and power density (bottom) versus current density; data and models.

At a given pressure (here, 1 atm) the steady-state characteristics depend

Table 3.1: Thermodynamic constants for fuel cell steady state models

	FC-1 Data-1	**FC-1 Data-1**	**FC-2**	**FC-3**
α_A	1.1	1.1	1.1	1.1
α_C	0.18	0.15	0.17	0.15
i_{0A}	3 e-4	3 e-4	3 e-4	0.1
i_{0C} (A/cm^2)	1 e-4	1 e-4	1 e-4	1 e-4
i_L (A/cm^2)	0.31	0.35	0.8	0.85
i_{leak} (A/cm^2)	0.005	0.005	0.04	0.01
C (V)	0.01	0.06	0.005	0.15
ASR_Ω (Ωcm^2)	0.2	0.002	0.13	0.07

mainly on the temperature and humidity of the anode and cathode. Cell-level data obtained from Ref. [39] were used to find the variation of the thermodynamic constants in Eq. 3.1 with temperature and humidity. Two out of the eight constants, the limiting current i_L and ohmic resistance ASR_Ω were found to capture the principal variations.

The resulting models for variations in operating temperature are shown in Fig. 3.2. The values of i_L and ASR_Ω are plotted against operating temperature in Fig. 3.3; they follow a quadratic behavior. The fuel stack used in the present hardware operates at a maximum temperature of 65°C. Assuming an operating temperature of 60°C, extrapolation of these trends would predict an ASR_Ω of around 0.3 Ω cm^2, which is slightly higher than the value found during steady state calibration (0.2 Ω cm^2). Extrapolation would also predict i_L of around 0.3 A/cm^2, which closely matches the calibrated value (0.31 A/cm^2).

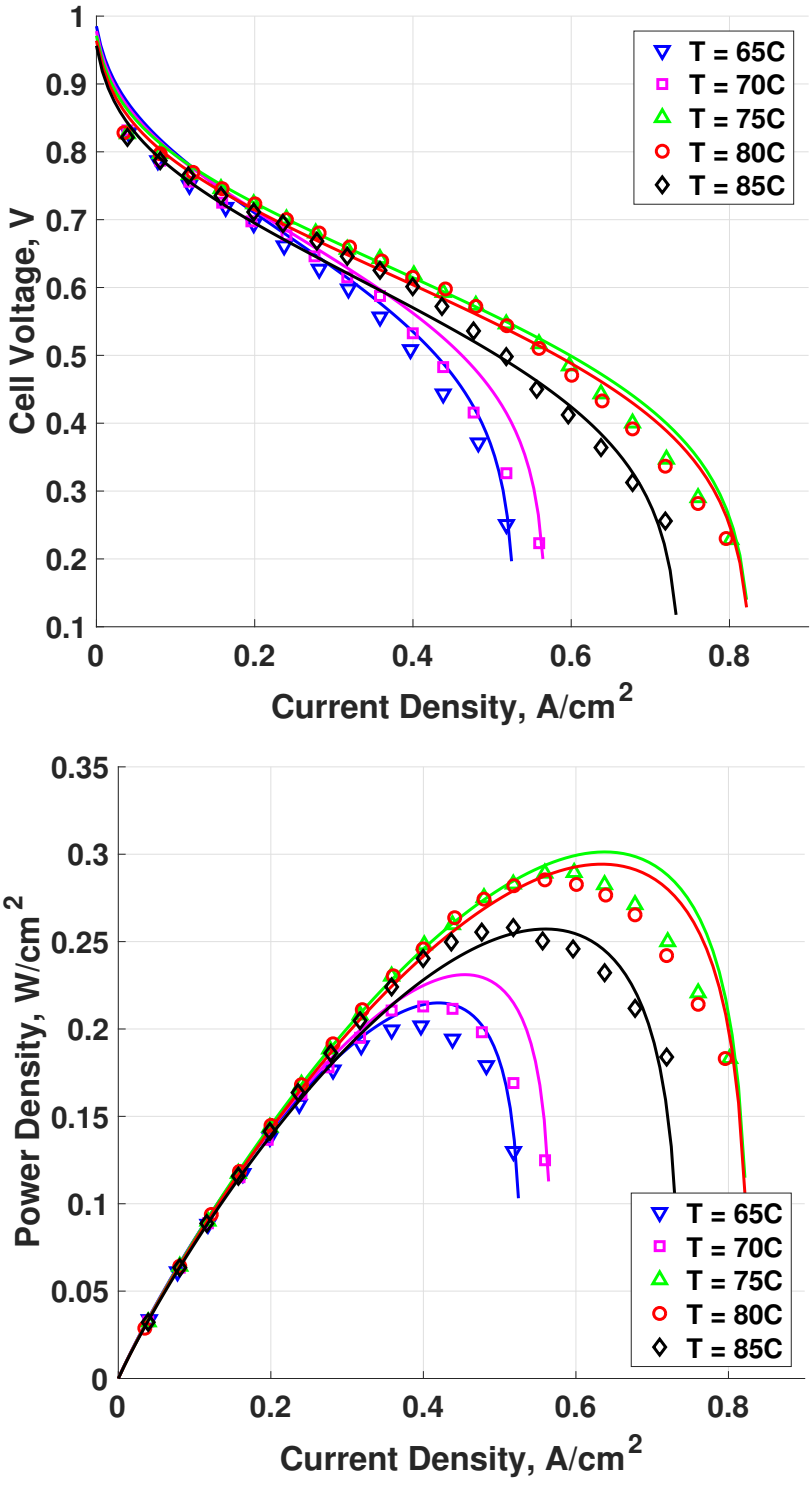

Figure 3.2: Steady state characteristics of a fuel cell over a range of operating temperatures at 1 atm; cell voltage (top) and power density (bottom) as a function of current density; solid lines show fitted models.

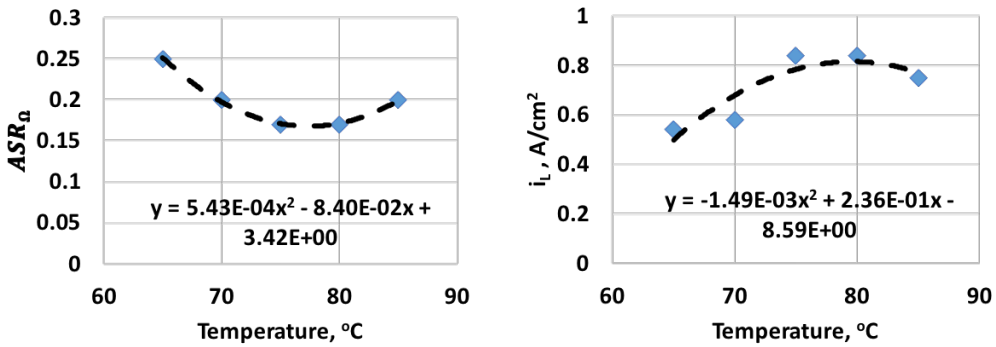

Figure 3.3: Variation of two main thermodynamic constants, area specific resistance (left) and limiting current (right), as a function of temperature; 100% anode and cathode relative humidity; y is the value of the constant, x is the temperature of the cell.

For variation with humidity, data at four different anode relative humidity (ARH) and cathode relative humidity (CRH) values were used from Ref. [39]. The same two constants were varied at each ARH over the range of CRH. The final constants are shown in Fig. 3.4. The individual trendlines for ASR_Ω are shown in Table 3.2.

To illustrate the use of these trends, consider for example a fuel stack operating at 70% ARH, 80% CRH and 65°C. The first step would be to use the first equation in Table 3.2 to calculate ASR_Ω for 70% ARH and 80% CRH, at 80°C. Then, a temperature correction would be made using the equation in Fig. 3.1 to calculate the difference between ASR_Ω at 65°C and 80°C. This difference would be added to the previous value of ASR_Ω. Similarly, the equation in Fig. 3.1 would first be used to calculate i_L for 70% ARH and 80% CRH at 80°C. The temperature correction would be made using the equation in Fig. 3.1 to calculate the difference between i_L at 65°C and 80°C. This difference would be added to the previous value of i_L.

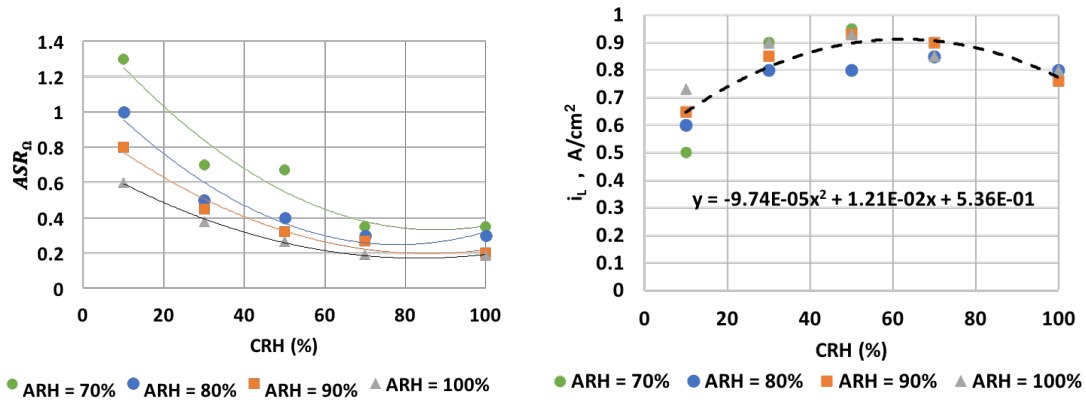

Figure 3.4: Variation in the two main thermodynamic constants, area specific resistance (left) and limiting current (right), as a function of cathode and anode relative humidity; temperature 80°C.

Table 3.2: Area specific resistance versus cathode relative humidity for various anode relative humidities; equations for trends in Fig. 3.1; temperature 80°C.

Anode Relative Humidity (%)	$y = ASR_\Omega; x = \%CRH$
70	$y = 1.53 \cdot 10^{-4}\ x^2 - 2.67 \cdot 10^{-2}\ x + 1.50$
80	$y = 1.52 \cdot 10^{-4}\ x^2 - 2.38 \cdot 10^{-2}\ x + 1.18$
90	$y = 1.00 \cdot 10^{-4}\ x^2 - 1.72 \cdot 10^{-2}\ x + 0.93$
100	$y = 0.783 \cdot 10^{-4}\ x^2 - 1.31 \cdot 10^{-2}\ x + 0.71$

The Sizing section assumes temperature T = 80 °C, CRH of 100%, and ARH of 100%.

3.2 Fuel Stack Transients

To model the fuel stack's transient operating characteristics, an ECN for a single polarization model was used, as shown in Fig. 3.5. E_r is the open circuit voltage. V and I are the voltage and current output by the fuel stack, respectively, where I is now a function of time. R_s is the electrolyte resistance (ohmic resistance in steady state) and R_{ct} is the charge transfer resistance causing a voltage drop across the electrode-electrolyte interface (activation and concentration losses in steady state). The capacitor C_{dl} (dielectric or double layer capacitance) accounts for the transients and models the effects of charge buildup in the electrolyte at the anode-electrolyte or cathode-electrolyte junctions.

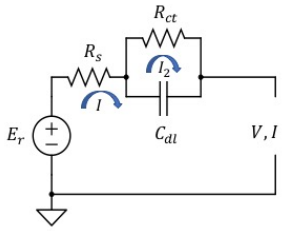

Figure 3.5: Basic equivalent circuit network of fuel stack.

The circuit in Fig. 3.5 can be represented by voltage balance around two current loops as follows.

$$E_r - R_s I - \frac{1}{C_{dl}} \int_0^t (I - I_2) dt - V = 0 \tag{3.2}$$

$$-R_{ct} I_2 - \frac{1}{C_{dl}} \int_0^t (I_2 - I) dt = 0 \tag{3.3}$$

Substituting Eq. 3.3 in Eq. 3.2 leads to Eq. 3.4, which gives the voltage supplied by the fuel stack as a function of current drawn from the fuel stack. Differentiating Eq. 3.3 leads to Eq. 3.5, which gives the branch current needed in Eq. 3.2.

$$\begin{aligned} V &= E_r - R_s I - R_{ct} I_2 \\ &= E_r - (R_s + R_{ct})I + R_{ct}(I - I_2) \\ &= \upsilon_{ss} + R_{ct}(I - I_2) \end{aligned} \tag{3.4}$$

$$R_{ct} C_{dl}\ \dot{I}_2 + I_2 = I \tag{3.5}$$

Here, $\upsilon_{ss} = E_r - (R_s + R_{ct})I$ is the steady-state cell voltage corresponding to Fig. 3.1, and is given by Eq. 3.1. This transient model collapses to steady state (i.e. $V = \upsilon_{ss}$) when $\dot{I}_2 = 0$ and $I_2 = I$.

An explicit equation for I_2 can be obtained for each new timestep $k+1$ by substituting a 3 point Euler backward approximation for $\dot{I}_2$ in Eq. 3.5,

$$\begin{aligned} &R_{ct} C_{dl} \left(\frac{1}{2\Delta t} I_{2_{k-1}} - \frac{2}{\Delta t} I_{2_k} + \frac{3}{2\Delta t} I_{2_{k+1}} \right) + I_{2_{k+1}} = I_{k+1} \\ &I_{2_{k+1}} = \left(1 - R_{ct} C_{dl} \frac{3}{2\Delta t} \right)^{-1} \left[I_{k+1} - R_{ct} C_{dl} \left(\frac{1}{2\Delta t} I_{2_{k-1}} - \frac{2}{\Delta t} I_{2_k} \right) \right] \end{aligned} \tag{3.6}$$

The values of the circuit components R_{ct} and C_{dl} were determined empirically. This was achieved by connecting the fuel stack output directly to an electronic

programmable load. A step current was drawn from the fuel stack and the transient voltage response was recorded. A sample of this data along with the empirically calibrated constants for two different current levels are given in Fig. 3.6 and Table 3.3. As depicted in Fig. 3.6 , the magnitude of the transient is R_{ct} times the size of the current step ΔI, and the time for the voltage to achieve steady state is approximately 4τ, where $\tau = R_{ct}C_{dl}$ is the time constant. For the response to a step input, the model is given by the following equation, where t is the time after the step change and ΔI is the magnitude of the step change.

$$V = E_r - \Delta I R_s - \Delta I R_{ct}\left(1 - e^{-t/\tau}\right) \tag{3.7}$$

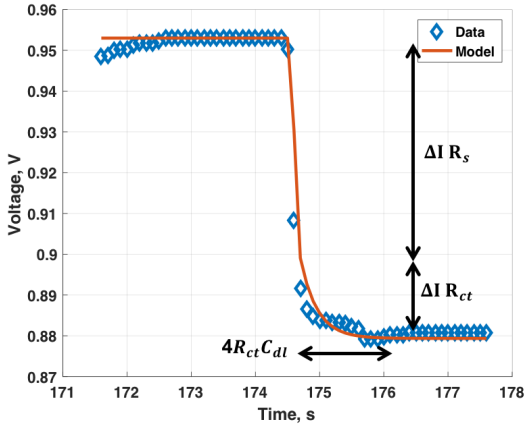

Figure 3.6: Voltage response to a step current drawn from a fuel stack.

The values of R_s, R_{ct}, and C_{dl} were found to depend on the magnitude of the current. They were calibrated separately for a very low current and a nominal current, as shown in Table 3.3. The resistor values are much lower at the nominal

current, which indicates that the transients are of smaller magnitude and duration than at low current. The value of $R_s + R_{ct}$ should correspond ideally with the ohmic resistance ASR_Ω, calibrated as 0.2 Ωcm^2 in Section 3.1. This difference in magnitude requires further investigation.

Table 3.3: Fuel stack ECN components calibrated for different current ranges

	Low Current	**Nominal Current**
Current Density, A/cm^2	0.01-0.04	0.07-0.18
$\mathbf{R}_s, \Omega\ cm^2$	2.57	0.60
$\mathbf{R}_{ct}, \Omega\ cm^2$	1.22	0.09
$\mathbf{C}_{dl}$**,** F	0.23	0.26
Time Constant, s	0.28	0.023

This basic ECN is as far as can be calibrated using step inputs without impedance spectroscopy. A more physically representative model is shown in Fig. 3.7. It includes two RC blocks – one associated with the cathode and one associated with the anode. Each RC block contains a resistance attributed to charge transfer and a capacitance attributed to the dielectric layer where charge builds up in the electrolyte at the electrode surface. The cathode RC block also includes a Warburg impedance in series with the resistor. The Warburg impedance is encountered by a charge diffusing through a dielectric field. It is most prominent in high current (i.e. high power) conditions, so it is of relevance to eVTOL aircraft.

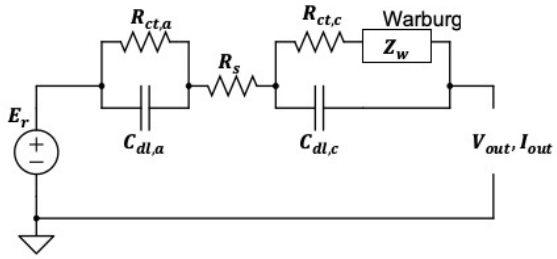

Figure 3.7: Physically representative equivalent circuit network of fuel stack; dual polarization blocks (anode and cathode) with Warburg impedance in cathode.

The Warburg impedance is a constant phase element that is difficult to represent in the time domain, as it leads to fractal systems described by fractional differential equations. It can, however, be approximated as a series of repeated RC blocks [45]. The resulting circuit diagram is shown in Fig. 3.8.

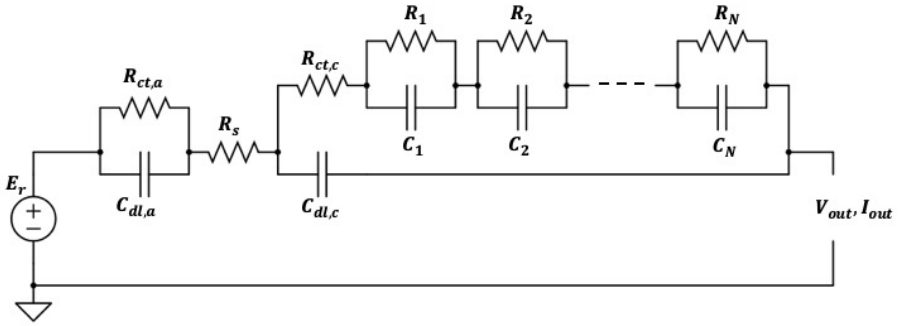

Figure 3.8: Equivalent circuit network of fuel stack with Warburg impedance approximated by RC blocks.

For this more refined circuit, the voltage supplied by the fuel stack is as follows.

$$V_{out}(t) = E_r - I_{out}(t)R_s - I_a(t)R_{ct,a} - I_c(t)R_{ct,c} - I_{R1}R_1 - ... - I_{RN}(t)R_N \quad (3.8)$$

where I_a is the current through $R_{ct,a}$, I_c is the current through $R_{ct,c}$, I_{R1} is the

branch current through R_1, and similarly for the other branches. Nodal analysis was used to find each of the unknown currents over time. For example, for the node between R_s, $R_{ct,c}$, and $C_{dl,c}$, the current equation is as follows.

$$\begin{aligned} I_c + I_{Cdl,c} &= I_{out} \\ I_c + C_{dl,c}\dot{v}_{Cdl,c} &= I_{out} \\ I_c + C_{dl,c}(\dot{I}_1 R_{ct,c} + \dot{I}_{R1}R_1 + ... + \dot{I}_{RN}R_N) &= I_{out} \end{aligned} \tag{3.9}$$

For each of the smaller branches, I_{RN} can be obtained using the same process. The final system of equations that describes the transient behavior is given by Eq. 3.8 and 3.10.

$$\dot{I}_c = -\frac{1}{R_{ct,c}\,C_{dl,c}}\,I_c - \frac{R_1}{R_{ct,c}}\,\dot{I}_{R1} \;\ldots - \frac{R_N}{R_{ct,c}}\,\dot{I}_{RN} + \frac{1}{R_{ct,c}\,C_{dl,c}}\,I_{out} \tag{3.10}$$

$$\begin{aligned} \dot{I}_{R1} &= -\frac{1}{R_1\,C_1}\,I_{R1} + \frac{1}{R_1\,C_1}\,I_c \\ &\ldots \\ \dot{I}_{RN} &= -\frac{1}{R_N\,C_N}\,I_{RN} + \frac{1}{R_N\,C_N}\,I_c \end{aligned}$$

Substituting the individual branch current derivatives into the first of Eq. 3.10 leads to the following single equation.

$$\dot{I}_c = \left(-\frac{1}{R_{ct,c}\,C_{dl,c}} - \frac{1}{R_{ct,c}\,C_1} \ldots - \frac{1}{R_{ct,c}\,C_N} \right) I_c + \frac{1}{R_{ct,c}\,C_1} I_{R1} + \ldots +$$

$$\frac{1}{R_{ct,c}\,C_N} I_{RN} + \frac{1}{R_{ct,c}\,C_{dl,c}} I_{out}$$

$$= a\,I_c + b_1\,I_{R1} + \ldots + b_N\,I_{RN} + b\,I_{out}$$

On the anode side, the differential equation is simpler.

$$\dot{I}_a = -\frac{1}{R_{ct,a}\,C_{dl,a}} I_a + \frac{1}{R_{ct,a}\,C_{dl,a}} I_{out}$$

All of these first order linear differential equations can be solved recursively to obtain the model output voltage V_{out} for a current draw I_{out}. Values at each new time step k are calculated based on the values at a single previous time step $k-1$.

$$I_{R1_{k+1}} = e^{-\frac{\Delta t}{R_1 C_1}} I_{R1_k} + \left(1 - e^{-\frac{\Delta t}{R_1 C_1}}\right) I_{ck}$$

$$\ldots\ldots$$

$$I_{RN_{k+1}} = e^{-\frac{\Delta t}{R_N C_N}} I_{RN_k} + \left(1 - e^{-\frac{\Delta t}{R_N C_N}}\right) I_{ck}$$

$$\begin{aligned} I_{c_{k+1}} &= e^{a\,\Delta t} I_{c_k} + \\ &\frac{1}{a}\left(e^{a\,\Delta t} - 1\right) b_1 I_{R1_{k+1}} + \frac{1}{a}\left(e^{a\,\Delta t} - 1\right) b_2 I_{R2_{k+1}} + \ldots + \\ &\frac{1}{a}\left(e^{a\,\Delta t} - 1\right) b_N I_{RN_{k+1}} + \frac{1}{a}\left(e^{a\,\Delta t} - 1\right) b\, I_{out_k} \end{aligned}$$

$$I_{a_{k+1}} = e^{-\frac{\Delta t}{R_{ct,a} C_{dl,a}}} I_{a_k} + \left(1 - e^{-\frac{\Delta t}{R_{ct,a} C_{dl,a}}}\right) I_{out_k}$$

Then substitute into Eq. 3.8

$$V_{out_{k+1}} = E_r - I_{out_{k+1}} R_s - I_{a_{k+1}} R_{ct,a} - I_{c_{k+1}} R_{ct,c} - I_{R1_{k+1}} R_1 - ... - I_{RN_{k+1}} R_N$$

An attempt was made to identify the resistor and capacitor values $R_1 ... R_N$ and

$C_1 ... C_N$, but the fuel stack voltage exceeded the limit for impedance spectroscopy. Instead, the test must be run on individual cells within the stack, which are not accessible in this fuel stack. This is expected to be possible on a higher grade fuel stack.

3.3 Battery Steady State Model

In a battery, the open circuit voltage E_r is no longer constant (like it is in the fuel cell), but instead is a function of the battery's state of charge (SOC). The SOC describes the fraction of charge remaining in the battery over the total charge C (Ah) possible for supply. In its simplest form, it is given by Eq. 3.11, where I is the current drawn in Amperes, and t is the time in hours.

$$\begin{aligned} SOC &= 1 - \frac{1}{C}\int I dt && \text{for discharge} \\ &= \frac{1}{C}\int I dt && \text{for charge} \end{aligned} \tag{3.11}$$

However, C itself can be a function of I, so this equation is hard to apply when the current changes with time. Typically, for lithium-ion (Li-ion) batteries, $C = C_{REF}/\alpha\beta$, where C_{REF} is capacity at a reference current I_{REF} and $\alpha(I)$ and $\beta(T)$ are rate factors associated with other currents and temperatures. Then, a more appropriate expression for SOC is,

$$SOC = 1 - \frac{1}{C_{REF}} \int \alpha \ \beta \ I \ dt \qquad \text{for discharge} \tag{3.12}$$
$$= \frac{1}{C_{REF}} \int \alpha \ \beta \ I \ dt \qquad \text{for charge}$$

The rate factors α and β have to be determined empirically. The quantity Idt is the actual amount of charge supplied or delivered to the load; the quantity $\alpha\beta Idt$ is a notional amount of charge released or depleted from the battery with which the state of charge SOC is to be calculated.

A representative set of rate factors based on Ref. [22] are,

$$\alpha(I) = 1 + 0.4 \left(\frac{I}{I_{REF}} - 1 \right) \frac{I_{REF}}{C_{REF}} \tag{3.13}$$

$$\beta(T^{\circ}C) = 1 - 0.02093(T - T_{REF}) \qquad \text{where } T_{REF} = 23^{\circ}C \tag{3.14}$$

where I is the instantaneous current and I_{REF} is a reference current in amperes for a reference capacity C_{REF} in Ah. For example, if a battery is rated (0.3 C) 33 Ah, then $C_{REF} = 33$ and $I_{REF} = 0.3 \times 33$, so $I_{REF}/C_{REF} = 0.3$.

Temperature also reduces the open circuit voltage (at all SOC).

$$\Delta E_r = 0.011364(T - T_{REF}) \tag{3.15}$$

The variation in E_r with SOC means there is not a unique steady state i-υ curve as with the fuel stack. As current is drawn, the SOC and E_r drop. This effect must be modeled. A fully empirical model based on the classical work of Shepherd [46] is adopted. For a constant current draw per unit area i, the Shepherd model has the following form.

$$\upsilon = E_r - iN \tag{3.16}$$

where

$$E_r = E_s - \frac{K}{SOC} i + A \exp\left[-B(1 - SOC)\right] \tag{3.17}$$

E_r is the open circuit voltage and υ is the battery output voltage. E_s is a constant potential in volts, K is a polarization coefficient in Ω-area, N is the internal resistance times unit area in Ω-area, and A in volts and B (unitless) are empirical constants. SOC is the area specific state of charge. The original Shepherd model uses SOC from Eq. 3.11; if α and β are available, Eq. 3.12 should be used instead. In total, 4 empirical constants: E_s, K, A, and B describe the open circuit voltage E_r as a function of SOC, and the additional constant N is the resistance needed for closed circuit voltage υ.

To calibrate the model for E_r, the battery was connected directly to a battery analyzer which discharged the battery at a very low constant i and measured υ. The unit area was defined as the area of the cell, so the current density (current per unit area) is equivalent to the total current drawn from the battery. N was taken to

be the summation of R_s and R_{ct}, the internal resistances of the battery, which were calibrated using the same method described in Section 3.2 for the fuel stack – by drawing a step current and recording the resulting voltage. The remaining values were calibrated empirically based on the discharge data.

The discharge data are shown in Fig. 3.9 and 3.10 for a 30 C, 2800 mAh, 3 cell Li-ion battery. Figure 3.9 uses a model based on the six empirical constants extracted from the 0.07 C discharge data (lowest current), and shows how the model performs at higher currents. Figure 3.10 uses empirical constants extracted from the 3.6 C discharge data (highest current) and shows how the model performs at lower currents. The main cause of this discrepancy at high currents is the change in K with current, obvious from Fig. 3.10, which shows how the model performs when the constants are extracted using data from 3.6 C. Here, the discrepancy is shifted to low currents. None of this is surprising; even though the Shepherd constants have some basis in underlying phenomena, empirical models are always inadequate as prediction models; at best the constants can be evaluated for several current levels, as shown in Table 3.4. The resistance N was extracted from step input experimental data, and is equivalent to $R_s + R_{ct}$ of the battery from Table 3.5 presented later. The capacity C was extracted by fitting the constant current discharge data. This value is consistent with the discharge capacity that was measured for each test by multiplying the current and the duration of discharge (i.e. calculating the integral of current over time). The capacity measured during the discharge test is slightly lower than the empirically fit total capacity C, because the discharge test was stopped when the battery voltage reached 9 V to avoid damaging the battery. Most of the

constants vary with the operating current. In this table, 'area' refers to the same unit of area as that in 'current per area' i.

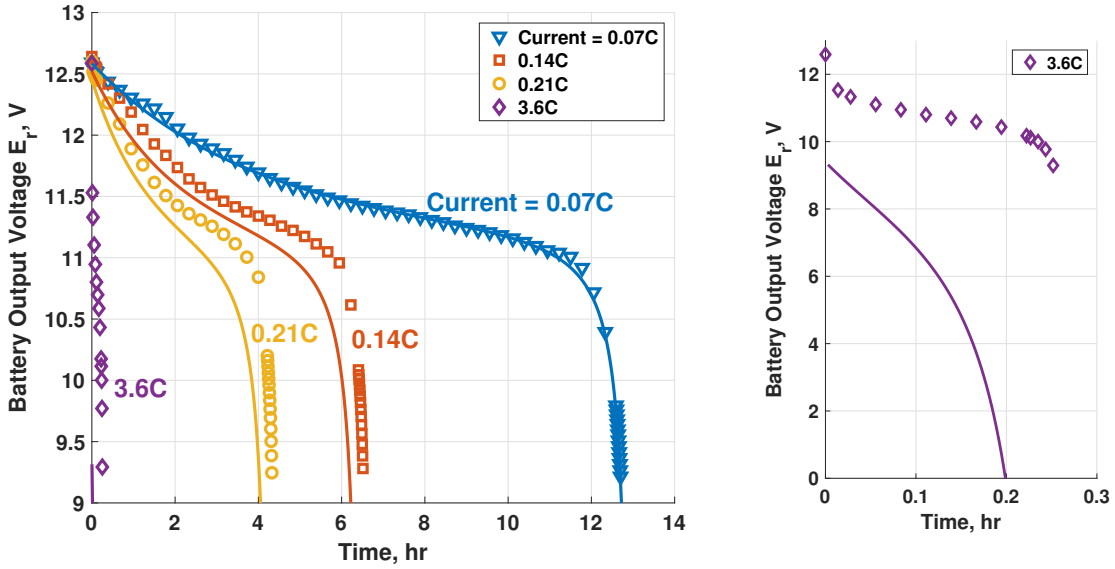

Figure 3.9: Discharge model compared to test data; right side is a close-up; model parameters extracted at 0.07 C.

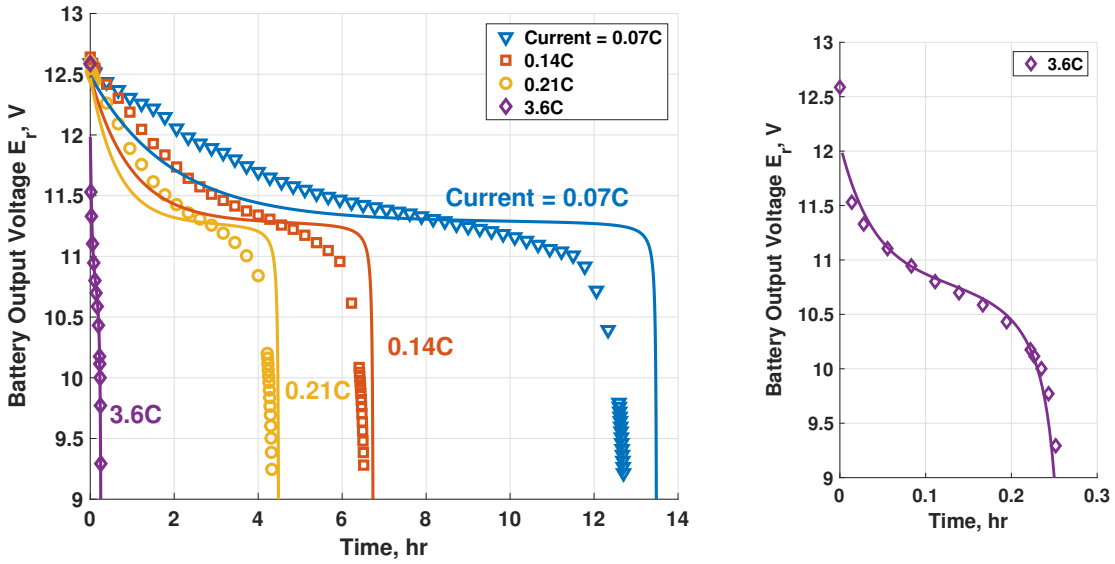

Figure 3.10: Discharge model compared to test data; right side is a close-up; model parameters extracted at 3.6 C.

A sensible procedure would be to extract the Shepherd model at very low currents (less than 0.1 C), resembling an open circuit as closely as possible, extract

the resistances using step inputs, and let the rate factor α handle the effect of current on capacity (and β to handle the effect of temperature). The error in K will still appear at higher currents, but it will be conservative (less voltage predicted), and the gross trends acceptable for at least a conceptual level of aircraft design. Alternatively, the constant K can be extracted at a range of different currents, and an exponential trend can be fit to obtain the value of K as a function of current.

Table 3.4: Shepherd battery model constants for 2800 mAh, 30C, 3 cell lithium polymer battery

	Very Low Current	**Low Current**	**Nominal Operating Current**
Discharge Current, A	0.2	0.4-0.6	10
Discharge C-rate, h^{-1}	0.07	0.14	3.6
Discharge Capacity, Ah	2.54	2.61	2.54
E_s**, V**	11.3	11.3	11.3
K, **Ω-area**	0.25	0.1	0.015
Q**, Ah/area**	2.6	2.65	2.7
N, **Ω-area**	0.076	0.076	0.028
A**, V**	1.35	1.35	1.2
B	3.4	3.4	7.0

3.4 Battery Transient

The transient behavior of a battery can be modeled by the same equivalent circuit network (ECN) as the fuel cell, for both are DC electrochemical sources. However, the open circuit voltage E_r is now a function of the state of charge (SOC). Many transient Li-ion battery ECN models have been developed in the past two decades for design of power systems in consumer electronics (see Ref. [22, 48] for example) and hybrid-electric cars (see Ref. [24, 25]). All of these models are semi-empirical and require extensive battery testing for temperature and frequency effects. The $E_r(SOC)$ would also have to be input separately as a function of temperature for all models.

The Shepherd model for $E_r(SOC)$ is retained to capture the nonlinear behavior of the steady-state and paired with an ECN model to capture the generally linear behavior of the transients. The transient model uses the same circuit diagram shown earlier in Fig. 3.5. The constants R_s, R_{ct}, and C_{dl} are extracted using the same method as the fuel stack. The results for low and nominal current ranges are presented in Table 3.5.

Table 3.5: Battery ECN components calibrated for different current ranges

	Low Current	**Nominal Current**
Current, A	0.01-2.4	9.3-13.5
C-rate, $\mathbf{h^{-1}}$	0.0036-0.86	3.32-4.82
$\mathbf{R_s}, \Omega$	0.042	0.021
$\mathbf{R_{ct}}, \Omega$	0.034	0.007
$\mathbf{C_{dl}}$, F	268.15	242
Time Const, s	9.12	1.69

While the capacitor values are higher compared to the fuel stack, the resistor

values are lower. This manifests as voltage transients of a lower magnitude but longer settling time compared to the fuel stack. The time constant of the battery is approximately one order of magnitude larger than that of the fuel stack.

An ECN including a model for E_r was explored, based on Ref. [47] and shown in Fig. 3.11. However, it is comprised of linear circuit components, which are unable to capture the highly nonlinear behavior of E_r as a function of SOC. Thus, the Shepherd model is still more accurate.

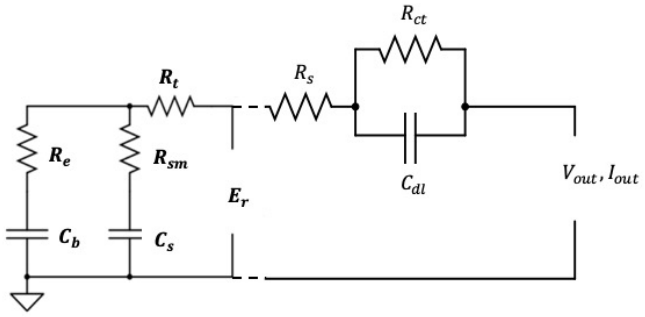

Figure 3.11: Equivalent circuit network of a battery, including E_r model, based on [47].

Chapter 4: Model Verification

For Li-ion batteries and PEM fuel stacks to be used in eVTOL, they must be able to respond to rapid transients caused by maneuvers or electrical faults. Experimental data were acquired to verify the models in the presence of these rapid transients.

4.1 Fuel Stack Test

Figure 4.1 shows fuel cell voltage (measured for the entire stack and divided by the total number of cells) with intentionally high amplitude and frequency transients. The results indicate that the model is generally capable of capturing the amplitude and waveform of the fuel stack's transient i-v characteristics. A small vertical shift is visible between model and experimental voltage, which can be attributed to measurement error or variations in temperature and humidity between the time of this test and the time of the steady-state model calibration (used to find v_{ss} in Eq. 3.4). The primary error in the model occurs at the beginning of the test, which appears as a longer transient behavior that occurs upon startup of the fuel stack, not captured by the present model.

The transient model is compared to the steady state in Fig. 4.1. This steady

state model based on the FC-1 Data-1 model in Fig. 3.1. This comparison reveals the first major conclusion: the transient model is almost identical to the steady state model. The steady state model is capable of capturing almost all of the behavior in the normal range of operating currents, so the transients in the fuel stack are not very significant. This is a reflection of the fact that the values of R_{ct} and C_{dl} in Table 3.3 are fairly small for the normal operating current range. The error at the beginning of the test duration is perhaps due to a second, larger internal capacitance not captured by the ECN used in this model.

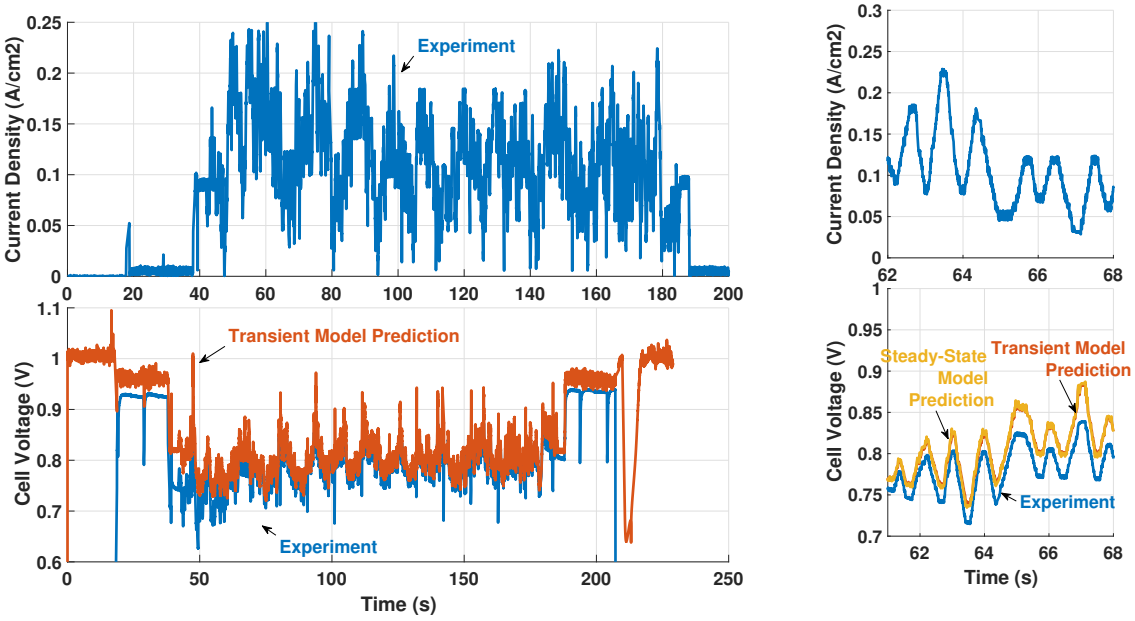

Figure 4.1: Model compared to experimental voltage for fuel stack for highly transient load; right side is close-up with additional steady state model.

4.2 Battery Test

Similar data were collected for the LiPo battery (Fig. 4.2). The model in this figure uses the empirical constants from the third set presented in Table 3.4. All three sets of constants were investigated and showed very small differences of less than 0.15 V. Comparison revealed the second key conclusion: unlike the fuel stack, here, the transient model is different from the steady-state model, and in general provides an improved waveform. However, like in the fuel stack, there is again a vertical shift between the model and experimental voltage. The experimental voltage is lower, so it cannot be due to heating (rise in temperature increases voltage), but perhaps due to rate effects at higher currents (higher current reduces voltage), not included in the model ($\alpha = 1$ in the model). Additionally, discrepancies could be due to the battery's total capacity degrading over use; the constant voltage discharge data used to calibrate the model was collected after the transient experiment, and the battery's capacity had reduced from a nominal 2.8 Ah to a lower 2.6 Ah.

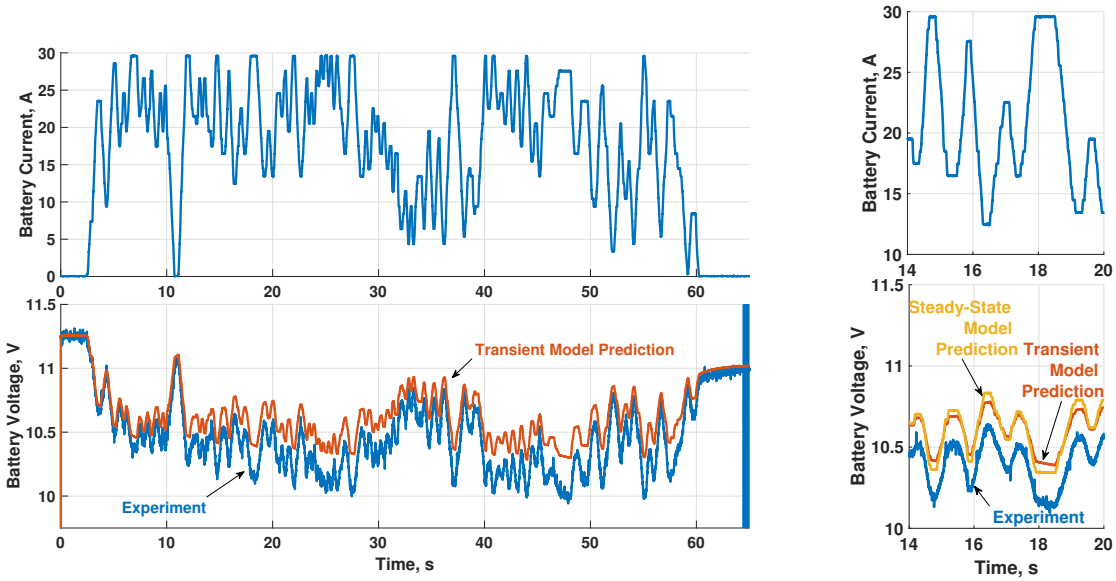

Figure 4.2: Model compared to experimental voltage for battery for highly transient load; right side is close-up with additional steady state model.

Key conclusions from this transient modeling is that transients are not critical for powerplant sizing at the conceptual design stage, and that the fuel stack has in fact a faster response than the battery.

Chapter 5: Demonstration of Power Sharing

5.1 Unregulated

A 3-cell LiPo battery and the 300 W PEM fuel stack are connected in parallel and used to power a quadcopter. An electrical tether is used to deliver power from the on-ground powerplant, as shown in Fig. 5.1. The data from each power source and the quadcopter load are shown in Fig. 5.2. The flight test demonstrates the viability of using the two power sources together in a hybrid powerplant. The architecture for the unregulated system is trivial; the two components are connected in parallel with only a diode in series with the fuel stack and a DC-DC step-down converter, the same arrangement shown earlier in Fig. 2.1 and 2.2. The DC-DC step-down reduces the fuel stack voltage (˜50V) to the order of magnitude of the battery voltage (˜12.3V) and the diode prevents current flow backwards towards the fuel stack. The power sharing is not regulated at all; the two components are left to operate based solely on their natural i-v characteristics. The key conclusion from Fig. 5.2 is that they form a natural combination working in tandem – the battery voltage drops with depleting SOC, diminishing its share of power. This causes the fuel cell voltage to also drop, increasing its share of power (Fig. 3.1). Thus, the total power supply is maintained. This is why a parallel configuration is used for the

battery and fuel stack, rather than a series configuration. However, even in parallel, regulation would be required to force them to not work in tandem, but instead share the supply of power as desired. This is an essential requirement for eVTOL, where the fuel stack is sized to low power cruise mode and the battery supplements during high power segments of the mission to minimize powerplant weight.

Figure 5.1: Quadcopter flight test with electrical tether for power delivery.

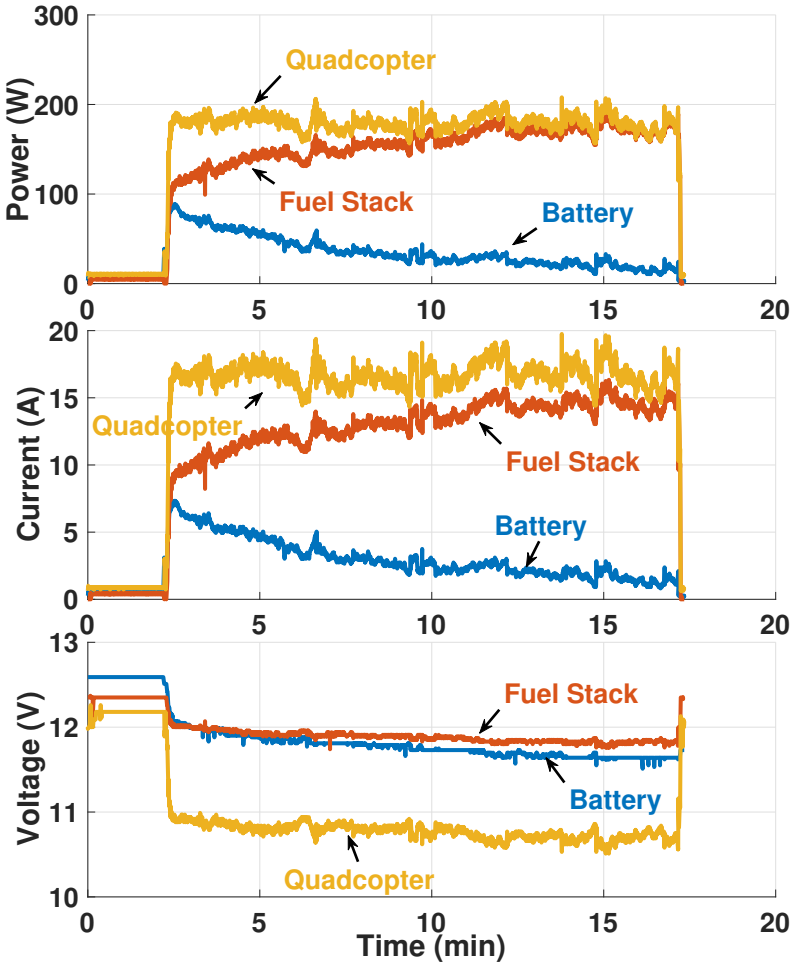

Figure 5.2: Experimental power, current, and voltage of battery, fuel stack, and quadcopter during hover.

This unregulated parallel configuration will serve as a control case to compare with various regulated power-sharing architectures in the next section. A circuit

schematic of the unregulated configuration is shown in Fig. 5.3. The circuit is used to provide power to an electronic load. The load follows a notional power profile for an eVTOL mission, consisting of two high-power segments representing hover and take-off or landing and a low-power segment representing cruise. These data are shown in Fig. 5.4. The power plot shows a non-optimal power sharing behavior, where both the battery and fuel stack need to be sized to the maximum power (exhibited at the beginning and end of the test, respectively). In the following section, a regulated architecture is developed to maintain optimal power sharing over the course of the mission.

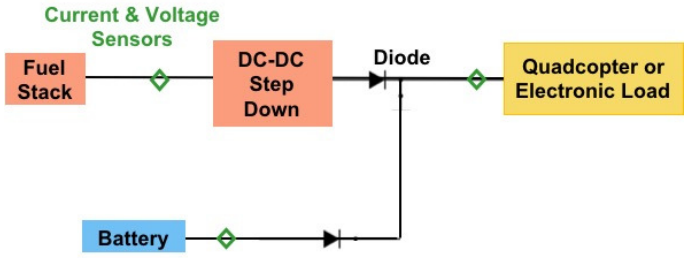

Figure 5.3: Circuit schematic for unregulated parallel configuration.

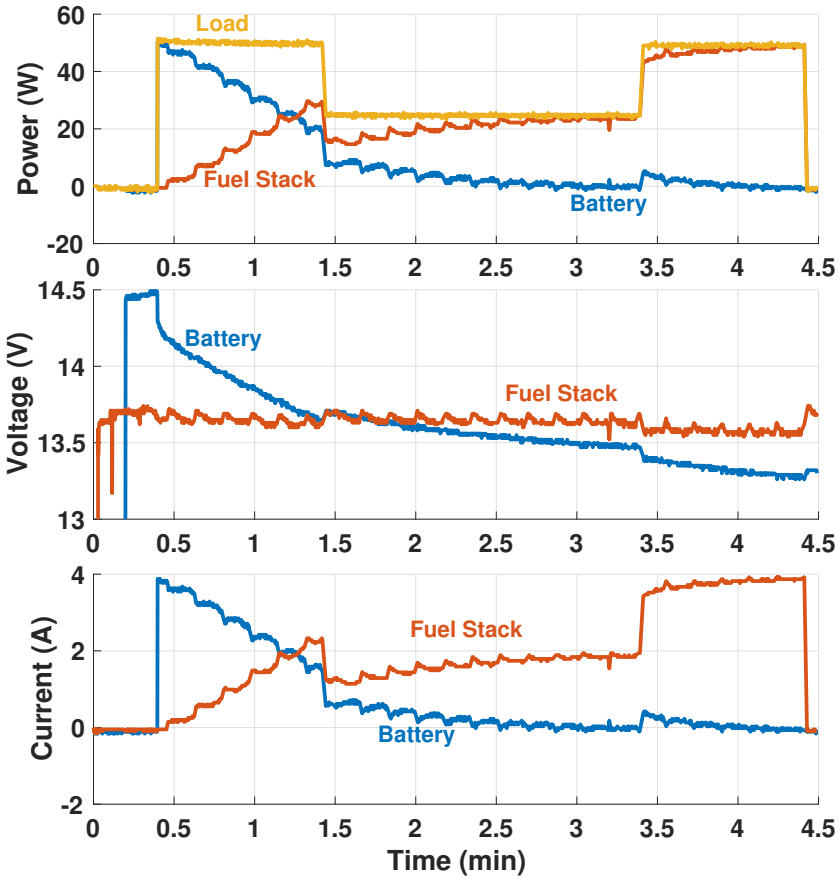

Figure 5.4: Measured power, voltage, and current of battery and fuel stack in unregulated parallel configuration for a notional eVTOL mission.

Note that the jaggedness of the fuel stack and battery data is due to the fuel stack short circuiting every 10 seconds, as described in Chapter 2. The fuel stack voltage drops to zero for 100 ms, and the battery power naturally surges to compensate. The localized drops and surges are filtered out to simulate data from a high-grade fuel stack, which would not exhibit this behavior. However, there are some transient aftereffects, leading to the periodic jaggedness seen in the data.

5.2 Regulated

The previous sections have shown that a battery and fuel cell can easily function in an unregulated parallel configuration and share the load of a quadcopter in flight. However, this is not the desired use of energy over the course of a mission. An optimal power sharing scheme for a notional eVTOL mission is illustrated in Fig. 5.5. In designing a minimum weight powerplant, the key factor is that the hydrogen source (i.e. the fuel stack) has high energy density, so its weight is driven by required power; the battery has high power density, so its weight is driven by required energy. A regulated system would conserve battery energy and use hydrogen energy whenever possible, because hydrogen energy is more weight-efficient. The battery would only be used during high power portions of the mission to supplement the fuel stack, allowing the fuel stack to be designed to a lower power and thus lower weight, and the battery to be designed to a lower energy and thus lower weight. Additionally, if the battery is depleted, any excess power from the fuel stack can be used to recharge the battery when the aircraft power demand is low.

In the unregulated case, the load sharing would behave as shown earlier in Fig. 5.4. In the regulated case, the battery no longer discharges during the low-power phases: idle, cruise, and spin down. Thus, less power is drawn from the battery and more from the fuel stack. The regulated power sharing strategy reduces the total weight of the powerplant compared to the unregulated strategy because batteries suffer from low specific energy but can provide higher specific power. Covering contingencies like failure of a battery or fuel stack would require additional power.

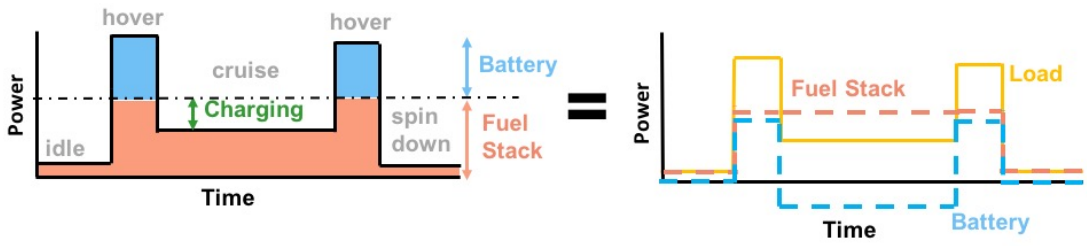

Figure 5.5: Power supplied by fuel stack and battery in regulated operation for a notional mission power profile.

Baseline: Charge and Discharge Switches

To implement the regulated power sharing architecture, a circuit was constructed as shown in Fig. 5.6. The fuel stack and battery are still connected in parallel with a diode to prevent current flow into the fuel stack. The additions compared to the unregulated circuit are the two switches and diodes to control charging or discharging of the battery. The switches are voltage controlled solid state relays activated by an Arduino. When the relay in the left branch is closed, the diode in that branch limits the current flow so that the battery can only discharge. When the relay in the right branch is closed instead, the diode in that branch channels the current flow in the direction to charge the battery.

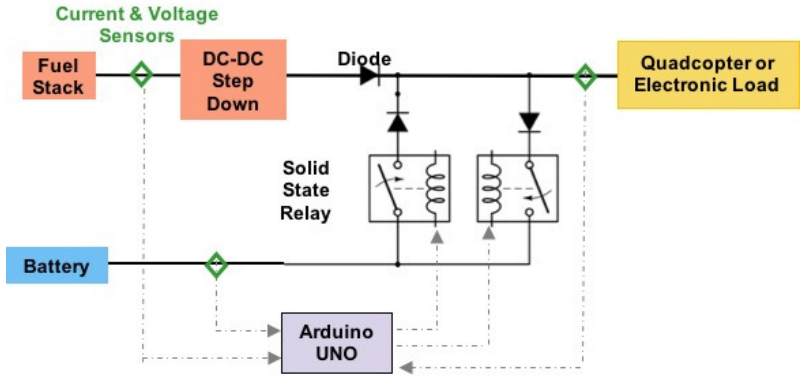

Figure 5.6: Circuit schematic for regulated power sharing operation.

The Arduino sets the switches open or closed depending on the battery voltage and load power. The various operating states are described below and listed in Table 5.1.

- State 1: The battery is fully charged and the load power is low. All the power is supplied by the fuel stack, and the battery is completely disconnected from the circuit. Charging is not allowed to avoid overcharging the battery.

- State 2: The battery is fully charged and the load power is above that which can be supplied by the fuel stack alone. The battery discharge switch is closed, allowing the battery to share the load with the fuel stack.

- State 3: The battery is partially depleted but still above its safe minimum voltage. The load power is low. The battery is prevented from discharging because the fuel stack is capable of providing all the necessary power to the load. The fuel stack uses any excess power available to charge the battery.

- State 4: The battery is in the same range as State 3, but the load power is above that which can be supplied by the fuel stack alone. The battery discharge switch is closed, allowing the battery to share the load with the fuel stack.

- State 5: The battery is completely depleted to its minimum safe voltage. The load power is low. The battery discharge switch is open so it cannot provide power to the load. The fuel stack provides all the power to the load. The fuel stack uses any excess power available to charge the battery.

Table 5.1: Operating states of regulated power sharing control circuit.

State	Battery Voltage	Load Power	Switch States		Power Source
			Dischg	Chg	
1	High	Low	0	0	Fuel Stack
2		High	1	0	Fuel Stack + Battery
3	Medium	Low	0	1	Fuel Stack (Charge Battery)
4		High	1	0	Fuel Stack + Battery
5	Low	Low	0	1	Fuel Stack (Charge Battery)
6		High	0	0	Fuel Stack
7	Battery Current Too High		0	0	Fuel Stack

- State 6: The battery is completely depleted but the load power is above the maximum fuel stack power. However, to prevent damaging the battery, it is still not allowed to discharge. If this case is ever reached, the battery was not sized adequately for the mission.

- State 7: If the battery charge or discharge current exceeds the maximum rated current, the switches open to disconnect it from the circuit as a safety precaution.

The first six states are demonstrated experimentally in Fig. 5.7. For this demonstration, the cutoff for 'high' or 'low' load was 20 W and indicated by a dashed line in the power plots. This is an arbitrary number chosen for illustration purposes. The cutoff for high battery voltage was 12.3 V and the cutoff for low battery voltage was 11.3 V. Both are plotted as dashed lines in the voltage plots. The Dchg and Chg lines indicate the time segments where the battery is discharging and charging, respectively. The boxes and numbers in the bottom plots indicate the

corresponding states of operation.

When the fuel stack and battery are sharing power (cases 3 and 5), the sum of the fuel stack and battery currents equal the current received at the load ($I_{fs}+I_{bat} = I_{load}$). The sum of the fuel stack and battery power is slightly greater than the power received by the load ($P_{fs} + P_{bat} > P_{load}$), due to losses across the diodes and wires. The same is true for the other cases – current is the conserved quantity and accurately illustrates the sharing of power, whereas power is not conserved due to losses in the circuit.

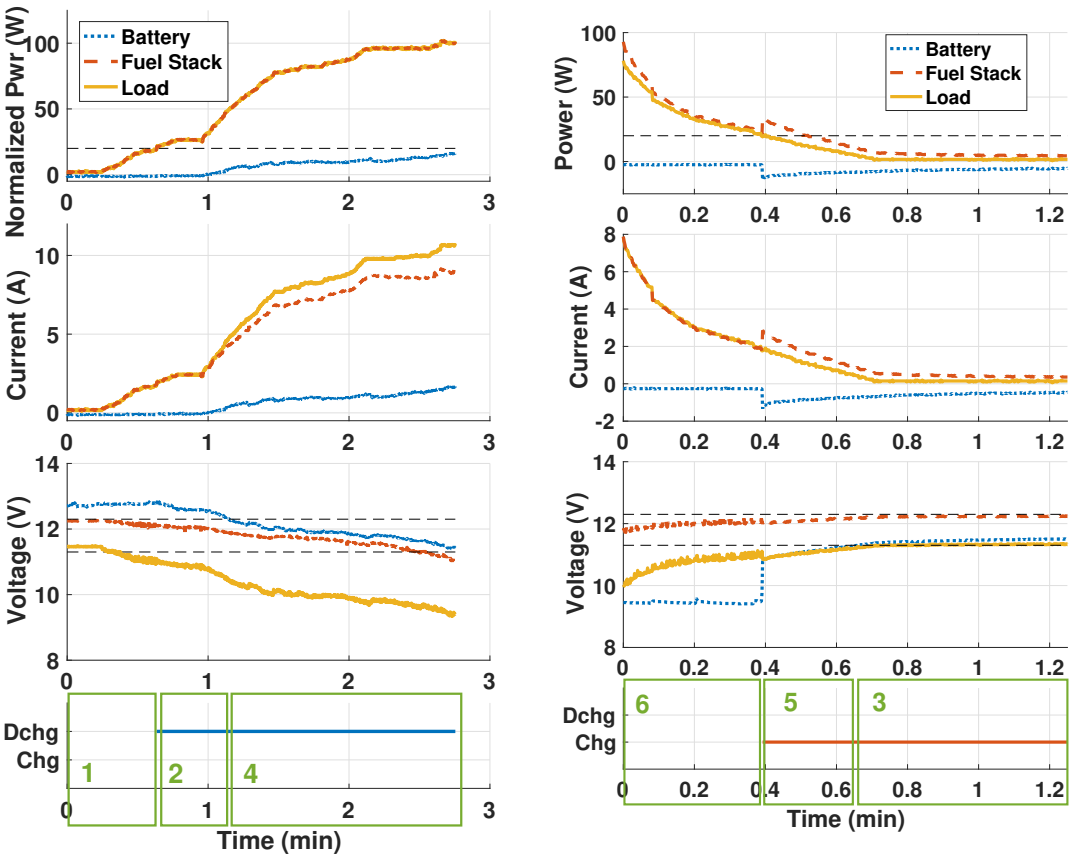

Figure 5.7: Demonstration of power sharing circuit's six operating modes.

The same notional mission power profile from the unregulated circuit was placed on this circuit, and the results are shown in Fig. 5.8.

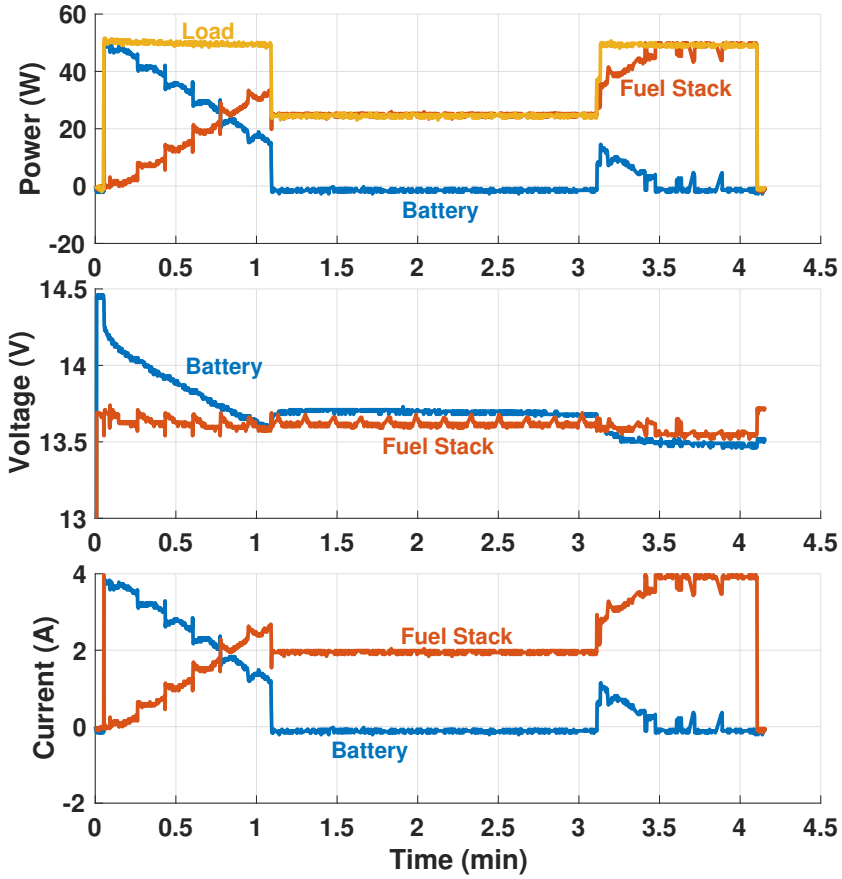

Figure 5.8: Measured power, voltage, and current of battery and fuel stack in a regulated parallel configuration for a notional eVTOL mission with switches to contorl charging and discharging.

This shows an improvement from the unregulated configuration data in Fig. 5.4. The battery is now turned off during the low power segment, thus conserving the battery energy. In this segment, the fuel stack is operating at its design power, and expending hydrogen, the comparatively light-weight energy source. This makes the overall system lighter. However, the desired charging of the battery is not observed. This is because the battery voltage is still higher than the fuel stack voltage, as seen in the bottom plot of Fig. 5.8, so there is insufficient voltage potential with which to charge the battery. Additionally, the power sharing ratio is not held constant as

desired for the ideal case. At the beginning of the test, the battery is providing all the power, which means battery energy is being consumed when it is not needed, and the fuel stack is not operating at its maximum design power. Then, at the end of the test, the fuel stack is providing all the power, which means the fuel stack would have to be sized to that high power, and therefore much heavier than the ideal scenario.

Refinement 1: Constant Current Charging

To address the inability to charge, a DC-DC constant current step-up converter was incorporated into the charging branch of the circuit, as shown in Fig. 5.9. It increases the voltage that the battery receives during the charging modes, and delivers a constant current (set by the user using a potentiometer) to charge the battery. The data from the same power profile with this circuit is shown in Fig. 5.10.

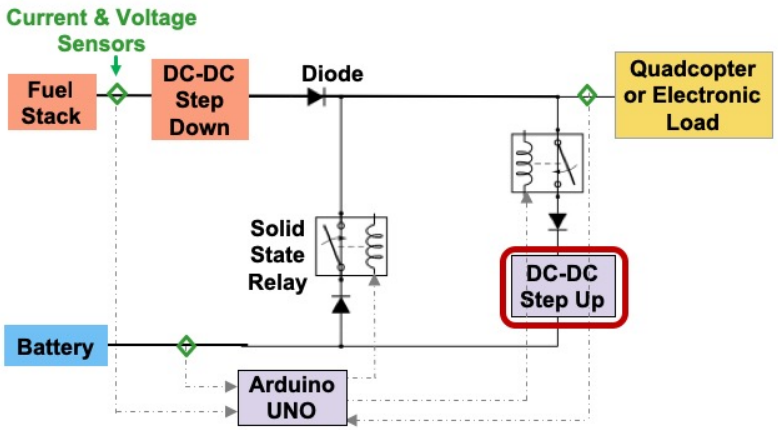

Figure 5.9: Circuit schematic for regulated power sharing operation with added DC-DC converter for constant current charging.

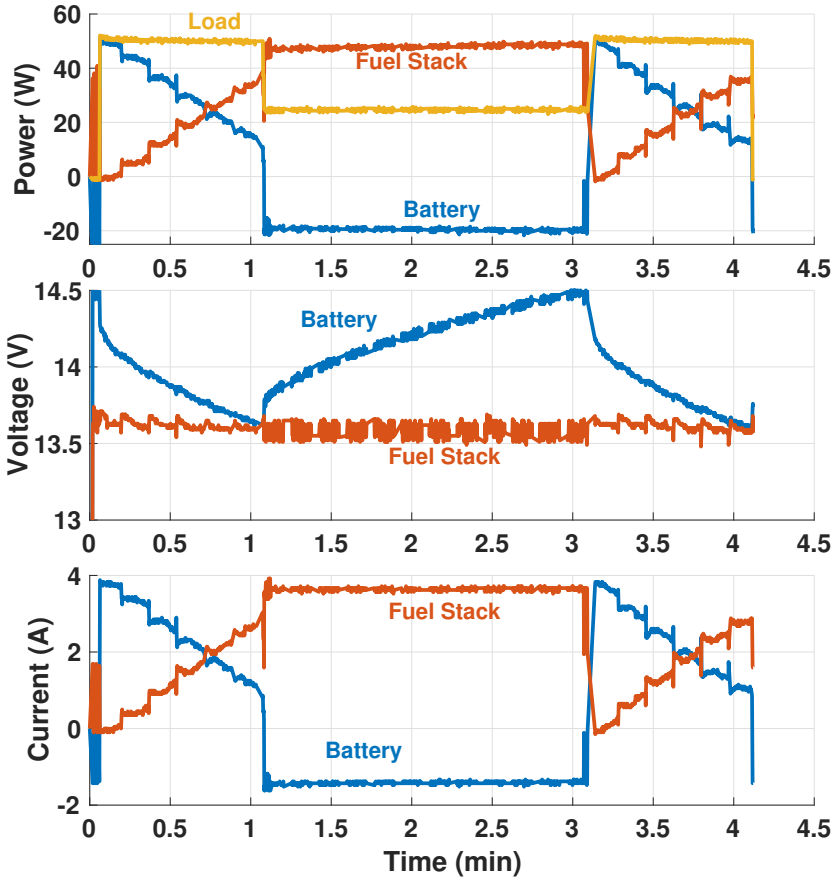

Figure 5.10: Measured power, voltage, and current of battery and fuel stack in a regulated parallel configuration for a notional eVTOL mission with added DC-DC converter for constant current charging.

In this test, the fuel stack is charging the battery in the low power segment, indicated by the negative battery power and increasing battery voltage. However, the power sharing ratio is still not constant.

Refinement 2: Constant Voltage Discharge

To address the above problem, a DC-DC buck-boost converter was incorporated into the discharging branch of the circuit, as shown in Fig. 5.11. This component allows the user to set a constant voltage for the battery power delivery,

regardless of the battery voltage, which changes with state of charge of the battery.

The data from the test of this circuit are shown in Fig. 5.12.

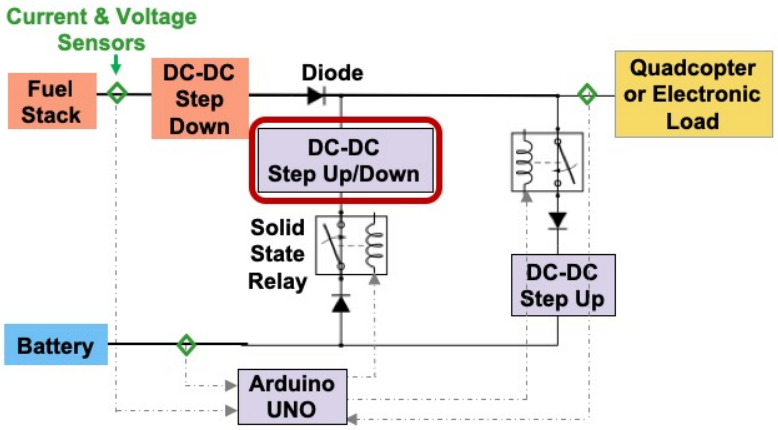

Figure 5.11: Circuit schematic for regulated power sharing operation with added DC-DC converter for constant voltage discharging.

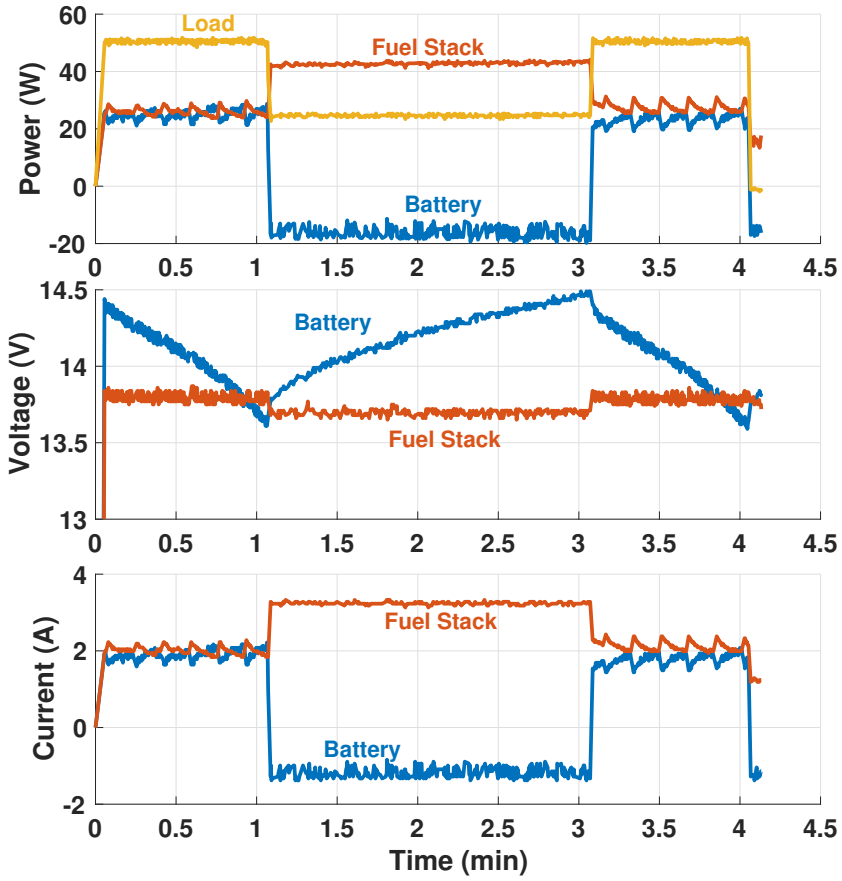

Figure 5.12: Measured power, voltage, and current of battery and fuel stack in a regulated parallel configuration for a notional eVTOL mission with added DC-DC converter for constant voltage discharging.

This circuit achieves control over power sharing and charging that is necessary to achieve the ideal power sharing scenario in Fig. 5.5. The remaining difference is that the fuel stack power contribution is not constant over the course of the mission. The fuel stack is not operating at its full power during hover, forcing the battery to supplement more power, which indicates that the battery is larger than necessary to complete the mission. This can not be corrected for by changing the circuit, but instead would be corrected for by designing the powerplant (i.e. fuel stack and battery size) to fit this specific mission. The powerplant for this mission would have

a reduced capacity battery set to a lower discharge voltage by the DC-DC converter, which would increase the fuel stack power during hover. The smaller battery can then be charged at a lower current during cruise, which would reduce the fuel stack power during cruise, and thus reduce the design power of the fuel stack. The lower capacity battery and lower power fuel stack would both lead to reductions in the powerplant weight.

Analytically, the fuel stack and battery design power, P_{fs} and P_{bat} respectively, can be found for some hover power P_{hi}, cruise power P_{lo}, hover time t_{hi}, and cruise time t_{lo} by solving the two equations below. E_{bat} is the total energy of the battery.

$$P_{hi} = P_{fs} + P_{bat} \tag{5.1}$$

$$(P_{fs} - P_{bat})t_{lo} = P_{bat}t_{hi}/2 = E_{bat} \tag{5.2}$$

Resizing the powerplant is beyond the scope of this research, as it would require purchasing a new, custom made fuel stack. Instead, an ideal power profile can be found for the existing powerplant. This power profile was used to demonstrate ideal power sharing, with data shown in Fig. 5.13. The circuit used is the same as that shown previously in Fig. 5.11. The new data now match the ideal power sharing seen in Fig. 5.5. This validates the ability of this circuit to achieve ideal power sharing, where: (1) the fuel stack operates at a constant power, (2) the battery supplements during high load portions of the mission, (3) a designer-defined constant ratio of battery and fuel stack power sharing is maintained, and (4) the fuel stack is used to

charge the battery during low load portions (indicated by fuel stack power higher than load power and negative battery power). This minimizes the design power of the fuel stack and the design energy of the battery, both of which are principal driving factors for weight. Thus, to summarize, the hybridization concept to be used in the eVTOL Sizing chapter is demonstrated to be possible.

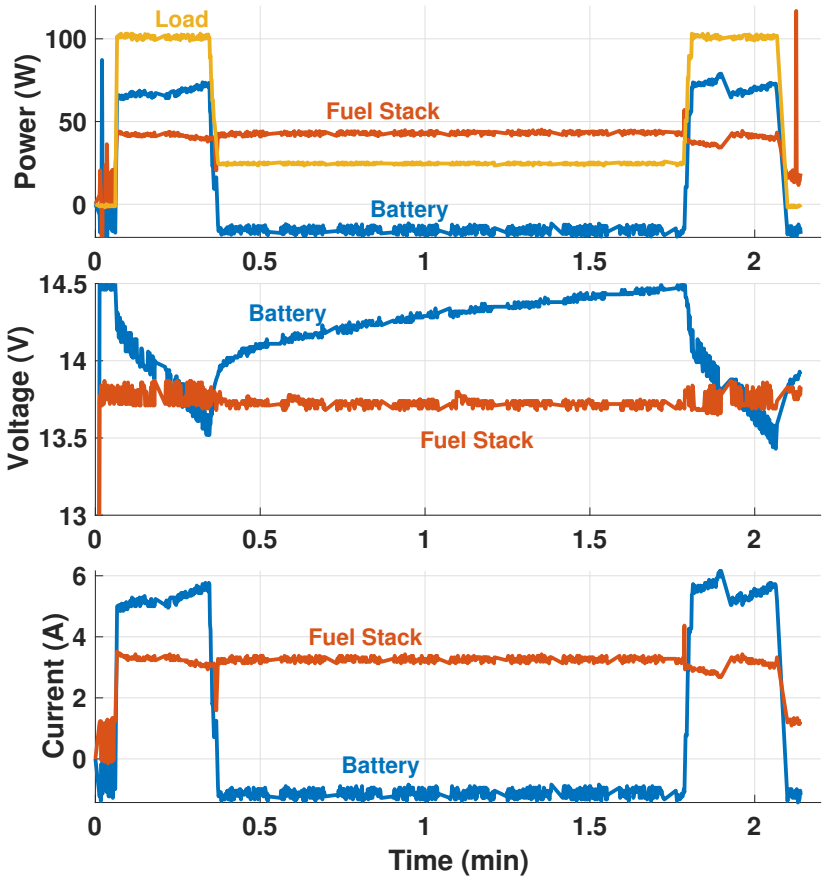

Figure 5.13: Measured power, voltage, and current of battery and fuel stack in regulated parallel configuration for an ideal power profile for the powerplant used in this research.

The overhead incurred in weight and power are minimal compared to the benefits of hybridization. Each of two DC-DC converters in the architecture portion of the setup causes an efficiency loss of around 90%. (The DC-DC step down

immediately after the fuel stack has a lower efficiency of 80%, as described in the Experimental Setup chapter.) Figure 5.14 shows a measurement of efficiency ($(P_{in} - P_{out})/P_{in}$) as a function of output current, for the DC-DC converters used in the power sharing architecture. The mass of the two DC-DC converters is 41 g each. These mass and power factors associated with the power sharing architecture are not included in the results in the eVTOL Sizing chapter.

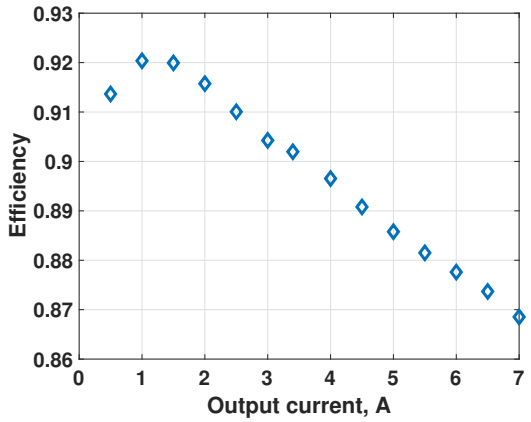

Figure 5.14: DC-DC converter efficiency as a function of output current.

5.3 Hardware

The key components used for this regulated architecture are shown in Fig. 5.15–5.18. The buck/boost converter was chosen for its ability deliver a constant current or constant voltage as desired, and automatically switch between stepping the input voltage up or down as needed to achieve the desired effect. It is set by hand using two potentiometers. The hall current sensors were selected because they measure current in both directions, with a positive or negative reading to indicate direction. They output a voltage signal between 0-5 V, which is then measured and

converted to a digital reading by the Arduino. The blocking diode was selected over other diodes due it its ability to withstand high currents and voltages. The solid state relay was chosen over other switching mechanisms due to its reliability and ease of use and compatibility with a 5 V Arduino signal.

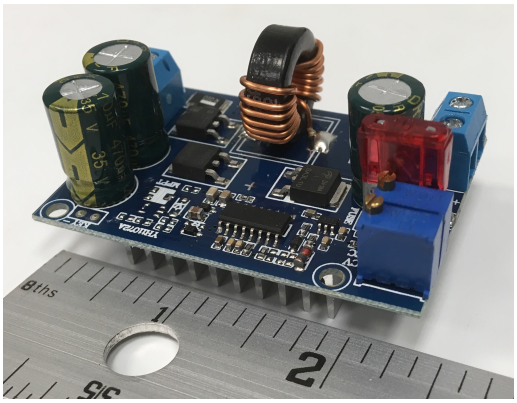

Figure 5.15: Buck/Boost Converter - 5-32 V to 1.25-20 V DC converter, 60 W power rating, by DROK.

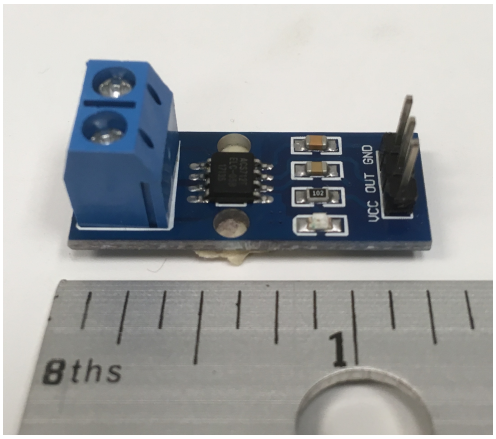

Figure 5.16: Current sensor - 30 A measurement range, 5 V working voltage, ACS712 chip Hall sensor module, by SMAKN.

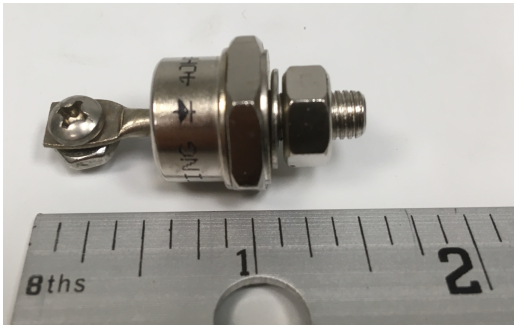

Figure 5.17: Blocking diode - NTE5991 Silicon Power Rectifier Diode, 40 Amp Current Rating, 400 V, by NTE Electronics.

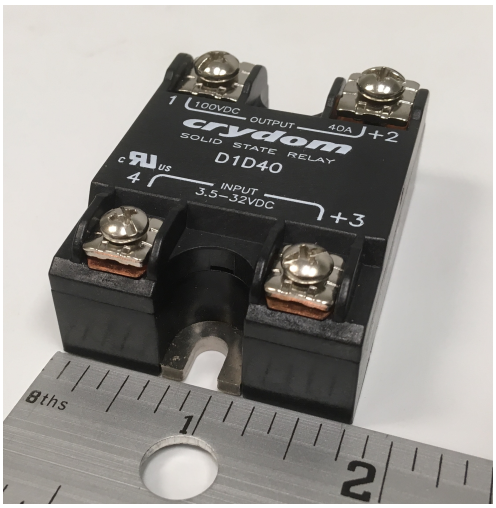

Figure 5.18: Relay - D1D40 solid state relay, 3.5-32 VDC input, 0-100 V load voltage, 40 A load current, by Sensata-Crydom.

Chapter 6: Powerplant Weight

This section describes models to calculate fuel cell and battery system weights required for aircraft sizing. These weights depend on the operating characteristics (models of which were described earlier) desired from the powerplant. Also described are motor weights.

6.1 Motors

Several manufacturers have introduced AC permanent magnet synchronous motors for powering aircraft in the past few years. Figures 6.1–6.2 show weights of 23 motors from six manufacturers (Thin Gap, Joby, EMRAX, YASA, Siemens and UQM), plotted versus maximum continuous torque and power. Of these, 17 motors are designed for aeronautical applications. The motors range from 4–260 kW continuous power, 3–1000 Nm continuous torque, and 1.3–95 kg weight. The inverter/controller weight lies between 16–28 kg for the heavier UQM motors. The operating voltage is typically between 250–425 volt DC.

Several weight trends can be found in recent literature [13, 17, 49]. In this paper, only the 17 aeronautical motors are used. Figure 6.1 shows how the weights of these motors scale with maximum continuous torque. Figure 6.2 shows how

they scale with maximum continuous power. The following equations (Eq. 6.1) can be used. The average error is around ±30%, similar to the models in the above literature. Either can be used in aircraft sizing; the torque equation is used here for its lower error at higher torques, and also because in principle, motor weight should scale nominally with torque.

$$\begin{aligned} \ln W_{kg} &= -0.91 + 0.71 \ln Q_{Nm} \\ W_{kg} &= 0.4025\ Q_{Nm}^{0.71} \qquad \text{with} \pm 30\% \text{ error} \\ \ln W_{kg} &= -0.89 + 0.89 \ln P_{kW} \\ W_{kg} &= 0.4106\ P_{kW}^{0.89} \qquad \text{with} \pm 30\% \text{ error} \end{aligned} \tag{6.1}$$

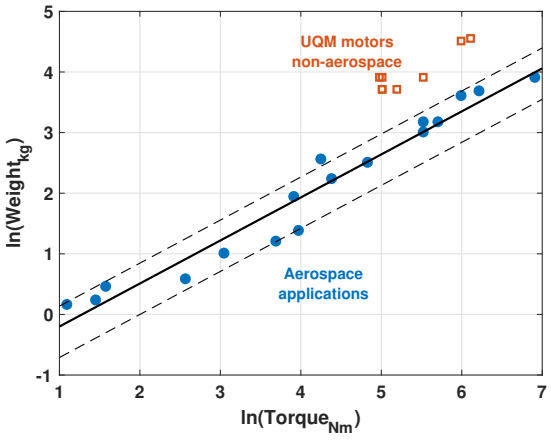

Figure 6.1: Natural logarithm of motor weight versus continuous torque with ±30% error bands.

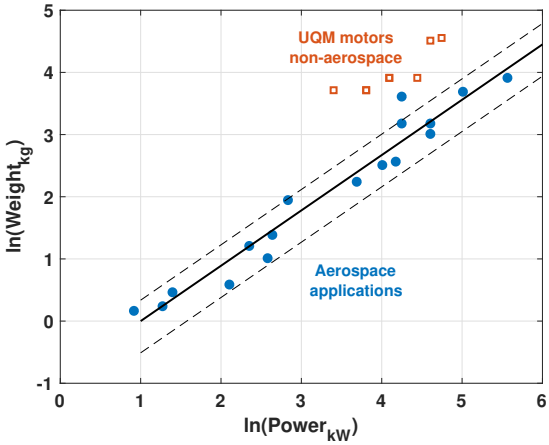

Figure 6.2: Natural logarithm of motor weight versus continuous power with ±30% error bands.

6.2 Lithium-Ion Batteries

Elementary Model

The most elementary model is not used in the sizing methodology for this work, but documented here for completeness. This model is simply the available ($\tilde{}70-80\%$ of the installed) specific energy E (Wh/kg) and maximum specific power P (W/kg) with which it can be delivered safely. The ratio P/E is called the C-rating, ζ (hr^{-1}). The ratio $P/E = (IV)/(CV)$, where I is current in amperes, V is voltage in volts, and C is charge capacity in Ah. So the C-rating ζ is the current delivered as a fraction of capacity. The maximum C-rating is the maximum current that can be delivered as a fraction of capacity without damaging the cell. This is fundamentally related to the maximum current density allowed by the electrode in A/m^2. Hence, for the same size (m^2), the same current can be drawn. So cells of lower capacity will show a higher current as a fraction of capacity. This is the reason small cells have very high C-ratings (30-40C). The weight of a cell scales with its capacity. The C-rating ζ is the current delivered as a fraction of capacity I/C also equal to $1/T$ where T is the time over which capacity C is discharged ($C = IT$). Thus, a 33 Ah (0.3C) rating means that a capacity C of 33 Ah can be delivered at maximum current $I = 0.3 \times 33A$, where $\zeta = 0.3$, over time $T = 1/\zeta = 1/0.3$ hr. A rating of 33 Ah (0.3C) / 5C maximum over 20 seconds, for example, would mean all of the above, but also a maximum current $I = 5 \times 33A$, where $\zeta = 5$, can be drawn — not for 1/5 hours continuously, but for a limited 20 seconds.

Refined Model

A refined model, beyond the elementary model above, would give the arrangement of cells to deliver a certain voltage, in addition to the energy, and associate battery weight with cell capacity. Such a model is more useful for sizing, and is more easily extended to advanced technology batteries of the future; only the cell weight equation (Eq. 6.2), cell voltage v_c (Eq. 6.4), and technology factor f_T (Eq. 6.4) need to change for new types of cell chemistries. The lithium-ion (Li-ion) battery model assumes n_s units in series arranged in n_p cells in parallel (Fig. 6.3). The total number of cells is $n_p \times n_s$. The series-parallel arrangement allows for adding energy while keeping a desired voltage output. The cells are assumed to be identical. The battery voltage is $V_B = n_s\ v_c$. The current through each cell is i_c. The currents add, so the battery current $I_B = n_p\ i_c$, or equivalently the battery capacity C_B (Ampere-hour, Ah) is related to the cell capacity C_c as $C_B = n_p\ C_c$. The energy capacity E_B (Watt-hour, Wh) is then $E_B = C_B\ V_B = n_p n_s\ C_c\, v_c = n_p n_s E_c$ which is the total number of cells in the battery times the energy capacity of each cell. The battery weight is calculated from the weight of each cell.

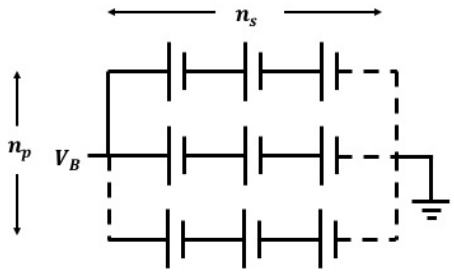

Figure 6.3: Schematic of batteries or fuel cells connected in series and parallel.

For a known output voltage V_B, mission energy E_B, and a choice of cell ca-

pacity C_c, the minimum weight is calculated as follows. The main equation is the cell weight versus capacity based on statistical fit of current generation Li-ion cells. The data in Fig. 6.4 are from twelve manufacturers; however, the equation uses data from only eight that are specifically designed for electric cars (shown as filled symbols in Fig. 6.4): AESC (NISSAN Leaf), LG Chem (Renault), Li-Tec (Daimler), Li Energy (Mitsubishi), Toshiba (Honda) and Panasonic (Tesla Model S). The weights follow the trend,

$$w_c = (0.0075 + 0.024\, Ah_c) \tag{6.2}$$

where w_c is in kg and C_c is in Ah. So the battery mass can be calculated as,

$$\begin{aligned}
&n_s = {}^{V_B}/_{v_c} && (v_c = 3.7 \text{ volt for Li ion}) \\
&C_B = {}^{P_B}/_{V_B\,\zeta} \quad \text{or} \quad E_B/v_B, && (\text{whichever is greater}) \\
&n_p = {}^{C_B}/_{C_c} && \\
&w_c = (0.0075 + 0.024\, C_c)\ f_T && (\text{kg}) \\
&W_B = w_c\ n_p\, n_s && (\text{kg})
\end{aligned} \tag{6.3}$$

P_B (Watt) is the power and ζ (hr^{-1}) is the C-rating. P_B/V_B is the current draw I_B. The minimum battery weight is found when I_B is the maximum (continuous, for the duration of P_B) discharge current. Then, $I_B = \zeta C_B$. If the C-rate ζ is known, the required charge capacity C_B can be found.

Consider a segment of a mission where power P_B is required over time Δt. If the voltage is V_B, then the charge capacity needed for this segment will be $\Delta C_B = P_B \Delta t / V_B$. However, if the C-rate is ζ, the power delivered can at most be $\zeta \Delta C_B V_B$. To ensure this equals P_B, the charge capacity must at least be $\Delta C_B = P_B / \zeta V_B$. Thus,

$$\Delta C_B = \max \left(\frac{P_B \Delta t}{V_B}, \quad \frac{P_B}{\zeta V_B} \right) \tag{6.4}$$

where the first quantity is the capacity required to deliver the energy required, and the second is the capacity required to deliver the power required. If the second is greater, it means more energy is needed for the mission than necessary just to satisfy the power demand. The optimal condition is when both are the same.

$$\zeta = 1/\Delta t \tag{6.5}$$

For example, if high power is required only for 5 min (e.g. for hover), then $\zeta = 60/5 = 12$ hr^{-1}. If a battery of this C-rate (12 C) is not available, then more capacity must be carried on board than what is needed to deliver the energy. Typically, Li-ion chemistries that store high energy have low C-rates and vice-versa (2-4 C for 80-100 Wh/kg; 0-1 C 150-200 Wh/kg at the battery pack level), thus the total capacity must be evaluated carefully based on power segments and available C-rates.

In general, for constant power, $P_B \, / \, \zeta$ gives the energy in Watt-hr. For varying

power, the energy is input from the mission, and the ζ found from the maximum power required. n_s and n_p are rounded to higher integers. The factor f_T is a technology factor; $f_T = 1$ places the specific energy at 150 Wh/kg for $\zeta = 1$ which represents a nominal state of the art at the battery pack level. The state of the art in cell level energy and power of these Li-ion batteries are shown in Fig. 6.5. The cells used for the weight equation can be found along the 1 hour endurance line (except for the NISSAN Leaf which falls near the 2 hour endurance line). The energy is obtained assuming up to 80% discharge and the power is based on the maximum continuous C-rating. Some of these cells are designed for higher power (greater maximum continuous current, i.e. C-rating) and some for higher energy, but it is apparent that in general they are energy limited, and only able to provide high specific power for short duration (less than 15 minutes). Figure 6.6 shows specific power and specific energy for two hobby grade batteries tested in house. The 4-cell battery shows the capability to exceed 5 C while maintaining a specific energy of 125 Wh/kg. The battery is rated to 85 C, but was not tested at C-rates above what is shown.

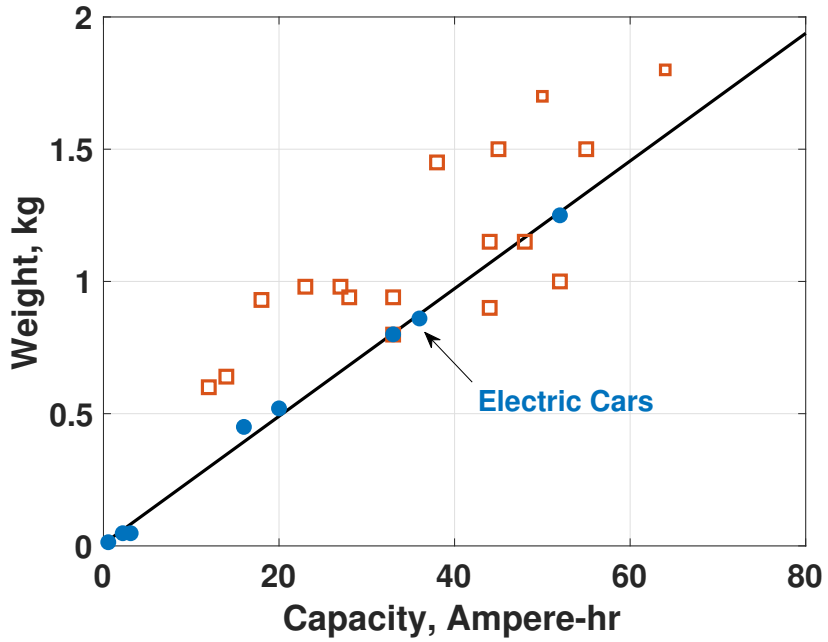

Figure 6.4: Li-ion cell weights versus capacity in Ampere-hr.

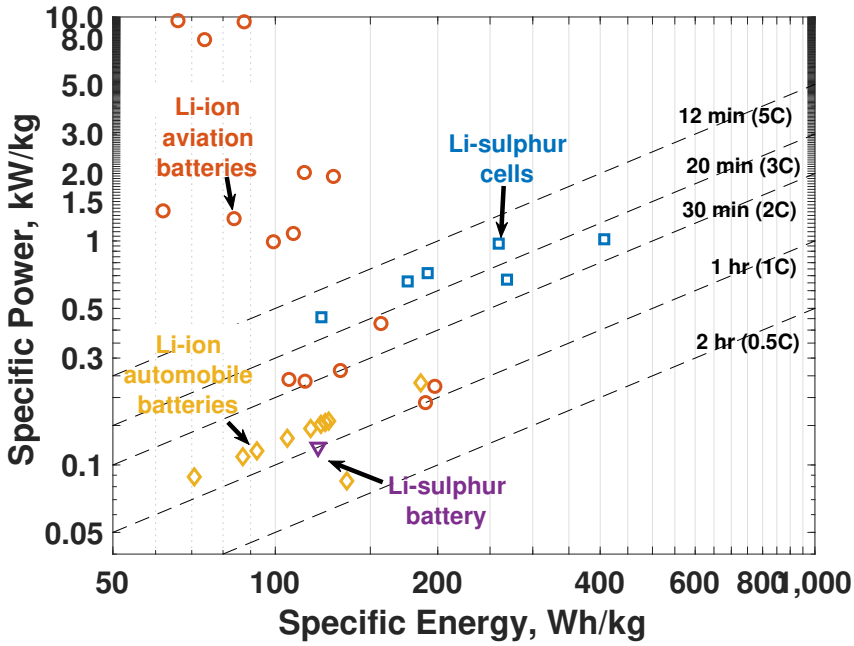

Figure 6.5: Li-ion and Li-sulfur cell specific power and energy (up to 80% discharge).

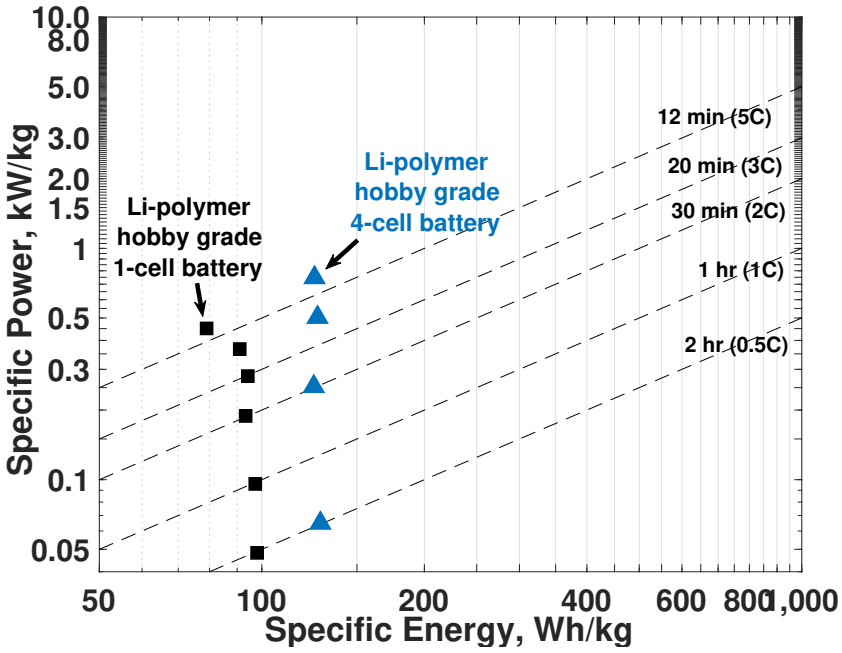

Figure 6.6: Li-polymer batteries analyzed in-house (full discharge).

6.3 PEM Fuel Stack

Proton Exchange (or Electrolyte) Membrane (PEM) fuel cells have lower specific power compared to batteries (due to a heavy balance of plant) but can provide dramatic increase in energy stored due to its hydrogen fuel. The degradation of its performance with low pressure is a problem in aeronautics, but not for on-demand air-taxi eVTOL, where the flight altitudes are expected be remain low. The problem of hydrogen storage and boil-off is also less significant in aviation compared to cars, and lesser even for on-demand air-taxi eVTOL, because of the shorter duration missions and only a few hours of hydrogen storage (not weeks or months). Thus the significant progress made in the past decade toward lighter gaseous hydrogen storage can be exploited to greater advantage, with some boil-off allowed.

A PEM fuel cell system consists of the stack and the hydrogen tank. For the stack, statistical weight models are difficult (see Fig. 6.7 for stacks of $0.4 - 100$ kW of continuous net power), because of drastic variations based on cost (cell materials and catalysts), duty cycles (construction), and applications (household, cars, aircraft auxiliary propulsion units (APU), and unmanned aerial vehicles (UAV)). Specific powers can easily range from 0.1 kW/kg for inexpensive laboratory grade stacks to 2.0 kW/kg for expensive automobile stacks.

A model suitable for design is one that is connected to stack geometry, materials, and operating characteristics so that improvements in constituent parts can flow into sizing. A simple model can be constructed as follows. Cells are assumed to be in series within a stack (which they typically are), similar to the arrangement

of battery cells to meet voltage and current requirements, shown in Fig. 6.3. Each cell is essentially a membrane electrode assembly (MEA). If the cross sectional area is k_A times the active area A_c, the area density of each MEA ρ_c (kg/m^2), thickness t_c (m), n_p cells in a stack, and an overhead fraction of η_O (to account for gaskets, seals, connectors and end plates), then the weight W_{FS} and volume L_{FS} become,

$$W_{FS} = \frac{k_A\, n_p\, A_c\, \rho_c}{1 - \eta_{OW}}$$
$$L_{FS} = \frac{k_A\, n_p\, A_c\, t_c}{1 - \eta_{OL}}$$

The maximum power output P_{max} is related to the maximum cell power density p_{cmax} by $P_{max} = p_{cmax}\, n_p\, A_c$. This can be rearranged, $n_p A_c = P_{max}/p_{cmax}$. The fuel stack operation accessories contribute to a balance of plant power, so a factor f_{BOP} is added to increase the required maximum power output. Then the weight model is,

$$W_{FS} = \frac{k_A\ \rho_c}{1 - \eta_{OW}}\ \frac{P_{max}(1 + f_{BOP})}{p_{cmax}} \tag{6.6}$$

A value of $k_A = 4$ (conservative) is assumed in this paper. Published data from Honda [26] and Toyota [27, 28] suggest $\rho_c = 1.57$ kg/m^2, $t_c = 0.001301$ m and $\eta_{OW} = 0.3$. The number of cells and active area are found from output voltage and power as: $n_p = V/\upsilon_c$ and $A_c = P/(n_p\ p_c)$. The design cell voltage υ_c (for maximum continuous power) is selected either to minimize the combined stack and tank weight or to ensure enough power margin (adequate maximum rated power). The factor

f_{BOP} is 20%, found in the Experimental Setup chapter, and is a conservative value, as it applies to a low-end fuel stack and DC-DC step down.

The fuel flow rate, at any given power, is related to the cell voltage. Corresponding to p_{cmax}, a υ_{cmax} can be found from the cell $i-\upsilon$ characteristics. In general, at any power P, cell power density is $p = P/n_p\,A_c$ and given p, the corresponding υ can be found. The fuel flow rate is

$$\dot{W}_F = \lambda_H\ \frac{m_H}{N_e\ F}\ \frac{P(1+f_{BOP})}{\upsilon} \tag{6.7}$$

and tank weight

$$W_{H2T} = \frac{1}{\eta_{BO}\ w_{frac}} \int \dot{W}_F\, dt \tag{6.8}$$

where λ_H is the effective stoichiometry (1 for no loss in hydrogen utilization), $m_H = 2.016 \times 10^{-3}$ kg/mol is the molar mass, $N_e = 2$ is the number of electrons released by each hydrogen atom, $F = 96485$ Coulomb/mol is Faraday's constant, P is the stack output power in Watt, υ the operating cell voltage in volts, and η_{BO} is the boil-off efficiency factor. The effective stoichiometry $\lambda_H = S_H\ \eta_H$, where S_H is the chemical stoichiometry (number of hydrogen molecules participating in reaction = 1) and η_H is the hydrogen utilization factor (typically $1 - 1.02$). The tank weight W_{H2T} is found from fuel weight W_F divided by the tank weight fraction w_f. For compressed hydrogen at 350 or 700 bar, the state of the art for long duration storage is 5.5% ($w_f = 0.055$) (see Fig. 6.8). Tolerating some hydrogen boil-off should allow

greater weight fractions of 7.5% – 15% (for example, the UTC helicopter used 10%), or perhaps even 30%. The tank model is simply this weight fraction.

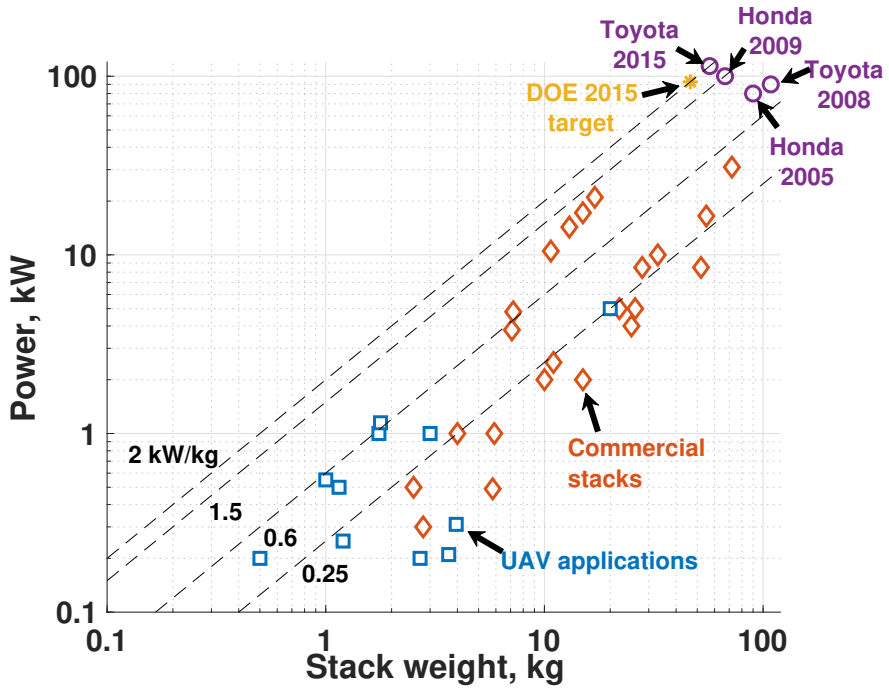

Figure 6.7: PEM stacks of power 0-100 kW.

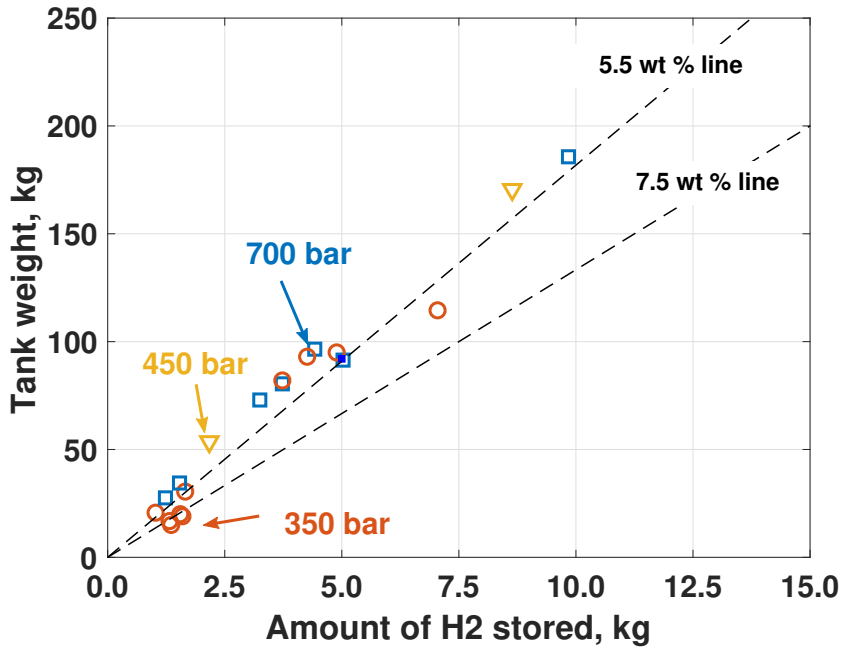

Figure 6.8: Gaseous (300, 450 and 700 bar) and liquid hydrogen storage.

Chapter 7: eVTOL Sizing

Sizing involves calculating the minimum gross (total) take-off weight (W_{GTO}, lb) and maximum engine power (for hover out of ground effect, P_H, hp) needed to carry a prescribed payload (W_{PAY}, lb) over a prescribed mission. The major dimensions of the configuration — rotor(s) radius and solidity and wing(s) span and chord — fall out of sizing. If the maximum power is prescribed as an input, sizing involves calculating the maximum gross take-off weight and payload.

An elementary mission is considered, representative of a simple on-demand intra-city air-taxi operation (Fig. 7.10): only 5 minutes of hover (including reserves) and 75 miles of cruise range. The vehicle is sized for different powerplants: turboshaft, battery only, fuel cell only, and battery-fuel cell (B-FC) hybrid. Battery charging from the fuel cell during flight is not considered.

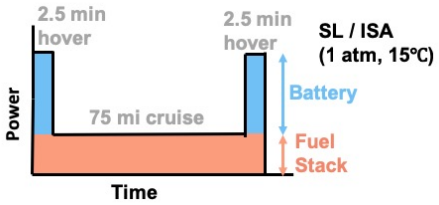

Figure 7.1: Baseline power profile used in eVTOL Sizing Section, showing B-FC hybrid power sharing scheme.

The Uber Elevate paper [5] suggests a maximum hover power P_H of 500 kW

(670 hp). This value is considered here. Three mission ranges are considered: a 75 mi baseline, a 150 mi extended range inter-city mission, and a shorter 50 mi intra-city mission. A total of 5 min of hover is included in each mission. Other attributes like cruise speed and gross weights influence the configuration, but are outputs of the sizing process.

7.1 Sizing Methodology

The maximum power is prescribed as an input. Sizing calculates the maximum gross take-off weight W_{GTO} and payload W_{PAY} for a range of disk loading $DL = W_{GTO}/A$, where A is the total projected disk area of all lifting rotors.

The weight break-downs are shown in Eq. 7.1 below. The gross take-off weight is the sum of empty weight and the useful weight. The empty weight W_E is the structural weight W_S, the power-plant weight W_P, and a generic group of all other weights W_{Oth}. This group of all other weights refers to the weights of systems and equipment, including: electrical (on-board power supply, anti-icing), avionics, furnishings (seats, emergency equipment), and load and handling (vibration absorbers, contingency weights). In the absence of any available data, historical trends of helicopters are used (typically 30% of empty weight; $f_{WO} = W_{Oth}/W_E = 0.3$) [51]. The useful weight is the payload weight and fuel weight. The payload weight includes fixed useful weights, such as the pilot and crew, and any additional payload.

$$
\begin{aligned}
W_{GTO} &= W_E + W_{USE} \\
W_E &= W_S + W_P + W_{Oth} \\
W_{USE} &= W_{PAY} + W_{FUEL}
\end{aligned}
\tag{7.1}
$$

For each disk loading, iterate the following steps until W_{GTO} converges:

1. From the maximum engine power, calculate the maximum W_{GTO}. Typically $P_{MAX} = PF\ P_H$, where PF is an installed power factor for excess power and P_H is from Eq. 7.2. Here, assume $PF = 1$ for minimal hover capability.

$$
P_{MAX} = P_H = \frac{1}{FM}\ W_{GTO}\ \sqrt{\frac{DL}{2\,\rho}} \tag{7.2}
$$

where ρ is density and FM is Figure of Merit (ideal induced power in hover divided by actual power), initialized as 0.6.

2. From disk loading and number of rotors N_R, find radius R of each rotor. With R known, FM can be updated. Here, blade element theory is used, with uniform inflow, induced power factor $K_h = 0.07$, and XV-15 airfoil decks. The following are assumed: solidity $\sigma = 0.1$, hover tip Mach number $M_T = 0.55$, number of blades per rotor $N_b = 3$, and and ISA/SL conditions (for density ρ and speed of sound c).

3. Calculate the power to cruise at speed V_C using Eq. 7.3.

$$P_C = \frac{W\, V_C}{L/D} \tag{7.3}$$

The aircraft weight W varies due to fuel burn (except for batteries) but the simple expression with $W = W_{GTO}$ is appropriate for an initial estimate. The lift to drag ratio L/D is a function of cruise speed V_C and this is where the configuration enters sizing.

The variation of L/D for a single edgewise rotor helicopter can be calculated using standard blade element momentum theory (with appropriate corrections). The aircraft drag area (ft^2) is estimated to be the minimum achieved by current helicopters (based on S-76, SA-341 and OH-6A helicopters as proposed by Harris [51])

$$F = f_D \left(\frac{W_{GTO}}{1000}\right)^{2/3} \tag{7.4}$$

where W_{GTO} is in lb and $f_D = 2.5$ for edgewise rotor helicopters.

The variation of L/D for a tiltrotor aircraft requires more detailed analysis because of lift sharing between a wing and rotor(s) as well as a reduction of rotor speed in cruise, which affects aircraft pitch and rotor collective. A two-dimensional trim solution was developed, which balances forces in the horizontal x and vertical z directions. The forces are: aircraft weight, aircraft drag, rotor lift, rotor propulsive force, wing lift, and wing drag. At a fixed

pylon angle, the trim variables are the aircraft pitch θ_{ac} and the rotor collective θ_{75}. The process for obtaining the trim solution will be described in detail in the next section, but introduced here.

This analysis results in L/D as a function of airspeed at a specific disk loading. For all disk loadings, the aircraft is assumed to be completely wing-bourne at 150 mph with a wing loading of 78 lb/ft^2 (XV-15 values). The wing aspect ratio $AR = 6$ with and Oswald efficiency factor $e = 0.8$. The wing airfoil is the VR-7, because the XV-15 wing airfoil is not available in the public domain. Component drags are scaled to gross take-off weight based on XV-15 values given in Ref. [50].

The cruise speed for minimum P_C/V_C, which by definition is the speed for best range V_{BR} (minimum energy spent per distance traveled), occurs at maximum L/D (Eq. 7.3). This speed is used for calculating cruise power. L/D versus DL for the final aircraft obtained in this process is shown in Fig. 7.2.

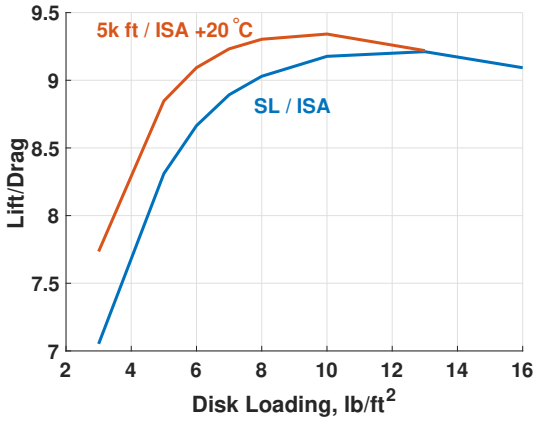

Figure 7.2: Maximum lift to drag ratio versus disk loading for final aircraft designed for 75 mile range; at cruise tip Mach number 0.28.

4. Calculate structural weight from statistical trends: $W_S = 0.24\,W_{GTO}$ (state of the art for helicopters [51]), valid between 3,000–100,000 lb gross take-off weight rotorcraft. eVTOL aircraft are not guaranteed to follow this trend, but it can be considered a reasonable target.

5. Calculate powerplant weight from weight models given in the previous section. The powerplant for the battery and fuel cell is the electric motor. The turboshaft model is the current statistical trend, which is valid between 300–20,000 engine hp. $P_{H,hp}$ is the hover power in hp. Any inefficiency due to electrical-to-mechanical conversion is neglected.

$$\begin{aligned} \text{turboshaft: } & W_P = 1.8\,P_{H,hp}^{0.9} \\ \text{battery: } & W_P = W_{motor} \\ \text{fuel cell: } & W_P = W_{motor} \end{aligned} \tag{7.5}$$

Calculate fuel weight from total energy required for the mission.

$$\begin{aligned} \text{turboshaft: } & W_{FUEL} = SFC\ E_{hp-hr} \\ \text{battery: } & W_{FUEL} = W_B \\ \text{fuel cell: } & W_{FUEL} = W_{H2T} + W_{FuelStack}(1 + f_{OH}) \end{aligned} \tag{7.6}$$

For the turboshaft, E_{hp-hr} is the mission energy in hp-hr, and a SFC of

0.4 lb / hp-hr is assumed. For the fuel cell, f_{OH} is the 15% weight overhead associated with the fuel stack used in the experimental setup of this paper. Note that while the fuel stack is not an expendable fuel mass, it is categorized as fuel weight to provide a fair comparison with the battery.

6. Calculate empty weight: $W_E = (W_P + W_S)/(1 - f_{WO})$. The 'all other' group is estimated as $W_{Oth} = f_{WO}\, W_E$, as described at the beginning of this section. Typically this group constitutes up to 30% of W_E for modern aircraft, so $f_{WO} = 0.3$ [51].

7. Calculate useful load and payload,

$$W_{USE} = W_{GTO} - W_E$$

$$W_{PAY} = W_{USE} - W_{FUEL}$$

and iterate steps 1–7 until the weights have converged.

7.2 Aircraft Performance Analysis

Step 3 of the sizing methodology in the previous section includes a rigorous calculation of the lift to drag ratio, L/D. This section describes in detail how this result was obtained.

An analytical trim solution was developed to evaluate the performance of compound rotorcraft with one or more wings and tilting rotors. The result was

then used to determine L/D as a function of true airspeed. Figure 7.3 shows the analytical result using XV-15 parameters falling close to empirical data from XV-15 flight tests. This analytical prediction was obtained using XV-15 parameters wherever possible, and calibrated to the XV-15 data where parameters were not publicly available. The dashed lines corresponding to a reduced tip Mach number illustrate the potential of eVTOL: electric motors can operate efficiently at a wider range of rpm than conventional turboshaft engines, so they can maintain a higher tip speed for efficient hover while operating at lower tip speeds for efficient cruise.

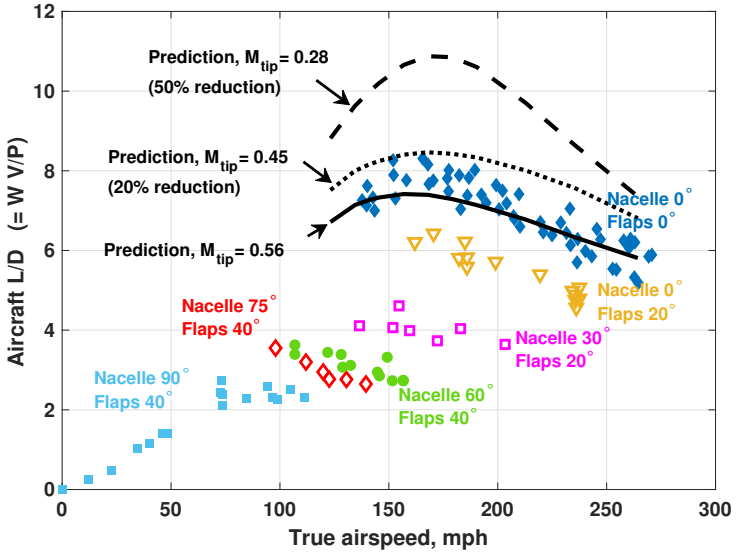

Figure 7.3: XV-15 lift to drag ratio as a function of true airspeed, analytical prediction validated against experimental data [50].

The trim solution balances forces in the horizontal x and vertical z directions. The forces are: aircraft weight, aircraft drag, rotor lift, rotor propulsive force, wing lift, and wing drag. The trim variables used here are the aircraft pitch θ_{ac} and the rotor collective θ_{75}. Alternatively, pylon angle θ_{py} could be used in place of θ_{ac}, and tip Mach number M_{tip} could be used in place of θ_{75}. For this analysis, θ_{py} is set to

obtain level flight at 270 mph, and M_{tip} is a performance parameter set by the user. The important angles used in this analysis are shown in Fig. 7.4.

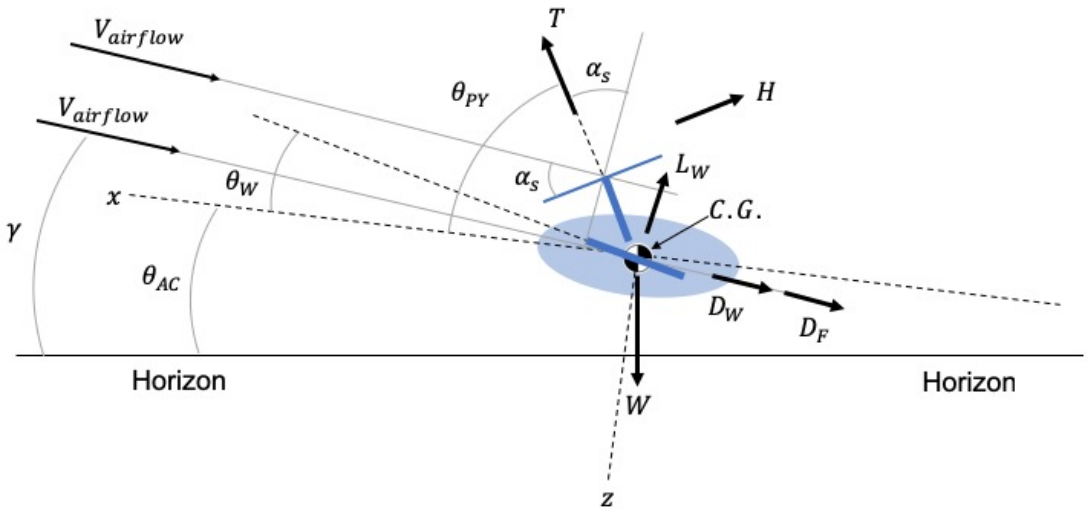

Figure 7.4: Key aircraft angles, including airframe, wing, and rotor.

Airframe Forces

The aircraft input parameters are gross take off weight W_{GTO}, number of rotors N_R, climb velocity V_c, and true airspeed or forward flight velocity V_f. The aircraft weight acts in the downward z direction. The aircraft drag is calculated for several components individually using,

$$F = f_D \left(\frac{W}{1000} \right)^{2/3} \tag{7.7}$$

$$D = q\ F \qquad \text{for } \alpha < \alpha_{stall} \tag{7.8}$$

$$= q\ F(1 + a\ \alpha^b) \qquad \text{for } \alpha \geq \alpha_{stall}$$

where q is defined as the dynamic pressure,

$$q = \frac{1}{2}\rho V_f^2 \tag{7.9}$$

Here, $a = 20$ and $b = 2$ are calibration constants, and $W = 13,000$ lb is the gross take-off weight in lbf for the XV-15. α is the angle of attack of each component and $\alpha_{stall} = 14$ deg is used as the stall angle. f_D is defined for each component by Johnson in Ref. [50] and listed here in Table 7.1. However, the fuselage factor found in Ref. [50] was allowed to vary as a calibration constant; this is to correct for inaccuracies in calculating wing drag using the VR7 airfoil instead of the XV-15 airfoil, which is not available in the public domain. Additionally, the horizontal tail factor found in Ref. [50] is set to 0 and calculated separately as part of wing drag.

Table 7.1: Drag factors for various aircraft components

Component	f_D	α
fuselage	~~$1.56/\left(\frac{13000}{1000}\right)^{2/3} = 0.2822$~~ 0.0534	aircraft angle of attack, α_{ac}
fittings and fixtures	$3.00/\left(\frac{13000}{1000}\right)^{2/3} = 0.5426$	aircraft angle of attack, α_{ac}
pylon	$0.76/\left(\frac{13000}{1000}\right)^{2/3} = 0.1375$	pylon angle of attack, α_{py}
vertical tail	$0.36/\left(\frac{13000}{1000}\right)^{2/3} = 0.0651$	aircraft sideslip, $\alpha_{side} = 0$
horizontal tail	calculated as part of wing drag	
wing	calculated separately	

Wing Forces

The wing input parameters for the XV-15 are aspect ratio $AR = 6.086$ and Oswald efficiency factor $e = 0.9$. The wing angle of attack is calculated as,

$$\alpha_w = \theta - \phi \tag{7.10}$$

$$\theta = \theta_{ac} + \theta_w - \gamma \tag{7.11}$$

$$\phi = \frac{c_L}{\pi AR\ e} \tag{7.12}$$

where θ_{ac} is the angle between the aircraft and the horizon, θ_w is the wing incidence angle, γ is the flight angle between the aircraft velocity vector and the horizon, and c_L is initialized to 1. α_w and Mach number M_w are used with a VR7 airfoil lookup table to find the coefficients of lift c_L, drag c_D, and moment c_M. Since the equation for ϕ contains c_L, fixed-point iteration is employed to obtain converged values for c_L, c_D, and c_M. Then, lift, drag, and moment are calculated,

$$L_w = qA_w c_L \tag{7.13}$$

$$D_w = qA_w c_D \tag{7.14}$$

$$M_w = qA_w c_M c_{w,mean} \tag{7.15}$$

where q is defined in Eq. 7.9. $A_w = 15.6$ m^2 is the wing area, and $c_{w,mean} = 1.6$ m is the mean wing chord, corresponding to the XV-15 geometry.

The horizontal tail is treated as an additional wing in the calculations. Equations 7.11–7.15 are repeated with XV-15 values, $A_h = 4.67$ m, $c_{h,mean} = 0.843$ m, $AR_h = 0.560$, $e_h = 0.9$ to obtain L_h, D_h, and M_h.

Rotor Forces

The rotor forces are calculated using blade element momentum theory, integrated over azimuth. The rotor input parameters are disk loading DL, rotor disk area A, tip Mach number M_{tip}, root cutout r_{cut}, solidity σ, number of blades N_b, induced power factors κ_h and κ_f.

First, the advance ratio μ and nondimensionalized climb inflow λ_c are calculated as follows,

$$\alpha_s = \frac{\pi}{2} - \theta_{py} - \theta_{ac} + \gamma \tag{7.16}$$

$$\beta = 0 \tag{7.17}$$

$$V_x = V_f \cos(\alpha_s) \cos(\beta) \tag{7.18}$$

$$\mu = \frac{V_x}{\Omega R} \tag{7.19}$$

$$V_z = V_f \sin(\alpha_s) \cos(\beta) \tag{7.20}$$

$$\lambda_c = \frac{V_z}{\Omega R} \tag{7.21}$$

where α_s is angle of the velocity vector V_f relative to the hub plane. $\alpha_s = 0°$ for pure edgewise flight and $\alpha_s = 90°$ for pure climb or cruise (for a tiltrotor). $\beta = 0$ is the side slip angle. θ_{py} is the pitch of the pylon relative to the fuselage, θ_{ac} is the aircraft pitch relative to the horizon, and γ is the angle between the aircraft's

trajectory and the horizon.

The airflow velocity U at each rotor blade segment is evaluated. It is made up of the tangential velocity U_T and perpendicular velocity U_P, where $x = r/R$ is the blade radial location nondimensionalzed with radius and ψ is the angle in radians around the azimuth.

$$U_T = (x + \mu \sin|\psi|)\ \Omega R \tag{7.22}$$

$$U_P = \lambda \Omega R \tag{7.23}$$

$$U = \sqrt{U_T^2 + U_P^2} \tag{7.24}$$

The rotor blade element's coefficients of lift c_L, drag c_D, and moment c_M from an XV-15 airfoil lookup table based on the blade element angle of attack α_r and Mach number M_r,

$$\phi_r = \tan^{-1}\left(\frac{U_p}{U_t}\right) \tag{7.25}$$

$$\alpha_r = \theta_r - \phi_r \tag{7.26}$$

$$M_r = (x + \mu \sin(\psi))\ M_{tip} \tag{7.27}$$

where θ_r is the rotor pitch at the center of the blade segment. The differential

lift, drag, and moment for each segment is calculated as follows,

$$dL = \frac{1}{2}\rho U^2 c_L c \; dr \tag{7.28}$$

$$dD = \frac{1}{2}\rho U^2 c_D c \; dr \tag{7.29}$$

$$dM = \frac{1}{2}\rho U^2 c_M c^2 dr \tag{7.30}$$

where c is the local chord and dr is the width of the blade segment.

The forces and moments are resolved along the hub axes in the rotating frame: z is along the shaft in the direction of nominal thrust, x is along the blade in the direction of centrifugal force, and y is towards the leading edge of the blade,

$$df_x = 0 \tag{7.31}$$

$$df_y = -dL \sin\phi - dD \cos\phi \tag{7.32}$$

$$df_z = dL \cos\phi - dD \sin\phi \tag{7.33}$$

$$dm_x = dM \tag{7.34}$$

$$dm_y = -df_z r \tag{7.35}$$

$$dm_z = -df_y r \tag{7.36}$$

and integrated over span for root loads. Blade motion can be ignored for steady-state performance. The integrated root loads ($f_x,\ f_y,\ f_z,\ m_x,\ m_y,\ m_z$) are resolved along the hub axes in the fixed frame: Z is along the shaft, X is opposite

the direction of motion in the hub plane, and Y is towards the starboard side.

$$f_X = f_x \cos\psi - f_y \sin\psi \tag{7.37}$$

$$f_Y = f_x \sin\psi + f_y \cos\psi \tag{7.38}$$

$$f_Z = f_z \tag{7.39}$$

$$m_X = m_x \cos\psi - m_y \sin\psi \tag{7.40}$$

$$m_Y = m_x \sin\psi + m_y \cos\psi \tag{7.41}$$

$$m_Z = m_z \tag{7.42}$$

This is calculated for each segment along the rotor blade, and the forces and moments are integrated over the length of the blade. This is done at each azimuthal station and integrated over the rotor disk,

$$H = \frac{N_b}{n_{psi}} \sum_{n_{psi}} F_X \qquad c_H = \frac{H}{\rho A(\Omega R)^2} \tag{7.43}$$

$$Y = \frac{N_b}{n_{psi}} \sum_{n_{psi}} F_Y \qquad c_Y = \frac{Y}{\rho A(\Omega R)^2} \tag{7.44}$$

$$T = \frac{N_b}{n_{psi}} \sum_{n_{psi}} F_Z \qquad c_T = \frac{T}{\rho A(\Omega R)^2} \tag{7.45}$$

$$M_X = \frac{N_b}{n_{psi}} \sum_{n_{psi}} m_X \qquad c_{Mx} = \frac{M_X}{\rho A(\Omega R)^2 R} \tag{7.46}$$

$$M_Y = \frac{N_b}{n_{psi}} \sum_{n_{psi}} m_Y \qquad c_{My} = \frac{M_Y}{\rho A(\Omega R)^2 R} \tag{7.47}$$

$$Q = \frac{N_b}{n_{psi}} \sum_{n_{psi}} m_Z \qquad c_Q = \frac{Q}{\rho A(\Omega R)^2 R} \tag{7.48}$$

where n_{psi} is the number of azimuth segments, H is the hub drag, T is the vertical upward force, and Y is the horizontal lateral force.

The forces and moments in the wind axes give rotor lift L_r and propulsive force X_r,

$$L_r = T\cos\alpha_s + H\sin\alpha_s \tag{7.49}$$

$$X_r = T\sin\alpha_s - H\cos\alpha_s \tag{7.50}$$

where α_s is defined in Eq. 7.17. L_r is perpendicular to the velocity vector and X_r is parallel to the velocity vector. These are needed for the rotor L/D_e calculation.

Trim with All Forces

At this point, all the forces due to the fuselage, wing, and rotor have been calculated. For force balance, resolve the forces along the gravity frame and sum forces in the horizontal and vertical directions. If a horizontal tail is present, it is treated as an additional wing in the calculations.

$$\text{Fuselage :} \qquad F_{Z,f} = -D_f \sin\phi_f \tag{7.51}$$

$$F_{X,f} = -D_f \cos\phi_f \tag{7.52}$$

$$\phi_f = \gamma \tag{7.53}$$

$$\text{Wing :} \qquad F_{Z,w} = \quad L_w \cos\phi_w - D_w \sin\phi_w \tag{7.54}$$

$$F_{X,w} = -L_w \sin\phi_w - D_w \cos\phi_w \tag{7.55}$$

$$\phi_w = \phi_w \text{ defined in Eq. 7.12} \tag{7.56}$$

$$\text{Rotors :} \qquad F_{Z,r} = \quad N_{rotors} L_r \cos\phi_r + N_{rotors} X_r \sin\phi_r \tag{7.57}$$

$$F_{X,r} = -N_{rotors} L_r \sin\phi_r + N_{rotors} X_r \cos\phi_r \tag{7.58}$$

$$\phi_r = \gamma \tag{7.59}$$

$$\text{Force Summation :} \qquad \sum F_Z = F_{Z,r} + F_{Z,w} + F_{Z,f} - W = R_1 \tag{7.60}$$

$$\sum F_X = F_{X,r} + F_{X,w} + F_{X,f} \qquad = R_2 \tag{7.61}$$

Newton-Raphson iteration is performed to reduce the residuals R_1 and R_2 to zero. The converged solution outputs the trim variables θ_{75} and θ_{ac}. This is performed for a range of forward flight velocities and shown in Fig. 7.5 and 7.6. θ_{ac} is compared with experimental data from [50]. The biggest assumption here is the absence of moment and center of gravity balance. For the tiltrotor configuration

here, future work should at least include pitching moment balance. The yaw and roll moments cancel nominally due to the symmetry of two rotors. The pitching moment can be trimmed (canceled) at the hub by cyclic inputs, so the principal equations for performance are still the two force equilibrium equations shown here.

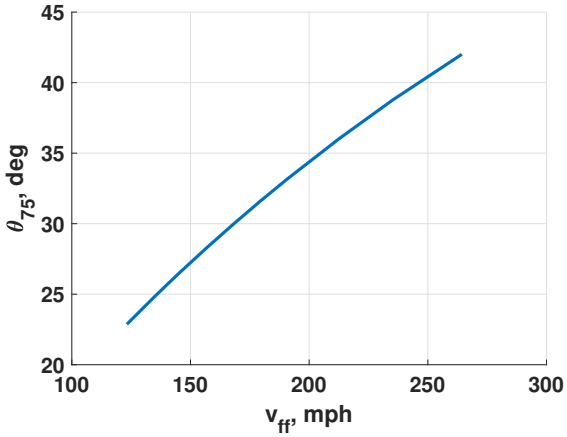

Figure 7.5: XV-15 trim solution; collective as a function of forward flight speed.

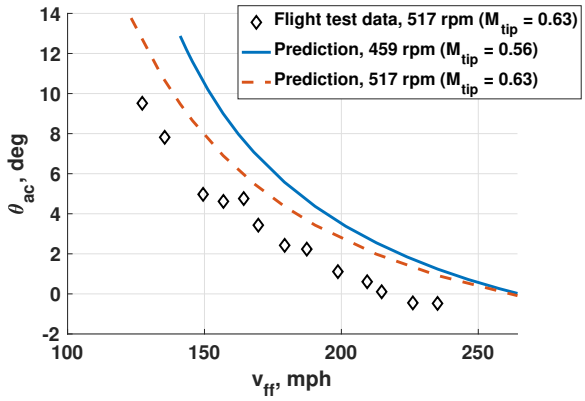

Figure 7.6: XV-15 trim solution; aircraft pitch as a function of forward flight speed.

The nondimensionalized forces and moments over solidity are shown as a function of forward flight velocity in Fig. 7.7 and 7.8. At maximum speed, the rotor is in axial flow, so only C_T/σ (i.e. thrust) remains. The aircraft is wing-borne at this speed. The C_T/σ values are much smaller compared to that of typical helicopters, but typical of tilting proprotors. Later, a reduction in tip Mach number, M_{tip}, will be shown to increase these values and make the rotor far more efficient.

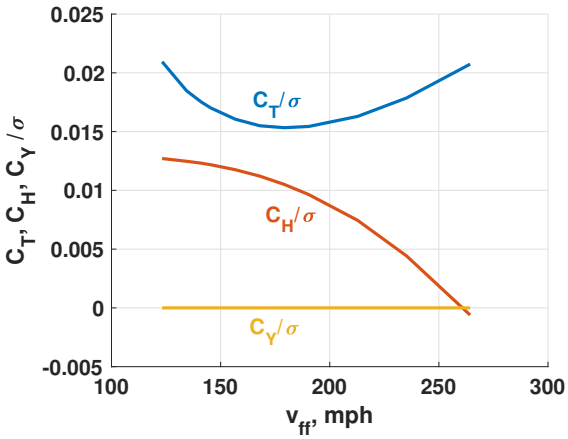

Figure 7.7: XV-15 trim solution; coefficients of force over solidity as a function of forward flight speed.

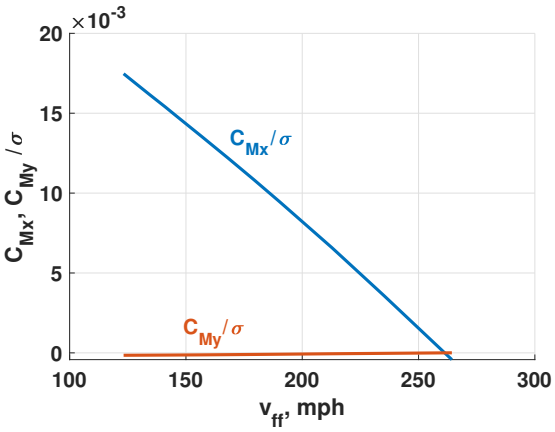

Figure 7.8: XV-15 trim solution; coefficients of moment over solidity as a function of forward flight speed.

In order to calculate the rotor performance (lift to drag ratio), the induced and profile power must calculated. First, the induced power is calculated for each blade segment at each azimuthal station, based on μ and λ_c defined in Eq. 7.20 and 7.21,

$$\lambda_h = \sqrt{|C_T|/2} \tag{7.62}$$

For $\mu = 0$,

$$\begin{aligned}
&\text{For } \frac{\lambda_c}{\lambda_h} > -1, && \lambda_{i0} = \lambda_h \left(-\frac{\lambda_c}{2\lambda_h} + \sqrt{\left(-\frac{\lambda_c}{2\lambda_h} \right)^2 + 1} \right) \\
&\text{For } -2 < \frac{\lambda_c}{\lambda_h} \leq -1, && \lambda_{i0} = \lambda_c \left(0.373 \left(\frac{\lambda_c}{\lambda_h} \right)^2 - 1.991 \right) \\
&\text{For } \frac{\lambda_c}{\lambda_h} \leq -2, && \lambda_{i0} = \lambda_h \left(-\frac{\lambda_c}{2\lambda_h} - \sqrt{\left(-\frac{\lambda_c}{2\lambda_h} \right)^2 + 1} \right)
\end{aligned} \tag{7.63}$$

$$\lambda_i = K_h \lambda_{i0} \tag{7.64}$$

$$\lambda = K_h \lambda_{i0} + \lambda_c \tag{7.65}$$

For $\mu \neq 0$,

Iterate until λ converges :

$$\lambda_0 = \lambda_h$$

$$Num = \mu \tan \alpha_s + |C_T| \frac{\mu^2 + \lambda_0^2}{\left(\mu^2 + \lambda_0^2\right)^{3/2}}$$

$$Den = 1 + |C_T| \frac{\lambda_0}{2\left(\mu^2 + \lambda_0^2\right)^{3/2}}$$

$$\lambda_0 = Num/Den \tag{7.66}$$

After convergence :

$$\lambda_i = \text{sign}(C_T) K_f (\lambda_0 - \mu \tan \alpha_s) \tag{7.67}$$

$$\lambda = \lambda_i + \mu \tan \alpha_s \tag{7.68}$$

$$dp_i = df_z \lambda_i \Omega R \tag{7.69}$$

$$p_i = \sum dp_i dr \tag{7.70}$$

$$P_i = \frac{N_b}{n_{psi}} \sum_{n_{psi}} p_i \tag{7.71}$$

Then, the rotor's propulsive and profile power are calculated as follows,

$$\text{Total power :} \quad C_P = C_Q \tag{7.72}$$

$$\text{Induced power :} \quad C_{Pi} = \frac{P_i}{\rho A(\Omega R)^3} \tag{7.73}$$

$$\text{Propulsive power :} \quad C_{Px} = C_X \frac{V_f}{\Omega R} \tag{7.74}$$

$$P_x = C_{Px} \rho A(\Omega R)^3 \tag{7.75}$$

$$\text{Profile power :} \quad C_{Po} = C_P - C_{Pi} - C_{Px} \tag{7.76}$$

$$P_o = C_{Po} \rho A(\Omega R)^3 \tag{7.77}$$

The power for propulsion is P_x, so the power for lifting action is $P - P_x$. This can be converted to an equivalent drag, $P - P_x = V_f \ D_e$. This drag is needed for rotor lift to drag ratio (i.e. lift to drag associated with lifting action), L/D_e,

$$\frac{L}{D_e} = \frac{L}{(P \ / V_f - P_x)} = \frac{L}{(P_i + P_o \ / V_f)} \tag{7.78}$$

For each rotor, $L = W/N_{rotor}$, so,

$$\frac{L}{D_e} = \frac{W/N_{rotors}}{(P_i + P_o) \ / V_f} = \frac{W/N_{rotors}}{(P - P_x) \ / V_f} \tag{7.79}$$

L/D_e is shown as a function of forward flight speed in Fig. 7.9.

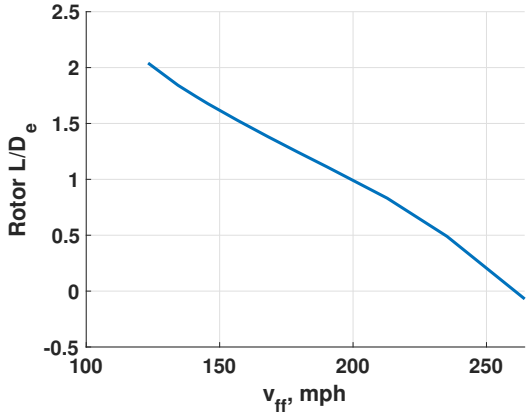

Figure 7.9: XV-15 trim solution; rotor lift to drag ratio as a function of forward flight speed.

Finally, the total aircraft lift to drag is calculated. Here, the total power is converted to drag,

$$\frac{L}{D} = \frac{L}{P/V_f} = \frac{LV_f}{P} = \frac{WV_f}{P} \tag{7.80}$$

The result was shown in Fig. 7.3. This analysis is used in Step (3) of the Sizing Methodology section.

7.3 Results of Sizing

The steps listed in the Sizing Methodology section were carried out for a notional mission of 5 minutes hover at 500 kW and 75 mi of cruise at the best range speed at SL/ISA, illustrated in Fig. 7.10. This is an elementary mission appropriate for a new powerplant so that key trends do not get buried inside the

details of start up, shut down, reserves, etc. Additional weight needed for reserves and redundancy in batteries or fuel stacks are not considered. The purpose is to evaluate and compare the different powerplants.

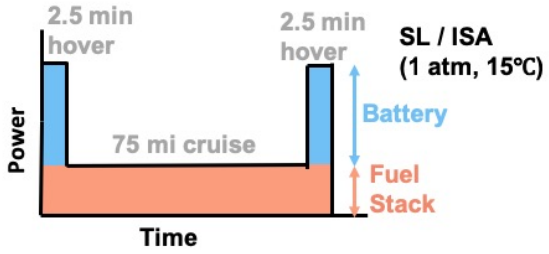

Figure 7.10: Baseline power profile used in eVTOL Sizing Section, showing B-FC hybrid power sharing scheme.

The cruise power for edgewise and tiltrotor configurations are shown in Fig. 7.11. For both the edgewise and tiltrotor configurations, the cruise speed is set to the best range speed V_{BR} at each disk loading. Tiltrotors require lower cruise power due to higher L/D. For the tiltrotor, the cruise power increases first, then drops with increasing DL; around 16 lb/ft^2, the cruise power is 240 hp. Edgewise rotors require significantly higher cruise power. At DL of 16, the cruise power is 430 hp. The minimum edgewise rotor cruise power occurs at 10 lb/ft^2 at 370 hp. The reduced cruise power has a dramatic impact on the feasibility of electric flight, so only the tiltrotor configuration is considered henceforth for the electric powerplants.

Figures 7.12– 7.18 show gross take-off weights and payload weights for a variety of conceptual power-plants. Figure 7.12 compares an edgewise rotor versus tilting proprotor configuration for two different powerplants – a conventional turboshaft engine and a battery-fuel cell (B-FC) hybrid powerplant. For the turboshaft engine, there is no significant difference in payload between the two configurations, because

75 mi is too short a cruise for the tiltrotor to produce the benefit of reduced fuel burn. The engine weight, scaled to maximum hover power, remains the major contributor to the power group. This however is not the case for electric power, where the battery weight is scaled to total energy and fuel cell weight to cruise power. The reduced cruise power has a dramatic impact on the feasibility of electric flight; only the tilting proprotor produces a positive payload, so only the tiltrotor configuration is considered henceforth for the electric powerplants.

Figure 7.13 shows the gross takeoff weights and payload weights for a turboshaft, fuel cell, battery, and B-FC hybrid powerplant. These sizing results are based on a two rotor tiltrotor configuration. They use conservative baseline technology for electric power components. This includes a battery available specific energy of 150 Wh/kg (Saft, Tesla), a fuel cell specific power of 0.5 kW/kg (Toyota), and a hydrogen storage weight fraction of 5.4% (Department of Energy). The battery powerplant assumes that the battery is energy limited rather than power limited, and is therefore sized according to its specific energy. The C-rate ζ is then a fallout. The hybrid powerplant includes a fuel stack sized to accommodate the prescribed cruise power, as well as a battery portion sized to accommodate the remaining energy for the mission. Charging the battery during the mission is not considered. The results show that for this mission, only the B-FC hybrid powerplant can carry a payload. For a gross take-off weight of 6200 lb, the payload weight is around 500 lb at a DL of 10 lb/ft^2. The weight break-downs for the B-FC hybrid powerplant at three different cruise ranges are shown in Table 7.2. The other cruise ranges are discussed in detail later. Fuel cells that provide 0.5 kW/kg specific power

still require custom design. The batteries consist of 68 units of 9 cells, each cell rated at (10 C) 100 Ah. These are high power cells and will also require custom design. Results are presented only for a two rotor tiltrotor; in a a multirotor aircraft, the advantage of the turboshaft would be slightly diminished, because each additional rotor requires an additional mechanical drivetrain for the turboshaft powerplant, comapred to a lighter electrical connection for electric powerplants.

Figure 7.14 shows the effects of an improvement in battery technology. It shows that with a battery of 250 Wh/kg available specific energy, a battery-only powerplant can accommodate a 1200 kg payload for a gross take-off weight of 6200 lb. Figure 7.15 shows the effects of improvements in fuel cell and hydrogen storage technology. A 7.5% weight fraction is a reasonable value to use for aviation, where boil-off is of lesser concern than in automobiles. Increasing the specific power of a fuel stack to Toyota's reported 2 kW/kg decreases the weight of the powerplant significantly, to the point where a fuel cell powerplant can accommodate a useful payload of around 1800 lb at a gross weight of 6600 b. Figure 7.16 combines these improvements in a B-FC hybrid powerplant to achieve a payload of 1800 lb with a gross take-off weight of 6200 lb, or a payload weight of 1900 lb for a gross take off weight of 6600 lb at a disk loading of 8 lb/ft^2. The greatest impact comes from increasing the fuel cell specific power to 2 kW/kg.

Figure 7.17 shows the effects of operating at increased altitude and temperature of 5,000 ft and 20° C. This corresponds to an air density decrease from 0.00238 slugs/ft^2 to 0.00194 slugs/ft^2 and a sound speed increase from 1116 ft/s to 1132 ft/s. As a result, the payload is reduced to 300 lb for a gross take-off weight of 6200 lb.

Thus far, the powerplants involving batteries have been sized using specific energy, under the assumption that specific power (or C-rate) is not a limiting factor. Figure 7.18 shows how the payload weight changes if the battery is in fact power limited. A battery's specific power is based on its C-rating, which specifies the maximum discharge current of the battery. The line for C-rating 10+ in Fig. 7.18 is the same as the line in Fig. 7.13 for hybrid W_{PAY}, in which power was not a limiting factor. The other lines in Fig. 7.18 show a decreasing payload weight because the powerplant weight is increased by a larger battery requirement to provide sufficient power for the mission. A B-FC hybrid powerplant using a 6C battery and baseline technology (150 Wh/kg battery, 0.5 kW/kg fuel cell, 5% w_f tank) is only capable of carrying a payload of 200 lb.

Productivity is a metric used classically to select the optimal disk loading. Productivity is defined as the useful work done per dollar. Useful work is $W_{PAY} \times V_c$ and cost scales closely with W_E. The expression for productivity is $W_{PAY} \times V_c / W_E$. Figure 7.19 shows the productivity of the hybrid powerplant for different C-ratings. Based on these results, the optimal eVTOL for this mission using baseline technology would have approximately: a C-rating of 10, disk loading of 10 lb/ft^2, W_{GTO} of 6200 lb, and a payload weight of 500 lb (based on Fig. 7.18).

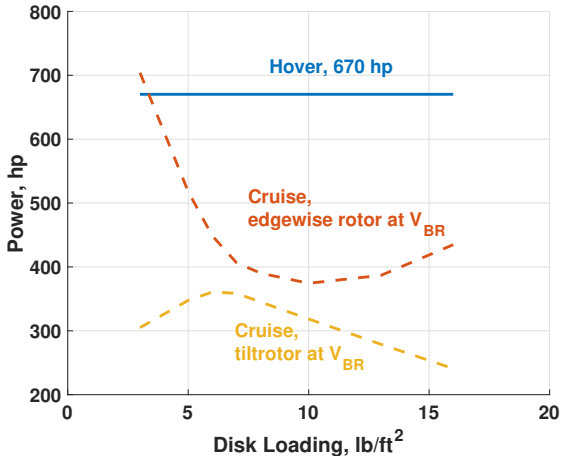

Figure 7.11: Cruise power versus disk loading for edgewise and tilting prop rotors.

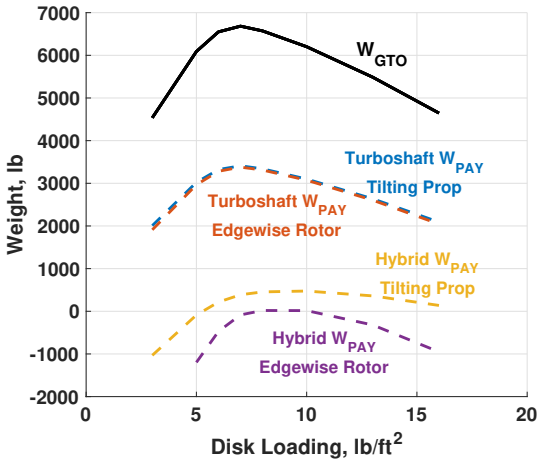

Figure 7.12: Payload for edgewise rotor vs tilting proprotor configurations.

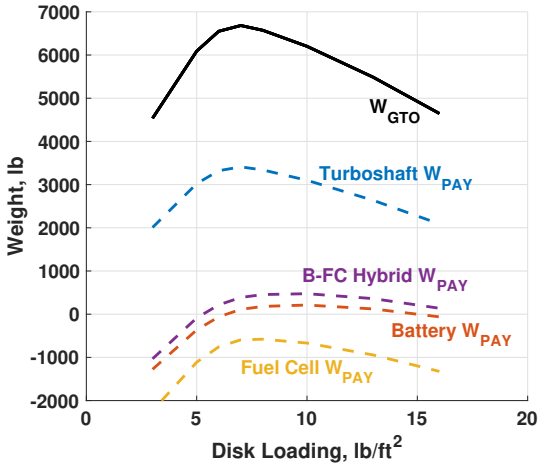

Figure 7.13: Payload for tilting proprotor configuration; various power sources; baseline technology.

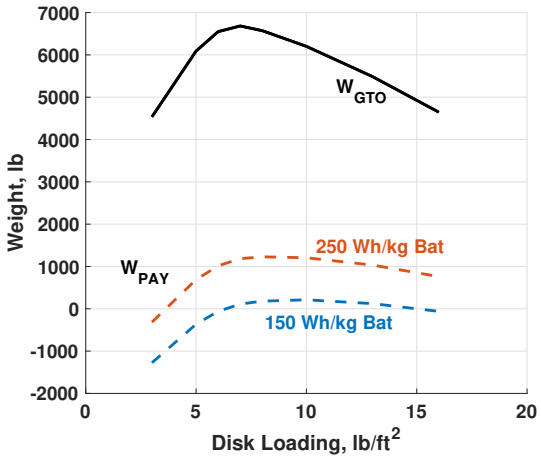

Figure 7.14: Battery powered; improved technology; tilting proprotor.

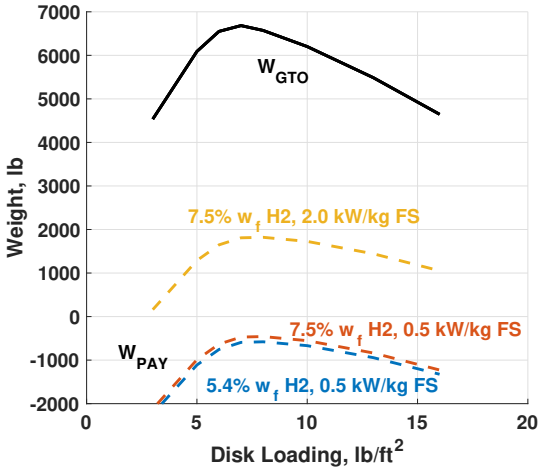

Figure 7.15: Fuel cell powered; improved technology; tilting proprotor.

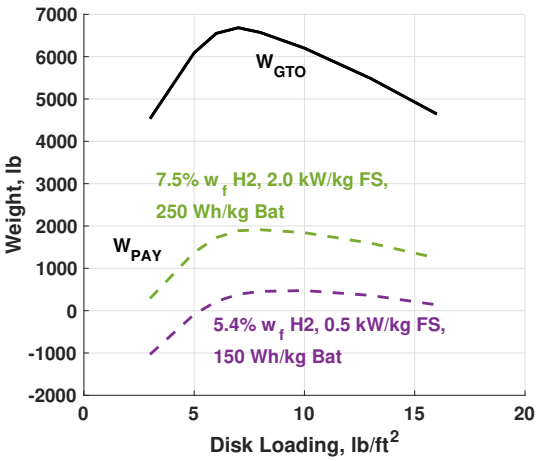

Figure 7.16: B-FC hybrid powered; baseline technology; tilting proprotor.

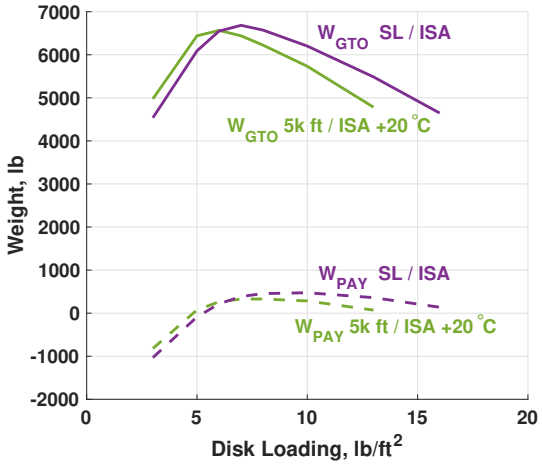

Figure 7.17: B-FC hybrid powered; high altitude and temperature comparison; baseline technology; tilting proprotor.

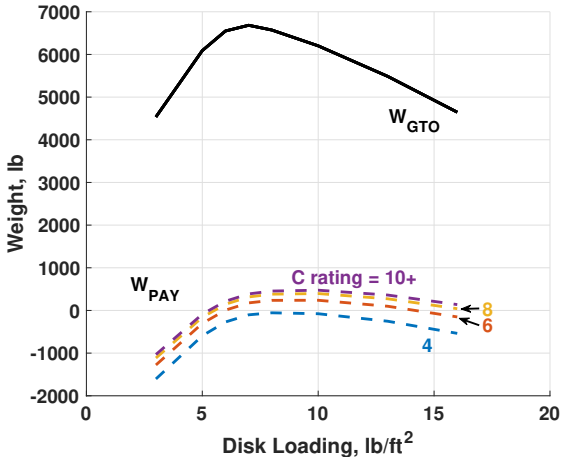

Figure 7.18: B-FC hybrid powered; baseline technology; tilting proprotor.

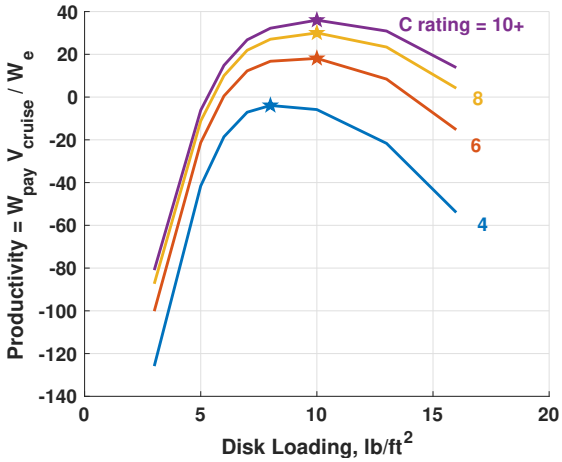

Figure 7.19: B-FC hybrid powered; baseline technology; tilting proprotor.

Table 7.2: Conceptual designs for a two-rotor tiltrotor aircraft for a 5 min hover mission

Cruise Range, mi	**50**	**75**	**150**	**150**
Powerplant Type	Bat	Bat-FS	Bat-FS	Bat-FS, improved tech
W_{GTO}, lb	6572	6202	6202	6202
Disk loading, lb/ft^2	8	10	10	10
Rotor radius, ft	11.4	9.9	9.9	9.9
Max hover power, hp	670	670	670	670
Cruise power, hp	345	318	318	318
Cruise speed, mph	177	177	177	177
Total energy, hp-hr	153	191	326	326
W_{PAY}, lb	834	475	84	1560
FUEL:				
W_{FS}, lb	0	1257	1257	315
PEM Wh/kg		211	387	1544
PEM kW/kg		0.42	0.42	1.65
H2 kg		25	46	46
Tank w_f		5.4	5.4	5.4
W_B, lb	2058	396	396	243
BAT Wh/kg	152	152	152	248
BAT kW/kg	0.53	1.46	1.46	2.38
BAT current in C	3.5	9.6	9.6	9.6
EMPTY WEIGHT W_E:				
W_P, lb	999	904	904	904
Motors, lb	714	646	646	646
Controller/inverter, lb	143	129	129	129
Cooling, lb	143	129	129	129
W_S, lb	1577	1488	1488	1488
W_{Oth}, lb	1104	1025	1025	1025

The results have shown that a hybrid powerplant is necessary to achieve a 75 mile range with practical payload. To investigate the possibility of further extending the range, the same aircraft sizing was carried out for an extended mission of 150 mile cruise. Figure 7.20 shows that for this extended mission, only the B-FC hybrid powerplant is light enough to accommodate any payload at all. It achieves a payload weight of 100 lb for a gross take-off weight of 6200 lb. Figure 7.21 shows the

results if the improved technology factors are used (250 Wh/kg batteries, 7.5% w_f storage tanks, and 2.0 kW/kg fuel cells). With these numbers, the hybrid powerplant achieves a substantial payload of 1600 lb for a gross take-off weight of 6200 lb. As in the previous mission, it is important to note that these results require a battery C-rating of 10 C, and results for limited C-rate batteries are shown in Fig. 7.22. Note that unlike in Fig. 7.18 for the 75 mi mission, this plot uses improved technology numbers. Even a 4 C battery can achieve a substantial payload of 1200 lb at a gross take-off weight of 6200 lb. However, with baseline technology numbers, no payload is possible for a C-rate below 10 C. Figure 7.23 shows the productivity of the hybrid powerplant for different battery C-ratings using improved technology numbers. The maximum productivity always occurs at a disk loading of 10 lb/ft^2 regardless of battery C-rate.

If the hover time were to decrease to less than 5 min, the C rating for the optimal powerplant would increase beyond 10 C. This is because the power required for hover remains the same, while the energy required is decreased. The battery is sized to meet the required energy, so the battery weight required for a shorter hover mission will be smaller. However, since the power required is the same, for this smaller battery to deliver the same power, the C-rating will increase.

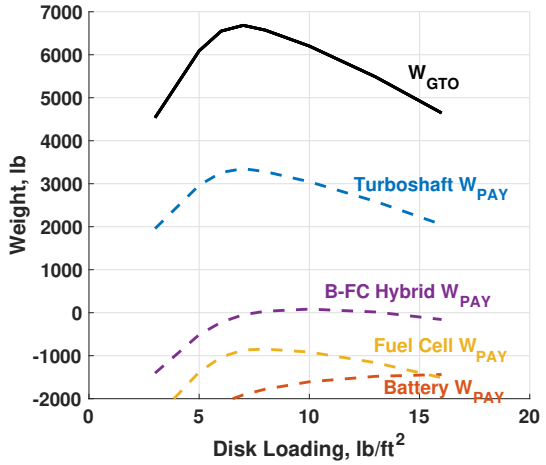

Figure 7.20: Various power sources; baseline technology; tilting proprotor; extended range mission.

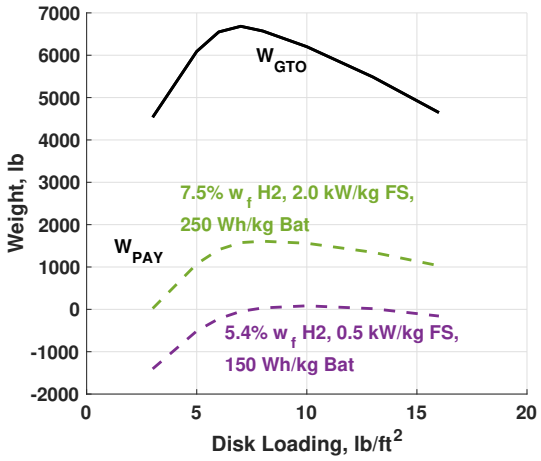

Figure 7.21: B-FC hybrid power; improved technology comparison; tilting proprotor; extended range mission.

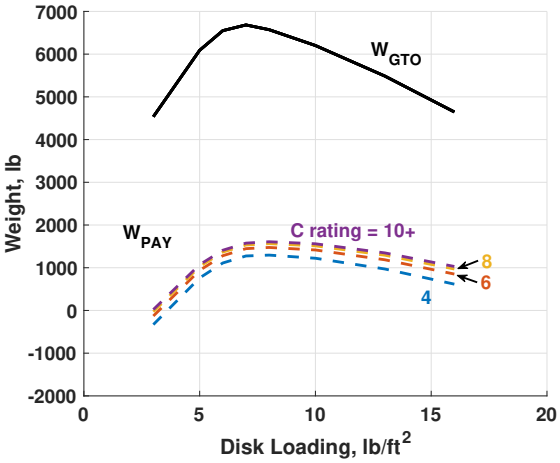

Figure 7.22: B-FC hybrid; improved technology; tilting proprotor; extended range mission.

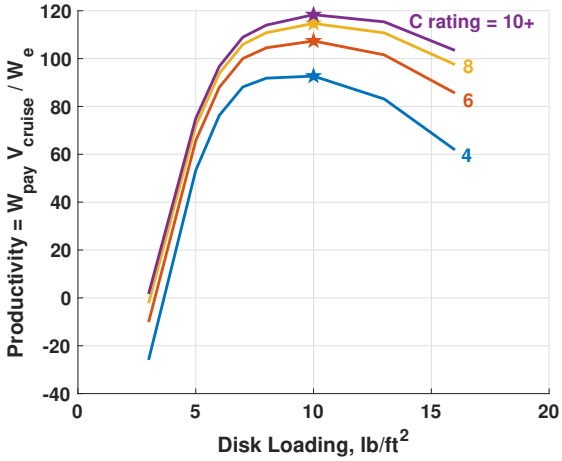

Figure 7.23: B-FC hybrid versus battery; improved technology; limited battery C-rating; tilting proprotor; extended range mission.

The final mission is the shortest: 5 min hover and 50 mi cruise, which is perhaps barely sufficient for an intra-city commute.

Figure 7.24 shows the W_{PAY} of different power configurations for a range of disk loadings. For this mission, the battery-only powerplant is best among the

all-electric options. This is because less energy is required for the mission, and a relatively large portion of it is at high power, so there is limited payoff for the high energy hydrogen fuel. Furthermore, aside from weight considerations, the B-FC combined system also introduces more complexity without any benefit in payload. For a gross weight of 6200 lb, the battery-only system can carry a payload of 800 lb. Figure 7.25 shows how an improvement in battery specific energy to 250 Wh/kg would increase the aircraft payload to 1600 lb. The fuel cell technology improvement results are identical to that of the baseline mission, shown in Fig. 7.15, because the fuel cell is sized to the maximum power, which remains the same for the abbreviated mission. Accounting for improved technology factors (250 Wh/kg batteries, 7.5% w_f storage tanks, and 2.0 kW/kg fuel cells), the hybrid configuration again becomes slightly favorable, as shown in Fig. 7.26. The 6200 lb vehicle is then able to carry a 1900 lb payload, or a 6600 lb vehicle can carry a 2000 lb payload; the former maximizes productivity while the latter maximizes payload.

For the shortest mission, the battery-only configuration with baseline technology was chosen to investigate the effects of limited C-rating. The results are shown in Fig. 7.27. A C-rating of at least 3 C is still needed for the battery powerplant, for a maximum payload of 500 lb, and even greater C-rating is needed for the hybrid.

Figure 7.28 shows the productivity of the battery-only power for various C-ratings. Based on these results, the optimal aircraft for the shortest mission would be battery powered and would have approximately: batteries with C-rating of 4 C, disk loading of 10 lb/ft^2, W_{GTO} of 6200 lb, and a payload weight of 800 lb.

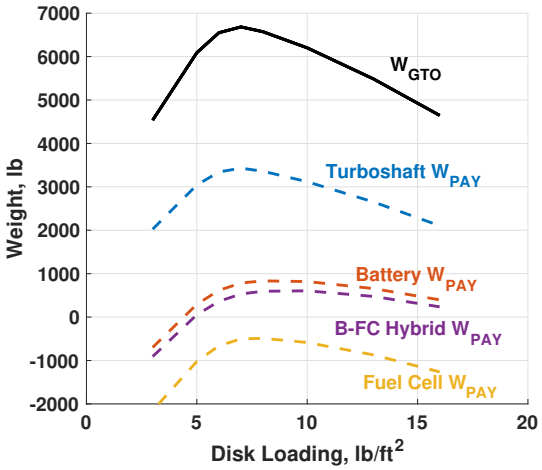

Figure 7.24: Various powerplants; baseline technology; tilting proprotor; shortest intra-city mission.

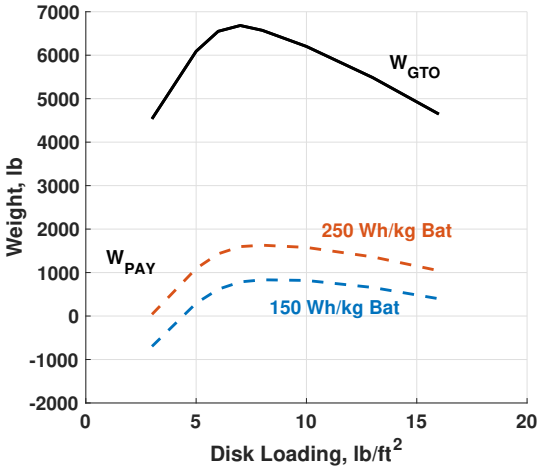

Figure 7.25: Battery-only powerplant; improved technology comparison; tilting proprotor; shortest intra-city mission.

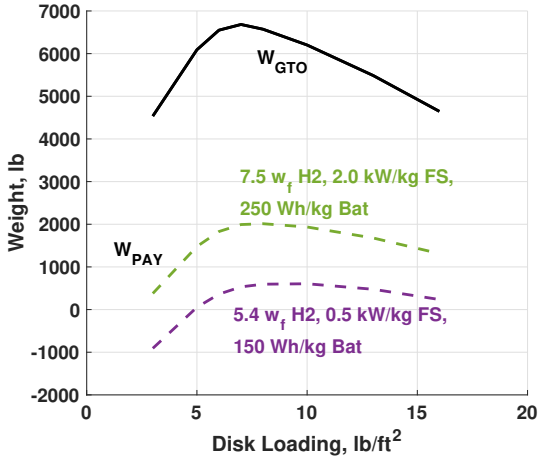

Figure 7.26: B-FC hybrid powerplant; improved technology comparison; tilting proprotor; shortest intra-city mission.

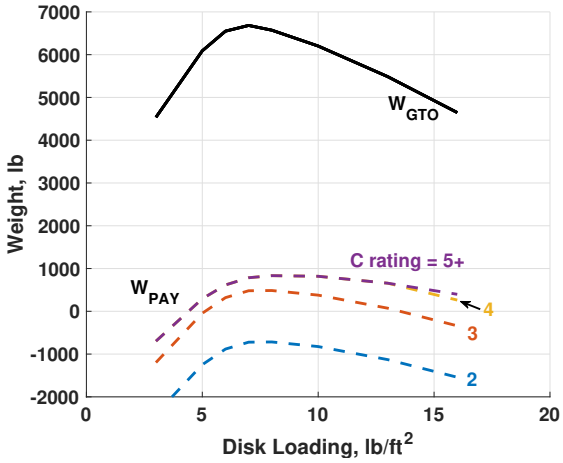

Figure 7.27: Battery-only; baseline technology; tilting proprotor; shortest intra-city mission.

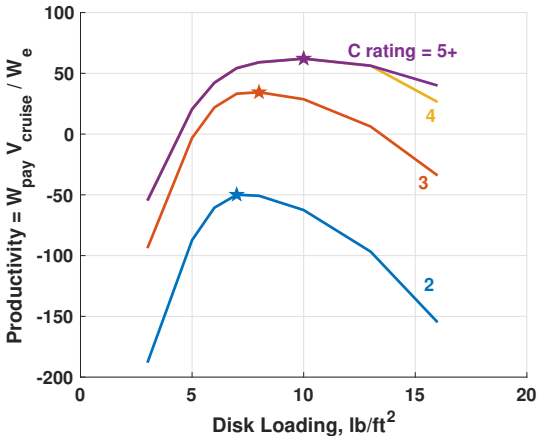

Figure 7.28: Fuel cell versus battery; baseline technology; limited battery C-rating; tilting proprotor; shortest intra-city mission.

Chapter 8: Summary and Conclusions

8.1 Summary

The use of hydrogen fuel cells combined with Li-ion batteries were examined as a potential candidate to increase range, endurance, and payload of eVTOL aircraft. Steady-state and transient models were developed for fuel stacks and Li-polymer batteries. A test bed was constructed to calibrate the model constants and validate transient predictions. The electrochemical sources were first used in isolation for independent calibration and validation of the models. They were then used in unregulated parallel combination to test a tethered flying quadrotor. A method for regulated power sharing was developed to optimize the use of the two power sources over the course of a mission with a notional power profile. Based on the calibrated models, experimental data from this test bed, and regulated power sharing scheme, a simple eVTOL sizing was carried out. It examined urban, on-demand missions ranging from 50–150 mi for three types of powerplants: battery only, fuel cell only, and a battery-fuel cell (B-FC) hybrid.

The results from the sizing provided context for research and revealed areas of promising returns on investment. For example, a tilting propellor configuration was found to be more appropriate than an edgewise configuration (regardless of the

number of rotors). Higher power rating in batteries (with power rating generation up to 10 C), increased mass efficiency of hydrogen storage, and transfer of automobile fuel stacks to flight applications appeared to be of pressing importance. Using both batteries and fuel cells seemed far more promising than batteries alone.

8.2 Conclusions

Based on systematic hardware testing, analytical modeling, and eVTOL sizing, the following key conclusions were drawn:

1. The transient nature of electrochemical sources is primarily driven by a first order capacitative behavior. Battery and fuel cell transients can both be modeled using the same underlying equivalent circuit networks. The circuit elements, and consequently the time constants, are different. There are presently no first principle methods to identify these components easily, so a semi-empirical approach is essential.

2. The models developed in this paper were generally able to capture the magnitudes and waveforms of experimental data. Some mean errors existed for both the fuel stack and battery. Additionally, the fuel stack model failed to capture a transient occurring immediately after it is turned on, and the battery discharge rate model was less accurate when placed in parallel with a fuel stack for flight testing. In general, the voltage model was accurate to within 5% for both the battery and fuel cell.

3. The fuel cells used in this research are in fact faster to respond than batteries,

and both are agile enough to handle rapid power transients in VTOL, as long as the current remains in the nominal range. The time constant in the normal operating range for the fuel stack was 0.02 s and for the battery 1.69 s. There are more significant transient behaviors in the low current (high voltage) and high current (low voltage) range that require further investigation. These limits are important for fuel cell eVTOL as they occur near the highest efficiency and highest power limits of the fuel cell.

4. An estimate for the fuel stack balance of plant power losses was found to be 15-25% of operating power. This loss was primarily due to the DC-DC step down, a smaller additional loss associated with the diodes used for power sharing regulation, and a very small loss due to the length of electrical wiring.

5. An estimate for weight overhead of the fuel stack is 15%, again primarily from power electronics. This is the mass that would not be included in the reported specific power of a fuel stack. The value is conservative for this small, low-end fuel stack and step-down.

6. Power sharing between a battery and fuel stack can be regulated to minimize the total powerplant weight if the fuel stack supplies a constant power, the battery provides supplemental power during high power portions of the mission, and the fuel stack charges the battery during low power portions of the mission. This regulation can be accomplished using an Arduino, two solid state relays, and three DC-DC converters.

7. For a baseline mission of 75 miles using a tiltrotor aircraft, a fuel cell and battery combined powerplant is the best option. Using 150 Wh/kg and 10C batteries, 0.5 kW/kg fuel stack, 5% w_f tank, an aircraft sized for this mission can carry 500 lb (at least 2 passengers) with a gross weight of 6200 lb and disk loading of 10 lb/ft^2. The B-FC combination is superior to either electric power source alone.

8. For a longer inter-city mission of 150 miles, the fuel cell and battery combined powerplant is the only option that gives a practical payload with present technology. At this range and speed, using baseline technology, a tiltrotor aircraft optimized for productivity (payload weight $\times$ speed / empty weight) has a disk loading of 10 lb/ft^2, gross weight of 6200 lb, and a payload of 100 lb.

9. For an short intra-city mission of 50 miles, batteries alone are the lightest powerplant option. For this mission, using 4 C batteries with baseline energy density (150 Wh/kg), a 6200 lb aircraft with a disk loading of 10 lb/ft^2 can carry 800 lb.

10. Improved battery C-rate (i.e. power density) is critical to using batteries in eVTOL for practical payloads. Based on the mission profile used in this paper, with baseline numbers (150 Wh/kg batteries, 0.5 kW/kg fuel stack, 5% w_f tank), a 50 mile mission requires a 4 C battery for a payload of 800 lb or 3 C for a payload of 500 lb, a 75 mile mission requires 10 C for a payload of 500 lb or 6 C for a payload of 200 lb, and a 150 mile mission requires 10 C for a payload of 100 lb. Current battery technology of 150 Wh/kg and 3 C is

insufficient to carry a practical payload for distances much more than 50 miles.

11. With future technology reported by industry (250 Wh/kg available for batteries, 2 kW/kg for fuel cells, and 7.5% w_f hydrogen storage), for the baseline mission of 75 miles, an aircraft with a gross take-off weight of 6200 lb can carry a payload of 1900 lb with a B-FC hybrid powerplant, or 1800 lb with a fuel cell-only powerplant. For the extended range of 150 miles, a 6200 lb aircraft can carry 1600 lb with a B-FC hybrid powerplant. For an intra-city range of 50 miles, a 6200 lb aircraft can carry a 2000 lb payload using batteries alone.

12. Strategic investments for technology development depend on the target mission length. For missions longer than 50 miles, improved technology for fuel cell power density is very promising for combined battery and fuel cell powerplants. For shorter missions, improving battery energy density for battery powerplants is more important. For all mission lengths, battery power density must be improved to 4-10 C if specific energy remains limited to 150 Wh/kg batteries.

8.3 Contributions

This work is the first comprehensive study of fuel cells for eVTOL. It not only shows the potential of the B-FC hybrid for realistic eVTOL missions through thorough conceptual design, but also demonstrates several of the practical requirements to implement the hybrid configuration. These include the development and demonstration of a regulated power sharing architecture and the verification of sufficiently fast response speeds of the fuel stack and battery. A new two-dimensional trim was

developed to analyze the performance of tilting proprotor aircraft. Furthermore, the methodology used to do all this is documented in sufficient detail to replicate the work. The benefits and challenges of incorporating fuel cells were clarified through modeling, experimentation, and conceptual design informed by measured overheads.

8.4 Future Work

The fuel cell and battery individual models should be expanded to include thermal management. A combined power sharing model should be developed to design a B-FC hybrid powerplant given any mission power profile, as well as predict the battery state of charge and fuel stack fuel consumption throughout the course of the mission. The design should include the power of the fuel cell, the quantity of hydrogen fuel, and the power, energy, charging C-rate, and discharging C-rate of the battery.

On the experimental side, the (presently ground-based) powerplant should be integrated on-board the aircraft. This would require a larger aircraft and higher power density fuel stack. This tether-free aircraft would enable tests in highly transient, maneuvering flight conditions. It would provide more accurate data on the scaling of calibration constants as well as mass and power overheads. Proper testing will require incorporation of flexible rotor dynamics as well as transient RPM loading, which are the subjects of ongoing research.

Bibliography

[1] Colucci, F., "Lift Where you Need It," *Vertiflite*, Vol. 62, No. 6, November/December 2016a, pp. 26–30.

[2] Whittle, R., "Air Mobility Bonanza Beckons Electric VTOL Developers," *Vertiflite*, Vol. 63, No. 2, March/April 2017, pp. 14–21.

[3] Chretien, P., "The Quest for the World's First Electric Manned Helicopter Flight," *Vertiflite*, Vol. 58, No. 2, March–April 2012, pp. 38–42.

[4] Schneider, D., "Helicopters Go Electric," *IEEE Spectrum*, Vol. 49, No. 1, Jan. 2012, pp. 11–12.

[5] Holden, J., and Goel, N., "Fast-Forwarding to a Future of On-Demand Urban Air Transportation," *UBER Elevate*, October, 2016.

[6] Lapeña-Rey, N., Mosquera, J., Bataller, E., and Ortí, F., "First Fuel-Cell Manned Aircraft," *Journal of Aircraft*, Vol. 47, No. 6, 2010, pp. 1825–1835.

[7] P. Rathke, J. Kallo, J. Schirmer, T. Stephan, W. Waiblinger, and Weiss-Ungethüm, J., "Antares DLR-H2 Flying Test Bed for Development of Aircraft Fuel Cell Systems P. Rathke," *ECS Transactions*, Vol. 51, No. 1, 2013, pp. 229–241.

[8] Flade, S., Kallo, J., Schirmer, J., and Stephan, T., "Comparison of Anode Configurations During Long Distance Flight in Fuel Cell Powered Aircraft Antares DLR-H2," AIAA Paper 2014. *SciTech Forum 52nd Aerospace Sciences Meeting*, National Harbor, MD, 2014.

[9] Kallo, J., Flade, S., Stephan, T., and Schirmer, J., "Antares DLR H2 - Test Bed for Electric Propulsion," AIAA Paper 2015. *53rd AIAA Aerospace Sciences Meeting*, January, 2015.

[10] Romeo, G., Borello, F., Correa, G., and Cestino, E., "ENFICA-FC: Design of transport aircraft powered by fuel cell & flight test of zero emission 2-seater aircraft powered by fuel cells fueled by hydrogen," *International Journal of Hydrogen Energy*, Vol. 38, No. 1, 2012, pp. 469–479.

[11] Moffitt, B. a., and Zaffou, R., "Polymer-Electrolyte Fuel Cells for UAV Applications Providing Solutions to Revolutionize UAVs," 2012. doi:10.4271/2012-01-2161.

[12] EnergyOr shows off world's first fuel cell multirotor UAV. (n.d.). Fuel Cells Bulletin, 2015(4), 5–6. https://doi.org/10.1016/S1464-2859(15)30078-X

[13] Datta, A., and Johnson, W., "Requirements for a Hydrogen Powered All-Electric Manned Helicopter," *AIAA Paper 2012-5405*, 12th AIAA ATIO Conference, Indianapolis, IN, 2012.

[14] Datta, A., and Johnson, W., "Powerplant Design and Performance Analysis of a Manned All-Electric Helicopter," *Journal of Propulsion and Power*, Vol. 30, No. 2, February 2014, pp. 490–505.

[15] Ng, W., Datta, A., "Development of Propulsion System Models for Electric-VTOL Aircraft," *AIAA Paper 2018-1750*, 1018 AIAA Aerospace Sciences Meeting, AIAA SciTech Forum, January 2018.

[16] Ng, W. and Datta, A. "An Examination of Hydrogen Fuel Cells and Lithium-Ion Batteries for Electric Vertical Take-Off and Landing (eVTOL) Aircraft", *Paper 113*, 44th European Rotorcraft Forum, Delft, Netherlands, September 2018.

[17] Sinsay, J. D., Alonso, J. J., Kontinos, D. A., Melton, J. E., and Grabbe, S., "Air Vehicle Design and Technology Considerations for an Electric VTOL Metro-Regional Public Transportation System," *AIAA Paper 2012-5404*, 12-th AIAA ATIO Conference, Indianapolis, IN, 2012.

[18] Nagaraj, V. T., and Chopra, I., "Explorations of Novel Powerplant Architectures for Hybrid Electric Helicopters," *American Helicopter Society 70-th Annual Forum*, Montreal, Canada, 2014.

[19] Snyder, C. A., "Exploring Propulsion System Requirements for More and All-Electric Helicopters," *Paper 2015-20221*, 22nd International Symposium on Air Breathing Engines (ISABE), Phoenix, AZ, 2015.

[20] Dever, T. P., Duffy, K. P., Provenza, A. J., Loyselle, P. L., B., C. B., Morrison, C., and Lowe, A., "Assessment of Technologies for Noncryogenic Hybrid Electric Propulsion," *NASA TP-2015-21658*, 2015.

[21] Johnson, W., "NDARC NASA Design and Analysis of Rotorcraft," *NASA/TP-2015-218751*, 2016.

[22] Gao, L., Liu, S., and Dougal, R. A., "Dynamic Lithium-Ion Battery Model for System Simulation," *IEEE Transactions on Components and Packaging Technologies*, Vol. 25, No. 3, September 2002, pp. 495–505.

[23] Chen, M., and Rincón-Mora, G. A., "Accurate Electrical Battery Model Capable of Predicting Runtime and I-V Performance," *IEEE Transactions on Energy Conversion*, Vol. 21, No. 2, June 2006, pp. 504–511.

[24] Johnson, V. H., "Battery Performance Models in ADVISOR," *Journal of Power Sources*, Vol. 110, No. 2, August 2002, pp. 321–329.

[25] Markel, T., Brooker, A., Hendricks, T., Johnson, V., Kelly, K., Kramer, B., O'Keefe, M., Sprik, S., and Wipke, K., "ADVISOR: a systems analysis tool for advanced vehicle modeling," *Journal of Power Sources*, Vol. 110, No. 2, August 2002, pp. 255–266.

[26] Matsunaga, M., Fukushima, T., and Ojima, K., "Powertrain System of Honda FCX Clarity Fuel Cell Vehicle," *World Electric Vehicle Journal*, Vol. 3, International Battery, Hybrid and Fuel Cell Electric Vehicle Symposium 24, Stavanger, Norway, 2009.

[27] Hasegawa, T., Imanishi, H., Nada, M., and Ikogi, Y., "Development of the Fuel Cell System in the Mirai FCV," *SAE Technical Paper 2016-01-1185*, SAE 2016 World Congress and Exhibition, Detroit, MI, 2016.

[28] Yoshida, T., and Kojima, K., "Toyota MIRAI Fuel Cell Vehicle and Progress Toward a Future Hydrogen Society," *Electrochemical Society Interface*, Vol. 24, No. 2, Summer 2015, pp. 45–49.

[29] O'Hayre, R., Cha, S., Colella, W., and Prinz, F. B., *Fuel Cell Fundamentals*, 2nd ed., John Wiley and Sons, Inc., 2009.

[30] Office of Energy, Efficiency, and Renewable Energy, "Types of Fuel Cells", Retrieved from https://www.energy.gov/eere/fuelcells/types-fuel-cells.

[31] Andújar, J. M. and Segura, F. (2009). "Fuel cells: History and updating. A walk along two centuries." *Renewable and Sustainable Energy Reviews*, 13, 2309–2322. https://doi.org/10.1016/j.rser.2009.03.015.

[32] Warshay, M. and Prokopius, P. R. (1989), "The Fuel Cell in Space: Yesterday, Today and Tomorrow," Grove Anniversary Fuel Cell Symposium (Vol. NASA TM-102366), https://doi.org/10.1016/0378-7753(90)80019-A.

[33] J.S. Fordyce, "Technology Status—Batteries and Fuel Cells", Future Orbital power Systems Technology Requirements, NASA CP-2058, 1978, pp. 157–166.

[34] Aso, S., Kizaki, M., and Nonobe, Y. (2007). "Development of fuel cell hybrid vehicles in TOYOTA". 2007 Power Conversion Conference - Nagoya (pp. 1606–1611). https://doi.org/10.1109/PCCON.2007.373179

[35] Barrett, S. (2005). "AeroVironment Flies World's First Hydrogen Powered Plane". *In Fuel Cells Bulletin* (pp. 2–3).

[36] Bradley, T. H., Moffitt, B. A., Mavris, D. N., and Parekh, D. E. (2007). "Development and experimental characterization of a fuel cell powered aircraft". *Journal of Power Sources*, 171, 793–801. https://doi.org/10.1016/j.jpowsour.2007.06.215

[37] Gong, A. and Verstraete, D., "Fuel cell propulsion in small fixed-wing unmanned aerial vehicles: Current status and Research Needs", *Int J of Hydrogen Energy*, v 42, (33), August 2017

[38] Rathke, P., Kallo, J., Schirmer, J., Stephan, T., Waiblinger, W., and Weiss-Ungethüm, J. (2013). "Antares DLR-H2 – Flying Test Bed for Development of Aircraft Fuel Cell Systems". *ECS Transactions*, 51(1), 229–241. https://doi.org/10.1149/05101.0229ecst

[39] Yan, Q., Toghiani, H., and Causey, H., "Steady State and Dynamic Performance of Proton Exchange Membrane Fuel Cells (PEMFCs) Under Various Operating Conditions and Load Changes," *Journal of Power Sources*, Vol. 161, May 2006, pp. 492–502.

[40] Yan, Q., Toghiani, H., and Wu, J., "Investigation of water transport through membrane in a PEM fuel cell by water balance experiments," *Journal of Power Sources*, Vol. 158, October 2005, pp. 316–325.

[41] Amphlett, J. C., Mann, R. F., Peppley, B. A., Roberge, P. R., and Rodrigues, A., "A Model Predicting Transient Responses of Proton Exchange Membrane

Fuel Cells," *Journal of Power Sources*, Vol. 61, No. 1-2, July-August 1996, pp. 183–188.

[42] Ceraolo, M., Miulli, C., and Pozio, A., "Modelling Static and Dynamic Behavior of Proton Exchange Membrane Fuel Cells on the Basis of Electro-chemical Description," *Journal of Power Sources*, Vol. 113, No. 1, January 2003, pp. 131–144.

[43] Benziger, J., Chia, E., Moxley, J. F., and Kevrekidis, I. G., "The Dynamic Response of PEM Fuel Cells to Changes in Load," *Chemical Engineering Science*, Vol. 60, No. 5, March 2005, pp. 1743–1759.

[44] Ziogou, C., Voutetakis, S., Papadopoulou, S., and Georgiadis, M. C., "Modeling, Simulation and Experimental Validation of a PEM Fuel Cell System," *Computers and Chemical Engineering*, Vol. 35, No. 9, September 2011, pp. 1886–1900.

[45] Buller, S., Karden, E.,d Kok, D. and De Doncker, R. W., "Modeling the Dynamic Behavior of Supercapacitors Using Impedance Spectroscopy," *IEEE Transactions on Industry Applications*, Vol. 38, no. 6, Nov-Dec 2002, pp. 1622–1626.

[46] Shepherd, C. M., "Design of Primary and Secondary Cells II. An Equation Describing Battery Discharge," *Journal of The Electrochemical Society*, Vol. 112, No. 7, 1965, pp. 657–664.

[47] Johnson, V. H., Pesaran, A. A., and Sack, T., "Temperature-Dependent Battery Models for High-Power Lithium-lon Batteries", 17th Annual Electric Vehicle Symposium, Montreal, Canada, October 2000.

[48] Dong, T. K., Kirchev, A., Mattera, F., Kowal, J., and Bultel, Y., "Dynamic Modeling of Li-ion Batteries Using an Equivalent Electrical Circuit," *Journal of the Electrochemical Society*, Vol. 158, No. 3, January 2011, pp. 326–336.

[49] McDonald, R. A., "Electric Propulsion Modeling for Conceptual Aircraft Design," *AIAA Paper 2013-0941*, 52nd Aerospace Sciences Meeting, AIAA SciTech Forum, January 2014.

[50] Johnson, W., "NDARC - NASA Design and Analysis of Rotorcraft Validation and Demonstration," *AHS Aeromechanics Specialists Conference*, January 2010.

[51] Harris, F. D., "Introduction to Autogyros, Helicopters, and Other V/STOL Aircraft," *Volume II: Helicopters, NASA/SP-2012-215959*, 2012.